

**On the evolution of sea surface
temperature in the tropical
Pacific**

Hein Zelle

On the evolution of sea surface temperature in the tropical Pacific

Veranderingen in oppervlaktetemperatuur in de
tropische Stille Oceaan

(met een samenvatting in het Nederlands)

PROEFSCHRIFT

Ter verkrijging van de graad van doctor aan de Universiteit Utrecht
op gezag van Rector Magnificus Prof. dr. W. H. Gispen
ingevolge het besluit van het College voor Promoties
in het openbaar te verdedigen op

maandag 9 mei 2005 des middags om 14:30 uur

door

Hein Daniël Zelle

geboren op 14 mei 1975 te Geldrop

promotoren: Prof. Dr. G.J. Komen
Faculteit Natuur- en Sterrenkunde,
Instituut voor Marien en Atmosferisch Onderzoek Utrecht (IMAU),
Universiteit Utrecht

Prof. Dr. B.A.C. Ambrosius
Faculteit Luchtvaart- en Ruimtevaarttechniek,
Department of Earth Observation and Space Systems (DEOS),
Technische Universiteit Delft

co-promotor: Dr. G.J.H. Burgers
Koninklijk Nederlands Meteorologisch Instituut (KNMI),
De Bilt

This research was supported by the Netherlands Council for Earth and Life Sciences (ALW) with financial aid from the Netherlands Organisation for Scientific Research (NWO). The study was carried out at the Royal Netherlands Meteorological Institute (KNMI) in De Bilt, The Netherlands.

Contents

1	Introduction	1
1.1	Discovery of El Niño – Southern Oscillation	2
1.2	El Niño – Southern Oscillation	2
1.2.1	Observations of the tropical Pacific	2
1.2.2	What is normal?	4
1.2.3	The ENSO pattern and cycle	7
1.2.4	Teleconnections	11
1.3	Mechanisms, processes and feedbacks	15
1.3.1	Basic mechanisms	15
1.3.2	The effect of thermocline depth anomalies on SST	18
1.3.3	The interaction between wind stress and SST	21
1.4	Predicting El Niño	22
1.4.1	Models	22
1.4.2	ENSO Forecasts	23
1.4.3	The effect of global change	26
1.5	This thesis	27
2	SST and thermocline depth	29
2.1	Introduction	30
2.2	Observations	34
2.3	Model Runs	34
2.3.1	HOPE	35
2.3.2	Linear shallow-water model	35
2.4	Data analysis	36
2.4.1	Lag correlation between thermocline depth and SST, using TAO / TRITON data	36
2.4.2	Lag correlation between thermocline depth and SST, using HOPE model output	38
2.4.3	Lag correlation between thermocline depth and SST, using lin- ear model output	41
2.5	Two pathways	43
2.5.1	The upwelling pathway	43
2.5.2	The wind coupling pathway	48

Contents

2.6	Discussion	49
2.7	Conclusions	51
3	Evolution of SST anomalies in the warm pool	53
3.1	Introduction	54
3.2	Observations	55
3.3	Model	59
3.3.1	Setup	59
3.3.2	Budget study	59
3.4	Results	61
3.4.1	Growth phase	61
3.4.2	Peak phase	65
3.4.3	Decay phase	66
3.4.4	Summary	67
3.5	Discussion	67
3.5.1	Zonal wind and wind speed	69
3.5.2	Mixed layer depth	69
3.6	Summary and Conclusions	71
4	El Niño and greenhouse warming	73
4.1	Introduction	74
4.2	Global warming in the ensemble simulations	75
4.2.1	Model	75
4.2.2	Changes in the global mean state	76
4.3	ENSO and Global Change	76
4.4	Analysis	83
4.4.1	Low-order chaos versus noise driven	83
4.4.2	Sensitivities in ICMs	84
4.4.3	The wind response in CCSM	87
4.5	Summary and Discussion	91
5	Discussion	95
	Bibliography	99
	Samenvatting	107
	Dankwoord	111
	Curriculum vitae	113

Chapter 1

Introduction

In April 1997, meteorological institutes around the world issued warnings that an El Niño event was imminent. Droughts were predicted for eastern Indonesia, Australia and parts of Africa. Increased rainfall and floods were expected in Peru. Over the course of the year El Niño developed into the strongest recorded event ever. In October many of the warnings proved correct, preventing damage to people in several regions. At the same time, some developing countries were hit hard by the effects: forest fires occurred on Borneo and there were food shortages in Indonesia. In January a lake was formed in Peru where there was desert before, and a whole valley turned green for the first time in many years.

Although the sudden development and strength of El Niño surprised researchers (Pearce, 1997), it was clear what was going on and many of the effects were expected beforehand. This was in stark contrast to the El Niño of 1982/83, which went unnoticed until it was almost over (Philander, 1990). That event prompted the development of observational and modeling programs, to gain understanding and predictability of El Niño. These programs have coordinated and financed observations of the equatorial Pacific ocean since approximately 1990. A much improved understanding of El Niño has been the result, but many questions still remain.

This thesis contributes further to the improved understanding of El Niño. To put this contribution into perspective, some background on El Niño is provided first. The introduction starts with historical facts about El Niño. The El Niño cycle will then be discussed, starting with the normal situation, followed by what is different during an El Niño event and concluding with the effects of El Niño around the world. Next, the mechanisms and the main physical processes that play a role will be discussed. The following section treats the current state of state of El Niño forecasting. The introduction concludes with an overview of the chapters in this thesis.

1.1 Discovery of El Niño – Southern Oscillation

The name El Niño (the Christ child) was used in the 19th century by Peruvian fishermen to describe a warm current along the western coast of South America, which occurs around Christmas each year (Philander, 1990). The phenomenon varied in strength from year to year. At the time these water temperature variations were thought to be local, but in reality they sometimes extend thousands of kilometers westward into the equatorial Pacific, to the dateline and beyond.

In a seemingly separate development, Sir Gilbert Walker noted in the early 20th century that “when pressure is high in the Pacific Ocean it tends to be low in the Indian Ocean from Africa to Australia”, a relationship first mentioned by Hildebrandsson (1897). The pressure difference varies on timescales from months to years, and was given the name “Southern Oscillation”. Papers published by Walker between 1923 and 1937 indicate that the southern oscillation affects the weather in large parts of the globe, but other scientists remained skeptical about the results.

El Niño and the Southern Oscillation were seen as separate phenomena until studies by Berlage (1957), Ichiye and Petersen (1963), Bjerknes (1966) and Doberitz (1968) pointed out that there is an important relation between the two. The sea surface temperature (SST) variations of El Niño are coupled to the atmospheric changes of the Southern Oscillation: high SST in the eastern equatorial Pacific often occurs together with low sea level pressure (SLP), and vice versa. Together they form a coupled oscillating system known today as El Niño – Southern Oscillation (ENSO). The term El Niño is now used to indicate the phase of the oscillation where SST in the eastern equatorial Pacific is high, and SLP is low. La Niña (the girl) is used to indicate the opposite phase, with colder than average SST and higher than average SLP in the eastern equatorial Pacific.

The domain of interest for ENSO is the equatorial Pacific ocean, a map of the region with annual mean surface temperatures is shown in figure 1.1. Three overlapping regions called Niño3, Niño3.4 and Niño4 are indicated on the map, these are used for El Niño analysis and will be introduced in section 1.2.3.

1.2 El Niño – Southern Oscillation

1.2.1 Observations of the tropical Pacific

Our knowledge of El Niño is based on observations of the tropical Pacific ocean. Observations of the oceans have long been restricted to measurements taken from ships and coastal buoys. Such observations have poor spatial coverage in regions like the equatorial Pacific, where there are few busy shipping lanes. Nowadays ships provide not only surface observations but also subsurface temperature measurements, obtained with expendable bathy-thermographs (XBT). An XBT is a weighted thermometer on a thin wire approximately 800 m long. The instrument is thrown overboard, falls to the deep ocean while sending data to the ship through the wire, and is finally discarded. Regions without shipping lanes are occasionally measured on sci-

1.2. El Niño – Southern Oscillation

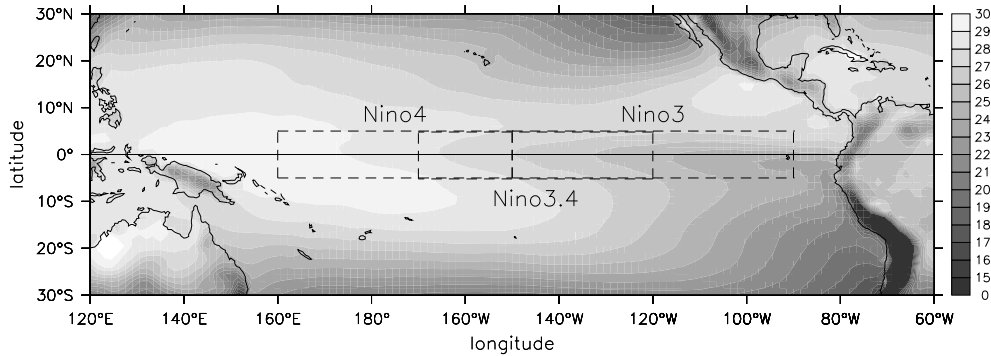


Figure 1.1: A map of the of the equatorial Pacific ocean, showing the annual mean surface temperature from ERA-40 reanalysis data. The Niño3, Niño3.4 and Niño4 regions (introduced in section 1.2.3) are indicated with dashed lines.

entific cruises, for example during the World Ocean Circulation Experiment (WOCE, 1990–2002) research ships repeatedly measured sections in the Atlantic, Pacific, Indian and Southern oceans. On such cruises subsurface temperature, salinity, chemical constituents and sometimes currents are measured at regular intervals.

Ships are no longer the only source of ocean observations. Since the early 1980's satellite observations of the oceans have started to become available (SeaSat in 1978, NOAA Polar-orbiting Operational Environmental Satellite in 1981, Geosat in 1985, see McPhaden et al. (1998a)). Since 1991 satellites continuously measure several oceanic variables with high time and spatial resolutions and near-global coverage. SST is measured from space using a radiometer, an instrument that measures infrared radiation emitted by the sea surface. Sea surface height (SSH) is measured from space with a radar altimeter. This instrument measures the time it takes for a radio wave to travel from the satellite to the earth surface and back, much like a sonar. Combined with detailed knowledge of the satellite orbit SSH anomalies (deviations from the time mean state) can be derived. Quality controlled satellite observations of SSH are made available by projects such as the Radar Altimetry Database System (RADS, Schrama et al., 2000). Surface wind strength and direction are measured with a scatterometer. This instrument sends out a radar signal and measures the strength of the reflected signal. Wind causes ripples on the ocean surface, increasing the surface roughness and the strength of the reflected radar signal. The wind direction is determined by “looking” in several directions. Finally, even rainfall is estimated from satellites, for example with a microwave sensor.

Finally, and perhaps the most important for research on El Niño – Southern Oscillation, the TAO/TRITON mooring array (McPhaden et al., 1998b) has been operational since approximately 1988. It is an array of buoys in the equatorial Pacific. Each buoy is attached by a mooring line to the ocean floor. The buoys measure several surface variables such as SST, air temperature, surface winds, relative humidity and radiation. Below the surface up to a depth of 750 m they measure water tempera-

ture, and sometimes salinity, zonal and meridional currents. The spatial resolution is coarse, approximately 15° zonally, 2° meridionally. The time resolution is very high (minutes) for most variables. The availability of the observations over a long period of time, especially of subsurface temperature measurements, makes the TAO/TRITON array invaluable for El Niño research.

The amount of observations of the equatorial Pacific has increased drastically in recent years. Since 1990 we have a reasonably complete picture of what happens during El Niño events. One of the main goals of this research work is to use these new observations to verify and improve our understanding of how El Niño works.

1.2.2 What is normal?

Before looking into the El Niño cycle, the climate of the equatorial Pacific will be described. We start with a description of the annual mean state. After that the mean seasonal cycle (climatology) will be discussed.

The atmospheric circulation above the tropical Pacific is dominated by the Hadley circulation. Air rises around the equator where the warming by solar radiation is strongest, and flows pole wards in the upper troposphere, descending in the subtropics around 20°N and 20°S . The air returns towards the equator at the surface and is affected by the Coriolis force, which generates the trade winds. These winds from the northeast and southeast converge at the equator, where the air rises again completing the circulation. The region of convergence is called the Inter Tropical Convergence Zone (ITCZ). Due to the north-south asymmetry of the continents it is located somewhat north of the equator, between 5°N and 10°N . A second region of convergence, the South Pacific Convergence Zone (SPCZ) extends from the equator at 140°E to the south east, into the south Pacific.

The easterly trade winds on the equator create a strong contrast between the “warm pool” in the western Pacific and the “cold tongue” in the eastern Pacific. The terms “western Pacific”, “central Pacific” and “eastern Pacific” are used to indicate the approximate regions $130^\circ\text{W} - 170^\circ$, $170^\circ\text{E} - 140^\circ\text{W}$ and $140^\circ\text{W} - 80^\circ\text{W}$ respectively. The “warm pool region” extends from 130°E to approximately 180° . Warm surface waters are pushed westward, forming a warm layer of roughly 150 m depth separated from the deeper, colder water by a sharp vertical temperature gradient. This gradient is called the thermocline, its depth is often approximated by the depth of the 20°C isotherm (Z_{20}). In the eastern Pacific there is relatively strong mean upwelling on the equator, which brings deeper, colder water up to the surface. The thermocline is much shallower here, at approximately 50 m. The surface water in the warm pool is among the warmest in the world oceans, with temperatures between 28°C and 30°C , while in the cold tongue the water is cold for the tropics, with average temperatures below 24°C . This temperature difference gives rise to a second, zonal circulation called the Walker circulation (Bjerknes, 1969), shown in the top panel of figure 1.2. In the warm pool where surface temperatures exceed 28°C , the air rises forming convective clouds which generate rainfall, both over land (Indonesia) and over the ocean. There is an eastward flow in the upper troposphere toward South America. The air sinks over the eastern Pacific where surface waters are cold, reducing the relative humidity and

1.2. El Niño – Southern Oscillation

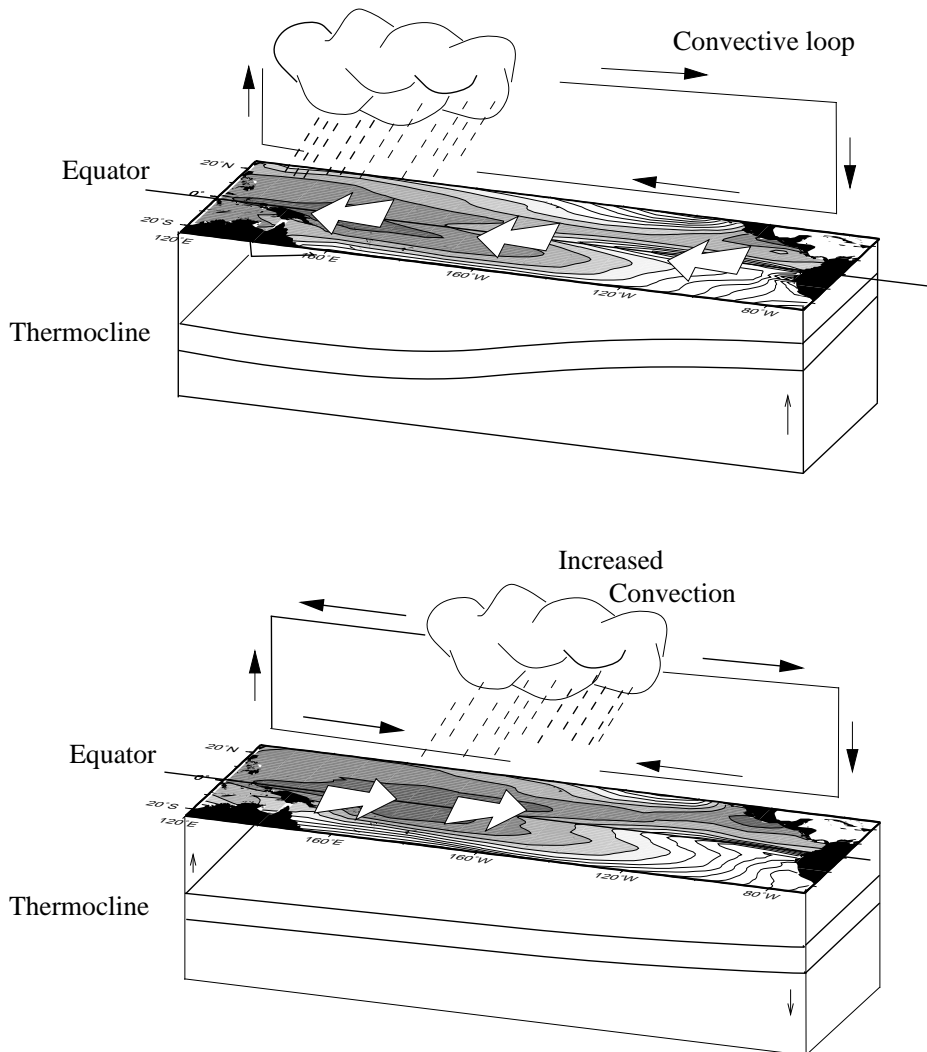


Figure 1.2: An illustration of the Walker circulation and the main features of El Niño. Top figure: normal conditions, with a convective region in the western Pacific. Bottom figure: El Niño conditions, during which the convective region shifts toward the central Pacific. The figures were obtained from Vossepoel (1999), and created after an example on the web-page of the Pacific Marine Environmental Laboratory: <http://www.pmel.noaa.gov/>

Chapter 1. Introduction

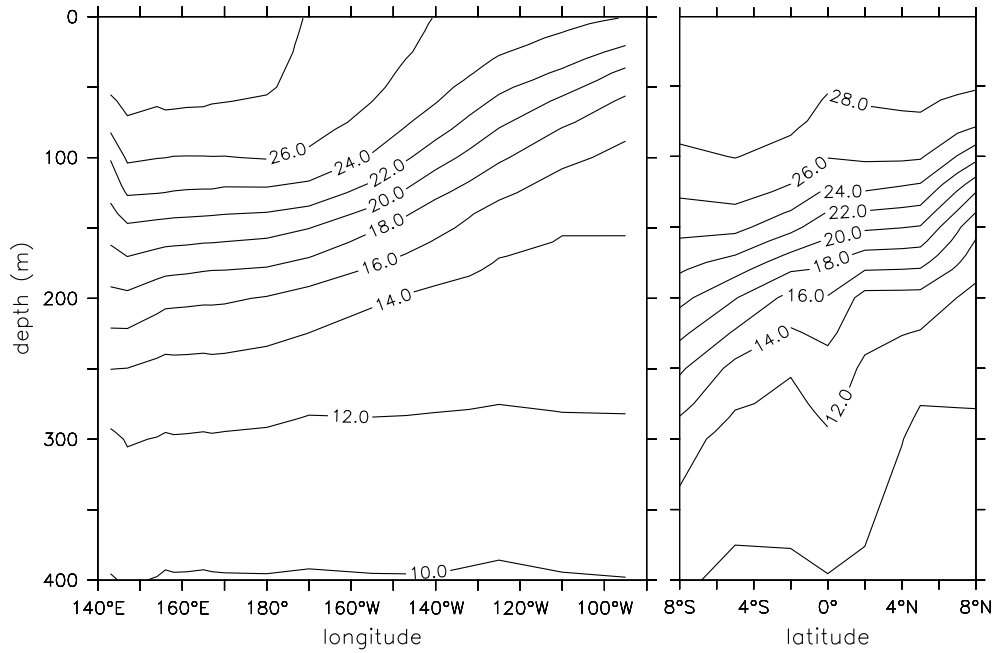


Figure 1.3: Vertical sections of the annual mean subsurface temperature in the equatorial Pacific, from TAO/TRITON observational data. Left: a section along the equator, right: a section at 180° , perpendicular to the equator.

inhibiting rainfall. Over the ocean this results in fields of low stratocumulus clouds and on the South American continent deserts are formed. After sinking, the air flows westward as part of the trade winds, gradually warming and taking up moisture over the warmer surface water. The Walker circulation reinforces the temperature contrast between the eastern and western Pacific.

Figure 1.3 shows two vertical sections of subsurface temperature, one on the equator and one perpendicular to the equator at 180° . The thermocline is clearly visible as a sharp temperature gradient at about 20°C , around 150 m depth in the warm pool and 50 m in the cold tongue. At the same time the sea surface in the warm pool is higher (~ 0.5 m) than in the cold tongue. The force exerted on the water by the surface winds (westward) is balanced by the pressure gradient built up by the sloped thermocline and sea surface. The thermocline is shallower north of the equator due to the location of the ITCZ. Due to variability in thermocline depth the annual mean thermocline shown in figure 1.3 is more diffuse than the instantaneous thermocline.

The equatorial Pacific region has a complex current system. The most prominent is the equatorial undercurrent, an intense eastward current of velocities up to 1 ms^{-1} in the thermocline on the equator. Other examples are the south equatorial current and the north equatorial counter-current. For the analysis of SST along the equator it is important to realize that there is a mean westward surface current on the equator.

1.2. El Niño – Southern Oscillation

The complicated behavior of the isotherms in the right hand side panel of figure 1.3 is related to the existence of these currents.

We continue with a description of the seasonal cycle in the tropical Pacific. Although the sun passes over the equator twice per year, the seasonal cycle in the central and eastern equatorial Pacific is dominated by an annual component. Figure 1.4 shows the mean SST ($^{\circ}\text{C}$) and wind stress (Nm^{-2}) for the months January, April, July and October, using data from the ERA40 reanalysis project (Uppala and coauthors, 2005). Strong changes also occur in sea level pressure and rainfall (see e.g. Philander, 1990, who gives a detailed description of the seasonal cycle). These changes are caused by a shift in strength and position of the two convergence zones, the ITCZ and the SPCZ. In January the SPCZ is well developed with intense convection, whereas the ITCZ is weak around 5°N . The strongest easterly winds occur around 10°N . On the equator in the eastern Pacific wind speeds are low and upwelling is weak, resulting in a warming of the cold tongue with the highest temperatures in March. In July the SPCZ is much weaker, while the ITCZ is well developed around 10°N . The strongest easterly winds occur south of the equator. On the equator wind speeds are higher and upwelling has increased in strength, resulting in a cooling of the cold tongue with the lowest temperatures in August. The seasonal cycle in the warm pool region is very weak, with small changes in surface temperature and mean winds. The wind in the warm pool region is more variable during the northern hemisphere winter, an important aspect for the onset of El Niño. Below the sea surface the effects of the seasonal cycle are small.

1.2.3 The ENSO pattern and cycle

ENSO is described in terms of deviations from the mean seasonal cycle, called “anomalies”.

Figure 1.5 shows the standard deviation of monthly SST anomalies in the equatorial Pacific, computed from ERA40 reanalysis data (Uppala and coauthors, 2005) for the period 1958–2002. Before 1981 the SST data originates from the Global sea Ice Coverage and Sea Surface Temperature dataset (GISST, Parker et al., 1994) from the U.K. Meteorological Office, after 1981 data from Reynolds and Smith (1994) is used. The pattern in figure 1.5 mainly represents ENSO SST variability: other mechanisms inducing SST variability in the equatorial Pacific are much weaker than ENSO. To obtain a single number indicating the current state of El Niño, SST anomalies are averaged over a region resulting in an index. Three regions are commonly used for this purpose: the Niño3, Niño3.4 and Niño4 regions shown in figure 1.1. The Niño3 index describes SST variability in the cold tongue, the Niño3.4 describes the central Pacific region. Both represent the strength of El Niño well. The Niño4 index describes SST variability near the edge of the warm pool region in the central/western Pacific.

The SLP anomaly pattern associated with El Niño can be visualized by computing the correlation between SLP and the Niño3.4 index, shown in Figure 1.6. The pressure difference between the western and eastern equatorial Pacific is clearly visible. To obtain an index for SLP similar to the Niño3.4 index, the normalized difference between the normalized sea level pressure in Darwin and Tahiti (marked by dashed

Chapter 1. Introduction

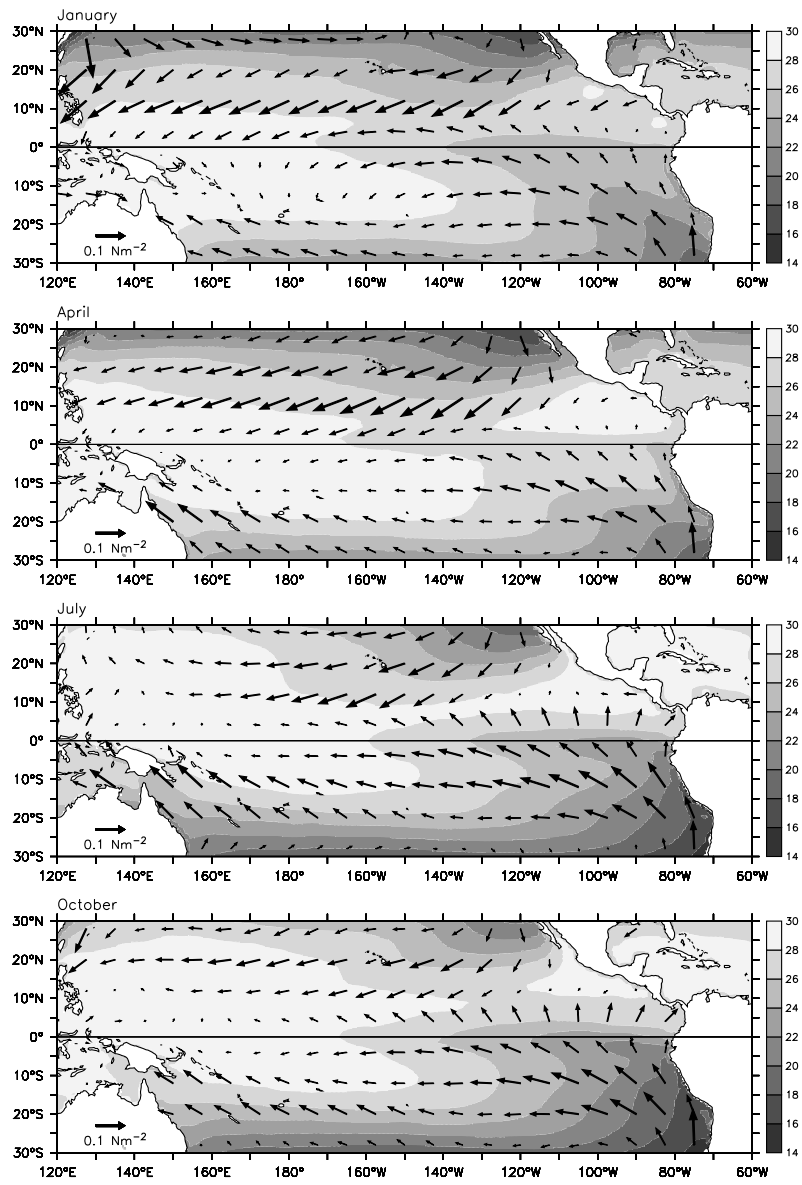


Figure 1.4: Mean SST ($^{\circ}\text{C}$) and wind stress (Nm^{-2}) in the equatorial Pacific for the months of January, April, July and October.

1.2. El Niño – Southern Oscillation

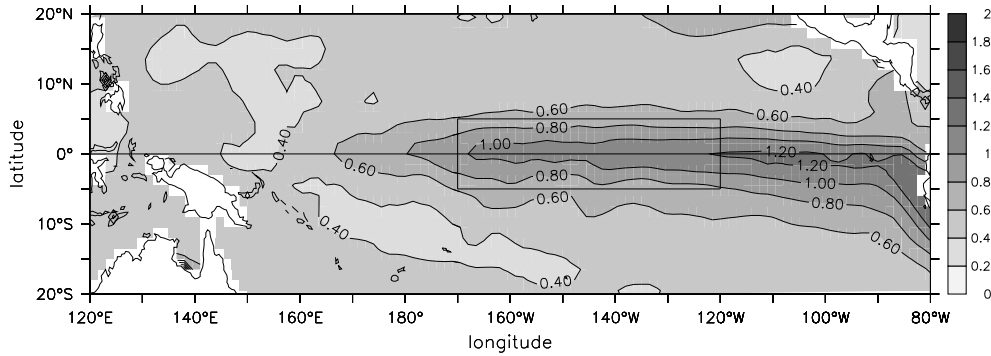


Figure 1.5: Standard deviation of monthly SST anomalies in the equatorial Pacific. ERA40 reanalysis data for the period 1958–2002 was used for the computation. The Niño3.4 region is indicated by a black box.

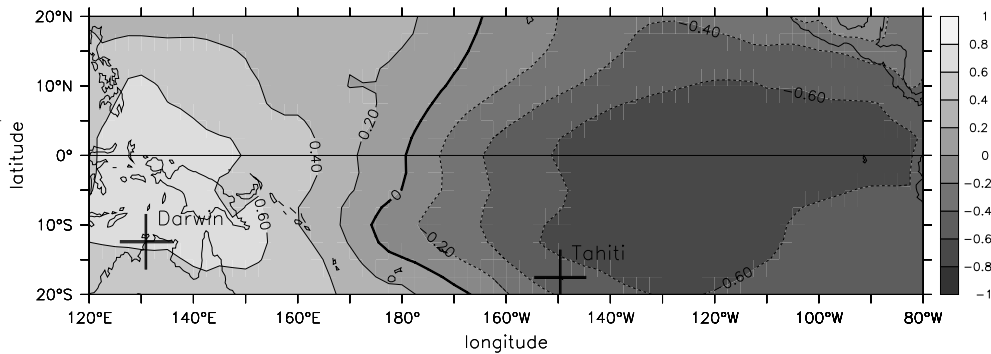


Figure 1.6: Correlation between SLP and the Niño3.4 index. ERA40 reanalysis data for the period 1958–2002 was used for the computation. Darwin and Tahiti are marked by crosses.

crosses in figure 1.6) is computed. These two stations were chosen because long homogeneous timeseries of SLP were available. The resulting time series is called the Southern Oscillation Index (SOI). The Niño3.4 index and SOI are not perfectly opposed, as can be seen in figure 1.7: after smoothing the SOI with a 6 month running mean filter, the correlation coefficient of the two indices is -0.74 for the period 1866–2003. The correlation is -0.86 for the period 1958–2003, the difference is mostly due to more accurate SST measurements.

Figure 1.7 shows that the ENSO cycle is irregular. The amplitude of both El Niño and La Niña varies from event to event, as well as the frequency of the oscillation. On average an El Niño event occurs every 3-7 years. A spectrum of the Niño3.4 index is shown in figure 1.8. SST anomalies are consistently stronger during El Niño than during La Niña, especially in the Niño3 region (Burgers and Stephenson, 1999):

Chapter 1. Introduction

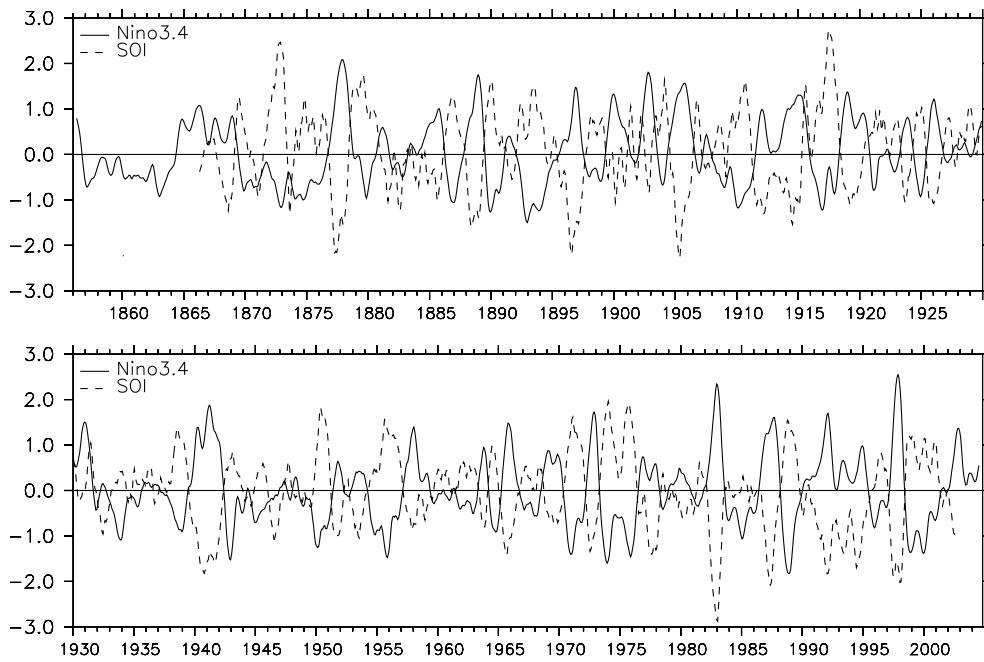


Figure 1.7: The Niño3.4 index (Kaplan et al., 1998; Reynolds et al., 2002) and the SOI (Allan et al., 1991). The data was smoothed with a 6 month running mean filter. The two indices are highly anti-correlated.

1.2. El Niño – Southern Oscillation

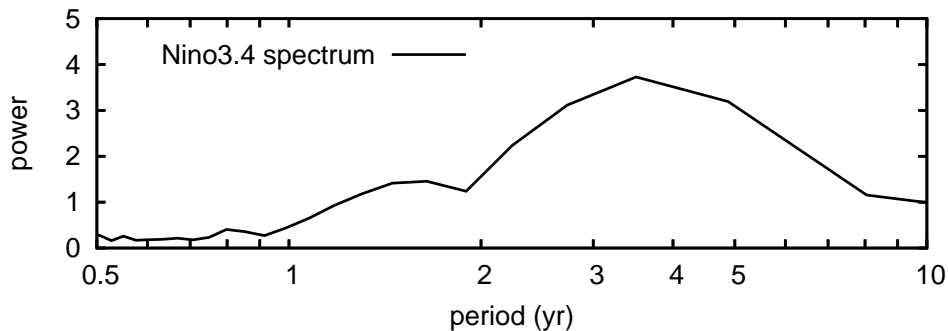


Figure 1.8: A power spectrum of the Niño3.4 index (Kaplan et al., 1998; Reynolds et al., 2002), computed for the period 1856–2004. On average an El Niño event occurs every 3-7 years.

ENSO is said to be “skewed”.

El Niño is locked to the seasonal cycle (e.g. Tziperman et al., 1997): the peak of El Niño almost always occurs around December, as the name “Christ child” implies. The complete transition through El Niño and La Niña takes approximately 2 years, with El Niño starting around northern hemisphere spring of the first year and La Niña starting around spring of the second year. There are several cases however where the El Niño state persisted for two (1905/06, 1914/15) or three (1940/41/42) years.

1.2.4 Teleconnections

The main reason for the attention El Niño receives, is that it has implications on the weather conditions in large parts of the world (Ropelewski and Halpert, 1987; Kiladis and Diaz, 1989). Such remote effects of El Niño are called teleconnections, and will be described in this section. Two important variables of the weather that are affected by El Niño are temperature and rainfall. Heat waves and droughts can result in ruined crops and forest fires, increased rainfall can cause flooding. Positive effects also occur: increased rainfall in areas that are normally dry, and milder winters in otherwise cold areas.

To visualize teleconnections of ENSO, we show the correlation between rainfall or temperature and Niño3.4. Observations from meteorological stations (Vose et al., 1992) are used for rainfall and temperature data, the Niño3.4 index is from Kaplan et al. (1998) before 1958 and Reynolds et al. (2002) from 1958 onward. Figure 1.9 shows the effects of El Niño on (the logarithm of) rainfall, figure 1.10 shows the effects on temperature. The panels show the correlation for different seasons: December - February (bottom left), March - May (top left), June - August (bottom right) and September - November (top right). It is important to realize that a positive correlation between rainfall and Niño3.4 does *not* mean it always rains more during El Niño. For correlations weaker than 0.6 natural variability is more than twice as

Chapter 1. Introduction

strong as the effect of El Niño, so the effect will only be visible when averaging over several El Niño years or during exceptionally strong El Niño events. Furthermore, the correlation coefficient only shows the linear relation with El Niño. This generally works well for the logarithm of rainfall but not always for temperature, for example the teleconnections to winter temperatures in North America.

The strongest ENSO teleconnections occur at the peak of El Niño, in northern hemisphere autumn and winter. The first clear effects occur earlier, in northern hemisphere summer. In Indonesia this is the dry season, figure 1.9 shows that during El Niño rainfall is even lower than normal. This is caused by the eastward shift of the convective region with rainfall, which is now situated over the Pacific. The onset of the monsoon (normally around October) is delayed, resulting in severe droughts in eastern Indonesia. This is not really a *remote* teleconnection, but it is one of the strongest effects of El Niño. Rainfall is also reduced in India (at the end of the summer monsoon around September), but this effect is much weaker than the Indonesian droughts. On the eastern side of the Pacific, the northern coast of South America is on average somewhat dryer than normal, with higher than normal temperatures all along the west coast.

As El Niño approaches its peak in northern hemisphere fall, the teleconnections become stronger and more widespread. Kenya and Rwanda often get more rainfall than normal as the short rains (October – November) are enhanced. Kazakhstan (central Eurasia) on average receives a bit more rainfall than normal. Northern India is still dryer than normal, but Sri Lanka receives more rainfall. All these effects are relatively weak: with correlation coefficients $r < 0.5$ they are approximately 3 times smaller than natural variability. Further east the effects are stronger: droughts persist over most of Indonesia, but rainfall returns to normal when the delayed monsoon sets in.

Past the peak of the event in northern hemisphere winter the effects of El Niño become noticeable in North America, where Florida, Texas and northern Mexico get more rainfall than normal and somewhat lower temperatures. The winter in the northern United States and Canada is often warmer than normal, in contrast to Kamchatka (eastern Russia) where temperatures are even colder than normal. Drought persists in the Phillipines. Temperatures are high in a broad band along the equator: west Africa, southeast Africa, India, north Indonesia, east Australia and South America are all warmer than normal.

In northern hemisphere spring following the El Niño event most teleconnections have weakened. The Phillipines receive somewhat less rainfall than normal, and the northern part of South America is warmer. The northwest coast of North America is warmer than normal, the southern states remain somewhat colder. The southwest receives more rain than normal.

Europe is almost completely unaffected by El Niño. Exceptions are a slight increase in rainfall for Spain and Portugal in autumn, and a weak but significant increase in rainfall in northwest Europe in spring (van Oldenborgh et al., 2000).

1.2. El Niño – Southern Oscillation

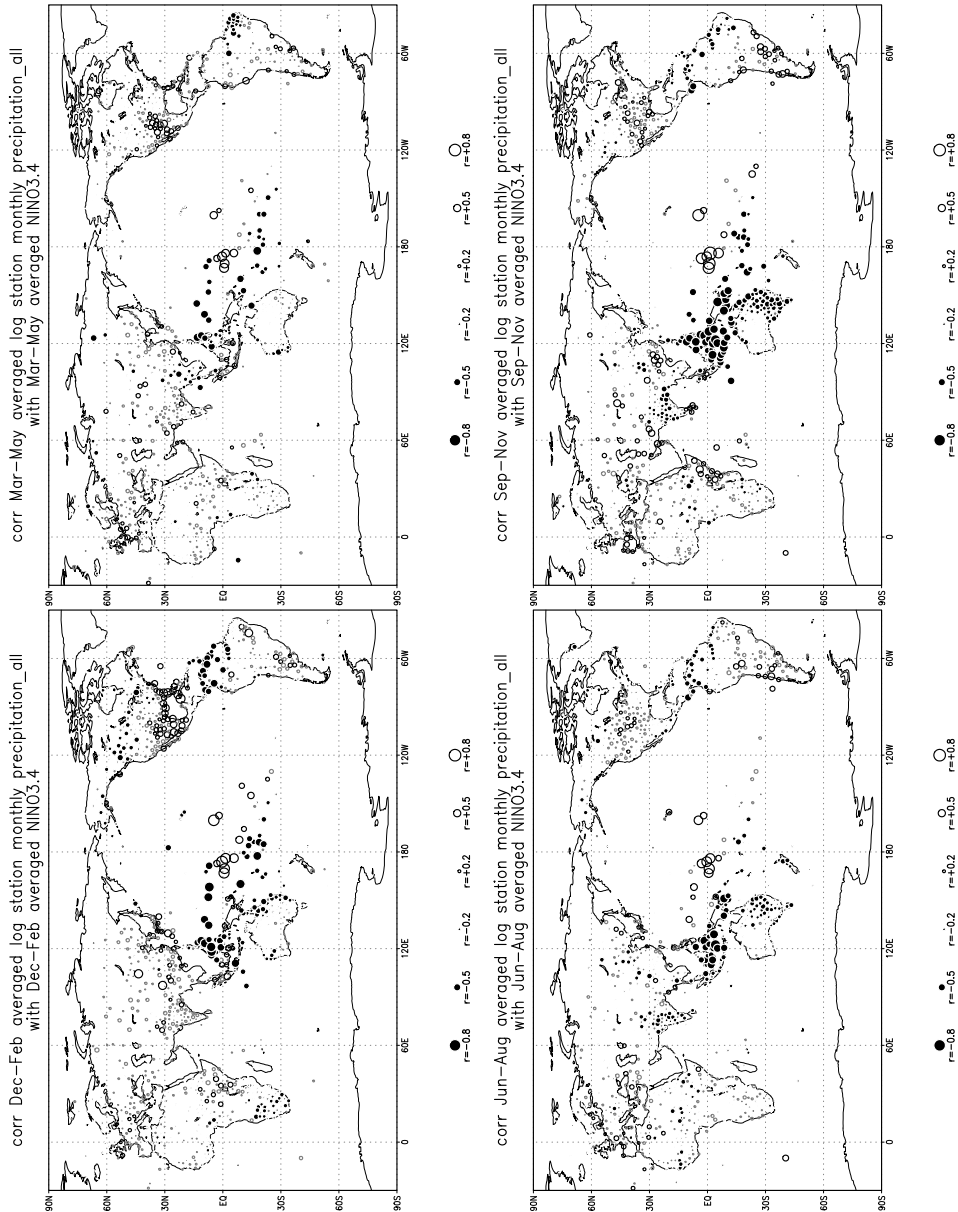


Figure 1.9: ENSO teleconnections: the correlation between Niño3.4 and the logarithm of rainfall, using station observations. The strength of the correlation is indicated by the size of the circle. More rainfall during El Niño (and less during La Niña) is indicated by an open circle, drought during El Niño by a filled circle. Non-significant correlations are indicated by gray circles. Bottom left: December - February, top left: March - May, bottom right: June - August, top right: September - November. The figures were generated with the KNMI Climate Explorer, <http://climexp.knmi.nl>

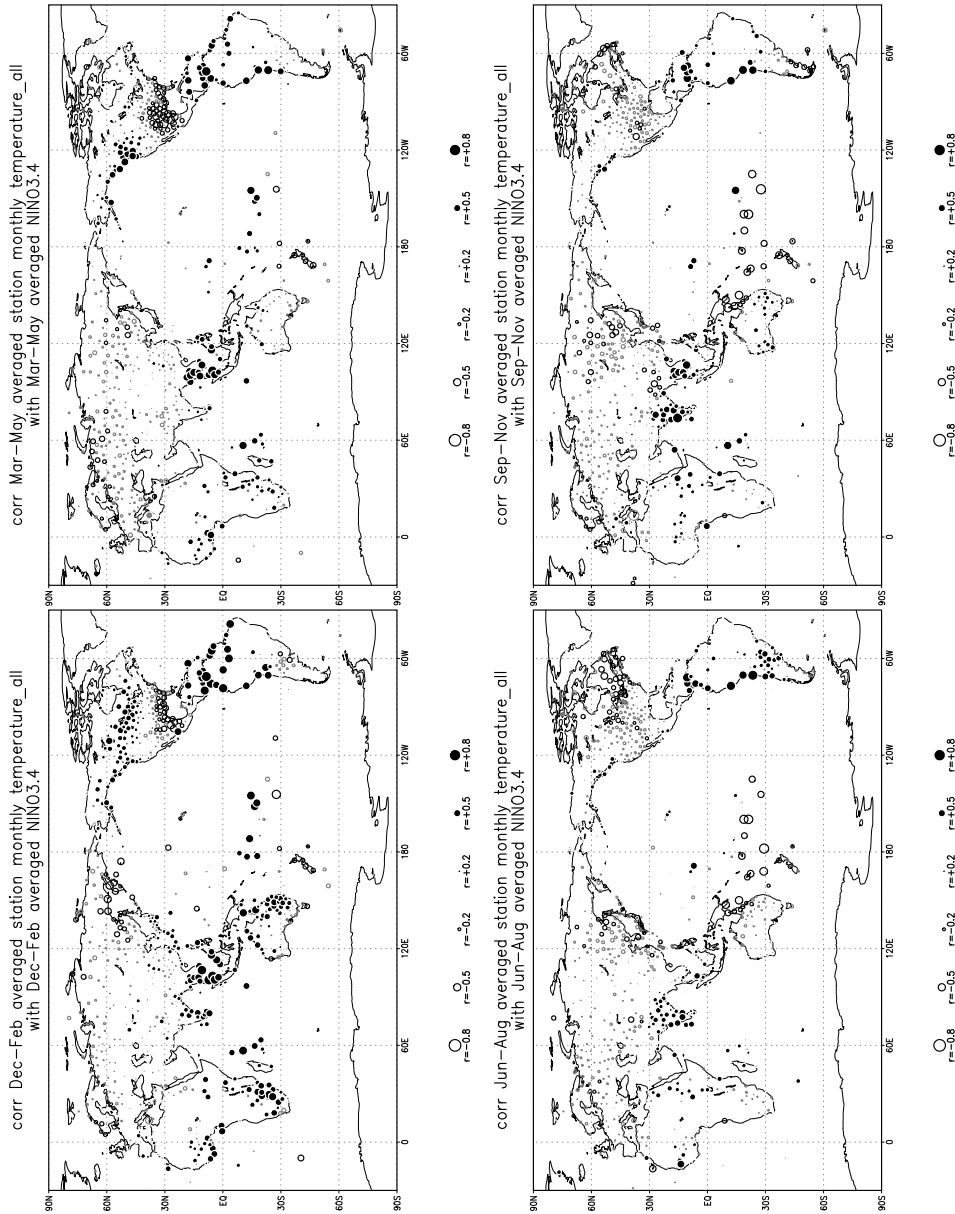


Figure 1.10: ENSO teleconnections: the correlation between Niño3.4 and temperature, using station observations. The strength of the correlation is indicated by the size of the circle. Higher temperatures during El Niño (and lower during La Niña) are indicated by a filled circle, lower temperatures during El Niño (and higher during La Niña) are indicated by an open circle. Non-significant correlations are indicated by gray circles. Bottom left: December - February, top left: March - May, bottom right: June - August, top right: September - November. The figures were generated with the KNMI Climate Explorer, <http://climexp.knmi.nl>

1.3 Mechanisms, processes and feedbacks

In this thesis a detailed investigation of some aspects of the ENSO cycle is performed. As an introduction to this investigation, a qualitative description of the ENSO cycle and the basic mechanisms is given in section 1.3.1. After that, the most important processes will be discussed in some more detail, and two views commonly used to describe ENSO are presented.

1.3.1 Basic mechanisms

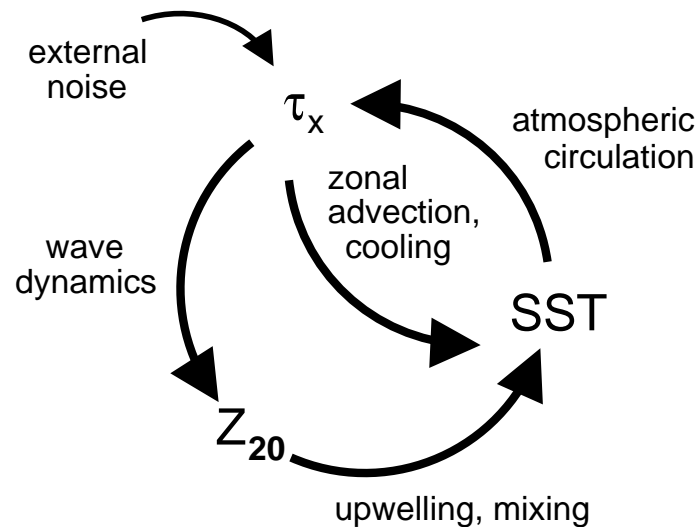


Figure 1.11: The main feedbacks in the ENSO cycle. Z_{20} denotes the thermocline depth in the eastern Pacific and τ_x the zonal wind stress.

The interactions that drive El Niño – Southern Oscillation (ENSO) are sketched in Figure 1.11. To describe a complete cycle of El Niño followed by La Niña, we imagine that the equatorial Pacific is in a state close to the climatological situation in January, as shown in figures 1.3 and 1.4. The easterly trade winds over the equator push the surface waters to the west. The force exerted by the wind is balanced by the pressure gradient resulting from the sloped thermocline and sea surface. This balance can be disturbed by anomalous westerly winds, for example a storm (see below). This is represented in figure 1.11 by a positive τ_x anomaly. The westerly wind anomaly effectively reduces the trade winds, leading to a reduction of the slope of the thermocline, deeper in the east, somewhat shallower in the west. The deepened thermocline in the eastern Pacific causes SST to increase, represented by a positive SST anomaly in figure 1.11. The strength of the trade winds is reduced: the Walker

Chapter 1. Introduction

circulation is weakened because the east-west temperature difference is reduced. This reinforces the initial westerly wind anomaly, and a positive feedback loop (the outer circle in figure 1.11) has been formed (Bjerknes, 1966). The anomalous westerly wind in the western and central Pacific also increases local SST directly, through several mechanisms discussed in section 1.3.3. This reinforces the positive SST anomaly in the central Pacific, shifting the 28°C isotherm to the east together with the region of atmospheric convection and rainfall. The inner feedback loop in figure 1.11 is completed as the westerly winds increase, drawn by the increased convection and corresponding low pressure in the central Pacific.

The results of these two feedbacks are increased SST in the central and eastern equatorial Pacific, a reduced thermocline slope and a shift of the convective region shifts toward the central equatorial Pacific, as shown in the bottom panel of figure 1.2.

A system will not oscillate without a negative feedback: the growth of SST anomalies in the eastern Pacific reverses at some point. There are two well known views of the mechanism by which the process is reversed, described by Suarez and Schopf (1988) and Battisti and Hirst (1989) in the “delayed oscillator” model, and by Jin (1997) in the “recharge oscillator” model. These models are discussed in section 1.3.2. In both views the reduced slope of the thermocline during El Niño causes geostrophic adjustment, which results in shoaling of the thermocline. This eventually leads to a reduction of the SST anomalies in the central and eastern Pacific.

As SST anomalies in the eastern Pacific are reduced, the zonal temperature gradient is increased and in response the easterly trade winds pick up strength. The convective region moves westward with the 28°C isotherm. The reverse process does not stop when SST is back to normal: it brings the system into a La Niña state. SST in the eastern Pacific is now colder than normal, the easterly trade winds are stronger and the sea surface and thermocline slopes are steeper than normal. Eventually the La Niña decays and the system swings back through the “normal” state. The interactions between surface wind, thermocline depth and SST are rather complex. They will be discussed in more detail in sections 1.3.2 and 1.3.3.

The above description does not specify what causes the fluctuations in westerly winds that can make the difference between an El Niño event developing in one case and not in another case. These westerly wind events are caused by a variety of physical mechanisms. Some are associated with the Madden-Julian oscillation (Madden and Julian, 1971), a wave in the atmosphere traveling along the equator around the globe with a 30 to 60 day period, generating low pressure systems in the Indian ocean and western Pacific. Another possibility is a tropical cyclone, which occurs somewhat off the equator. Due to the Coriolis force the prevailing wind on the equator caused by a cyclone is westerly. It is currently not clear to what extent the westerly wind events are purely weather “noise” and to what extent they are part of a (non-linear) aspect of ENSO.

In most cases El Niño can be said to lead the cycle, with La Niña a response to the previous El Niño. Although the transition through the El Niño–La Niña phases generally takes two years, the time between two distinct El Niño events can be much longer due to the irregularity of the oscillation. To visualize this behavior, ENSO can be modeled as a damped oscillator with two variables: the SST anomaly in the eastern

1.3. Mechanisms, processes and feedbacks

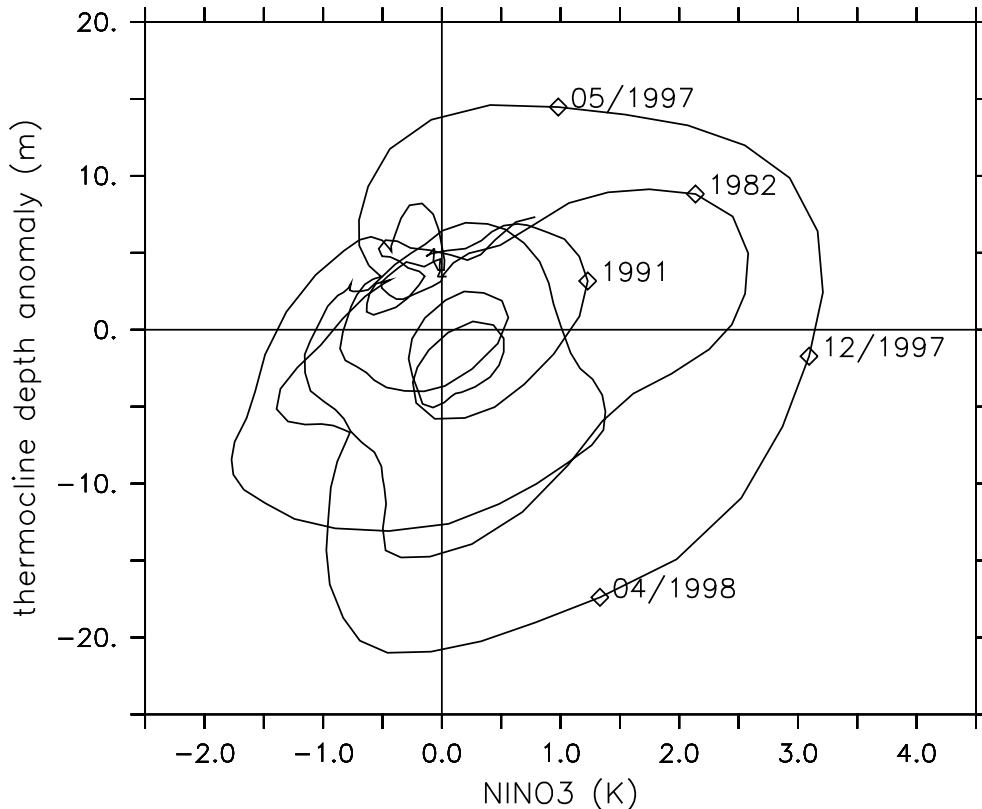


Figure 1.12: A phase diagram of SST anomalies in the eastern equatorial Pacific (Niño3) and the zonally averaged thermocline depth anomaly, representing warm water volume in the equatorial Pacific. Time increases clockwise along the trajectory.

Pacific (T , we use the Niño3 index) and the mean thermocline depth anomaly across the equator (h), also called warm water volume (WWV) (e.g. Fedorov and Philander, 2001; Kessler, 2002). The slope of the thermocline is not included in the model: on timescales of several months it does not vary independently of the eastern Pacific SST. Although this is a simplification, these variables can represent the basic El Niño oscillation well.

The oscillation can be visualized in a scatter plot of T against h , a regular damped oscillation without noise would form a spiral toward the origin. Figure 1.12 shows such a diagram for observations over the period 1980–2002. The basic shape of a clockwise spiral is recognizable, but the ENSO oscillator receives a “kick” now and then, usually in the upper left quadrant. The development of the 1997/98 El Niño starts with such a kick in the upper left quadrant, as h grows due to a series of westerly wind events drawing water to the equator (McPhaden, 1999). The onset is in March 1997, entering the upper right quadrant as positive SST anomalies develop.

The decay phase in the first half of 1998 is in the lower right quadrant, and the 1998 La Niña is in the lower left quadrant. During the cycle h leads T with a phase difference of approximately 90° . After La Niña, ENSO often remains close to the origin and mostly in the upper left quadrant. This can last several years, a positive h anomaly building up constitutes the start of a new cycle.

The physical processes that play a role in the links between thermocline depth, SST and surface winds are introduced in the next subsection. In this thesis we are specifically interested in the delayed coupling between thermocline depth anomalies and SST, investigated in chapter 2, and the surface heat budget that leads to the characteristic SST evolution of an El Niño event, investigated in chapter 3.

1.3.2 The effect of thermocline depth anomalies on SST

We have seen that variations in the depth of the thermocline in the equatorial Pacific are important for El Niño. Such variations are best understood by thinking of the equatorial Pacific as a layer of cold bottom water, with a warm layer on top. The bottom layer is stagnant, the top layer is in motion and has a variable depth. The interface between the two layers represents the thermocline. Horizontal motion of the upper layer and variations in layer depth are given by the shallow water equations for an equatorial β -plane (an approximation where the Coriolis parameter f varies linearly with latitude, $f = \beta y$ with β a constant). The linearized form of the equations is given by

$$\frac{\partial u}{\partial t} - fv + g' \frac{\partial h}{\partial x} = 0 \quad (1.1)$$

$$\frac{\partial v}{\partial t} + fu + g' \frac{\partial h}{\partial y} = 0 \quad (1.2)$$

$$\frac{\partial h}{\partial t} + H \left(\frac{\partial u}{\partial x} + \frac{\partial v}{\partial y} \right) = 0 \quad (1.3)$$

where u and v are zonal and meridional velocity, f is the Coriolis parameter, h represents the thermocline depth and H is the mean thermocline depth. g' is the reduced gravity given by $g' = g(\rho_2 - \rho_1)/\rho_1$, where ρ_1 and ρ_2 are the density of the upper and lower layers. Friction, non-linear and forcing terms have been left out of the equation, for a complete description see e.g. Gill (1982, ch. 11).

The shallow water equations have solutions in the form of non-dispersive waves propagating zonally along the equator, for discrete values of the group velocity v . The lowest order solution is the equatorial Kelvin wave (Thomson, 1879; Matsuno, 1966), it travels eastward along the equator at $v = c$ with $c = \sqrt{g'H} \approx 2.5 \text{ m s}^{-1}$. It is trapped on the equator and has a meridional extension of approximately 250 km. Higher order solutions have $v = -c/(2n + 1)$, $n = 1, 2, \dots$, these are off-equatorial Rossby waves traveling westward along the equator. Further away from the equator thermocline depth anomalies are composed of higher order Rossby waves, therefore the westward propagation speed decreases with the distance from the equator. Figure 1.13 shows the characteristic thermocline depth and current patterns of a Kelvin

1.3. Mechanisms, processes and feedbacks

wave and the first order Rossby wave. Kelvin and Rossby waves are excited by surface wind stress anomalies: they are the adjustment process that restores the balance between wind stress and pressure gradient on short time scales.

The shallow water equations tell us how a thermocline depth anomaly propagates, but not how it affects SST. As the thermocline is a sharp vertical temperature gradient, subsurface temperatures are directly affected when the thermocline deepens or shoals. In the eastern equatorial Pacific where the thermocline is relatively shallow and there is mean upwelling, subsurface temperature anomalies formed by thermocline depth anomalies are propagated upward by a combination of upwelling and diffusion, and eventually appear at the surface as SST anomalies. It takes 2 weeks or more for a subsurface temperature anomaly at the depth of the thermocline to reach the surface: the upwelling velocity is only of the order 1 m day^{-1} . This time span depends strongly on variations in thermocline depth and upwelling velocity.

The thermocline forms a delayed positive coupling between westerly wind stress in the western and central Pacific and positive SST anomalies in the eastern Pacific. It takes approximately 6 weeks for a free Kelvin wave to cross the Pacific basin. As discussed by Neelin et al. (1998) however, thermocline depth anomalies will propagate as a forced Kelvin wave under the influence of the zonal thermocline depth slope and zonal wind stress. The effective eastward propagation speed is much slower than the free Kelvin wave speed. Thus, a thermocline depth anomaly can take up to 6 months to cross the Pacific. Once it arrives in the eastern Pacific, mean upwelling will generate a positive SST anomaly. The delay between the generation of a thermocline depth anomaly in the western or central Pacific and the appearance of the SST anomaly in the eastern Pacific is discussed in detail in chapter 2.

In section 1.3.1 it was mentioned that the thermocline provides a negative feedback on SST anomalies in the eastern Pacific. Battisti and Hirst (1989) and Suarez and Schopf (1988) argued that Kelvin and Rossby waves are crucial to sustain an oscillation, the “delayed oscillator”. A westerly wind event in the western Pacific excites both a positive Kelvin wave (deepening) on the equator, and negative Rossby waves (shoaling) off the equator. The Kelvin wave provides a positive coupling between thermocline depth and SST in the eastern Pacific. The Rossby waves travel westward to the coast, which they follow to the equator to form negative (shoaling) Kelvin waves. When these Kelvin waves arrive in the eastern Pacific, the negative thermocline depth anomaly leads to a reduction of the existing positive SST anomaly, forming a delayed negative feedback. Jin (1997) describes the El Niño oscillation in the “recharge oscillator” in terms of the main variables of figure 1.12: the zonal mean thermocline depth or WWV, and SST in the eastern Pacific. During an El Niño event the reduced zonal slope of the thermocline causes Sverdrup transport away from the equator, between the thermocline and the surface. The zonal mean thermocline depth is reduced and eventually upwelling will bring colder water to the surface. The existing positive SST anomaly is reduced and the negative feedback completed. Actually, the delayed oscillator and recharge oscillator are very similar: the main difference is that the delayed oscillator takes only the wave speeds of first order Rossby waves and Kelvin waves into account, while the recharge oscillator also takes into account the effect of higher order Rossby waves. The thermocline provides a delayed positive

Chapter 1. Introduction

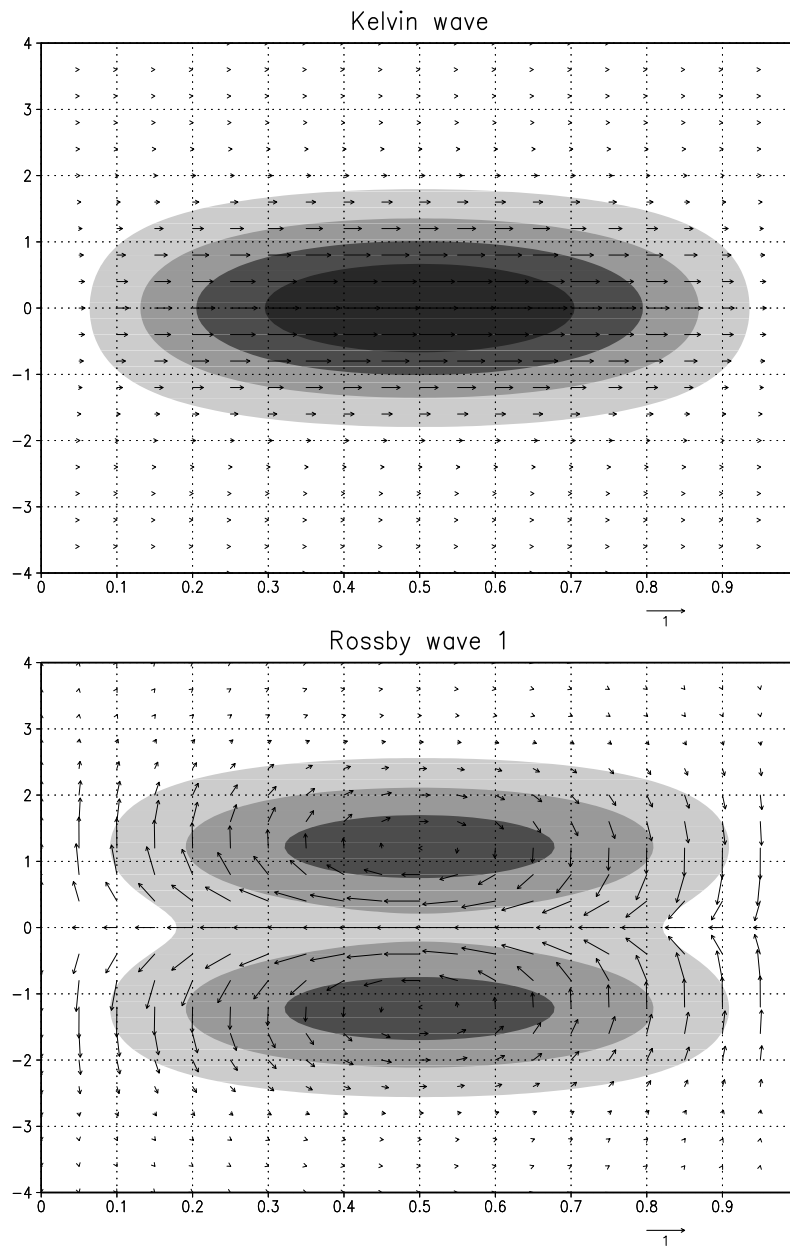


Figure 1.13: The thermocline depth anomaly pattern (shading) and current pattern (arrows) belonging to a Kelvin wave (top) and the first order Rossby wave (bottom). The x axis represents longitude (arbitrary units), the y axis represents latitude in units of the Rossby radius (~ 250 km). The patterns shown are for a positive Kelvin and Rossby wave, darker colors indicate a deepening of the thermocline.

1.3. Mechanisms, processes and feedbacks

coupling between wind stress in the western/central Pacific, thermocline depth and SST in the eastern Pacific. Delayed negative feedback on SST through thermocline depth can occur by waves and meridional advection.

1.3.3 The interaction between wind stress and SST

To understand the effects of surface fluxes on the ocean, it is important to know that the upper layer of the ocean is well mixed: temperature and salinity are approximately constant throughout this layer. SST is thus approximately equal to the temperature of the mixed layer. In the equatorial Pacific this layer has a thickness of approximately 20 m, varying with location and in time. A heat flux applied at the ocean surface (or at the bottom of the mixed layer) is effectively applied over the whole mixed layer thickness, as the heat is distributed across the layer in a very short time. Mixed layer depth variability is caused mainly by changes in surface wind speed and upwelling, a process described in more detail in chapter 3. Because a change in mixed layer depth affects the heat capacity of the mixed layer, it is also important for the development of SST anomalies.

Apart from their influence on thermocline depth as described above (1.3.2), anomalous zonal surface winds have a direct, local effect on SST in several ways. A westerly wind anomaly reduces the mean easterly trade winds, which results in reduced upwelling of cold water on the equator and thus a warming of the mixed layer. Anomalous eastward advection driven by the westerly wind anomaly transports warm water from the west Pacific toward the central Pacific where the mean SST is lower, resulting in warming (Picaut et al., 1997). Finally, because the dominant surface winds in the equatorial Pacific are the easterly trade winds, a westerly wind anomaly significantly reduces the surface wind speed. This results in reduced mixing of deeper, colder water into the mixed layer, as well as reduced evaporation at the surface. Both effects warm the mixed layer, increasing SST. The reduced wind speed also leads to a shoaling of the mixed layer, with implications on SST that are explained in chapter 3.

Wind stress anomalies in the warm pool are partially caused by atmospheric noise (weather), and partially by ENSO. At times when El Niño is weak, atmospheric noise is the dominant factor. During stronger El Niño events, the wind response to convection over the SST anomaly in the central/eastern Pacific is stronger than atmospheric noise. Clarke (1994) shows that the wind response is mostly westerly under the convective region (which lies somewhat west of the maximum SST anomaly), with a weaker easterly wind response east of the convection region. Figure 1.14 shows the zonal wind stress response to a SST anomaly in the central Pacific, computed from ERA40 reanalysis data. At the peak of a strong El Niño event the westerly wind anomalies can extend all the way across the Pacific, canceling the easterly trade winds.

There is a positive interaction between zonal (westerly) wind and SST: anomalous westerly winds are generated by SST anomalies, and reinforce them. The interaction is strongest in the western/central Pacific, not in the Niño3 region. There are several damping effects on SST (for example increased evaporation and reduced incoming solar radiation due to increased cloud cover) which reduce the growth of SST anoma-

Chapter 1. Introduction

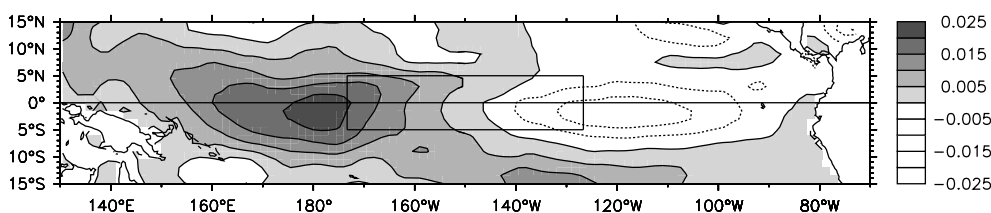


Figure 1.14: Zonal wind stress response to a SST anomaly (represented by the black box) in the central equatorial Pacific, in units of $\text{N m}^{-2} \text{K}^{-1}$. Westerly wind anomalies extend partially over the SST anomaly. The convective region lies somewhat west of the maximum SST anomaly.

lies in the western and central Pacific; the amplitude of El Niño remains largest in the eastern Pacific. The interaction between surface winds and SST in the western and central Pacific and its role in the ENSO cycle is discussed in detail in chapter 3.

1.4 Predicting El Niño

The most important driving mechanisms behind ENSO have been identified. The next step is to choose a model that represents these mechanisms as well as possible, and make numerical predictions of El Niño events. This can be done with a range of very simple to very complex models, and on medium (months) to long (years, decades) timescales.

1.4.1 Models

Models that are currently used for El Niño predictions can be roughly divided in three categories: statistical models, intermediate complexity models and general circulation models of the coupled ocean-atmosphere system.

Statistical models use statistical relationships to predict future ENSO behavior. The simplest models are based on persistence: once the ocean warms up, it takes a long time to cool down again. A good first-guess prediction for SST-related variables is thus that things will stay the same: once the Niño3 region has warmed up it will stay warm for a while and gradually relax back to climatology. The Cliper model (climatology - persistence) is an example of such a model: it predicts the Niño3.4 index based on the current Niño3.4 index and a damping coefficient c for each month and lead time ($c < 1$ except for short lead times during autumn when El Niño tends to grow the most, then $c > 1$). The next step is to add more knowledge of El Niño to the model. Most El Niño events develop in a similar fashion. Thus, once an El Niño event has started (in northern hemisphere spring or summer) this information can be used to forecast the next 9 months until the decay of El Niño. An example is the Constructed Analogue (CA) model by van den Dool (1994); van den Dool and Barnston (1994), which assumes that future El Niño events will be similar to past

1.4. Predicting El Niño

events. It is not based on persistence, instead it fits the observed global SST evolution over the last year to a weighted sum of the years 1956–2001, using positive and negative weights. The forecast is the weighted sum of the evolution of these years. The model is in operational use at the National Centers for Environmental Prediction (NCEP), USA. Another statistical model is the Markov model by Xue et al. (2000), based on a damped oscillator similar to the one described in section 1.3.1. It uses patterns of sea level, zonal wind and SST in the tropical Pacific as variables. This model is also in operational use by NCEP.

Intermediate complexity models are generally based on the shallow water equations 1.1–1.3, they typically simulate only one or two vertical layers in the ocean and atmosphere. The best known example is the Zebiak-Cane model (Zebiak and Cane, 1987), which consists of a linear shallow water ocean model with a non-linear SST equation, coupled to a linear Gill-type atmosphere model (Gill, 1980) with non-linear heating. Chen et al. (2004) report skill in forecasting large El Niño events up to two years in advance with a recent version of this model. The Gmodel (Burgers et al., 2002) is another intermediate complexity model: it consists of a linear shallow water ocean model with a linear SST equation, coupled to a linear statistical atmosphere based on the Niño3 and Niño4 indices and two wind response patterns. To produce a forecast these models are initialized with current observations as well as possible, after which a coupled ocean-atmosphere simulation is started with the length of the forecast period. The models are simple and fast, and can be run for long periods of time if desired.

The last category, general circulation models (GCM), use the primitive equations of motion (the Navier Stokes equations, with hydrostatic and Boussinesq approximations) to simulate both atmosphere and ocean. These models are generally complex, many physical processes that occur on scales smaller than the resolution (typically around 100 km) are parameterized, for example air-sea interaction and cloud formation in the atmosphere. An important difference with intermediate complexity models is that GCM's use a grid with many layers in the vertical for both ocean and atmosphere. To obtain the best initial state for a forecast simulation, modern GCM's make use of a process called data assimilation. A simulation of the past years is performed, during which the model is corrected using observational data. The data assimilation run stops at the present time, and provides the initial state for the forecast. Institutes that use a GCM for operational El Niño forecasts are amongst others the European Centre for Medium-range Weather Forecasts (ECMWF) and the Met Office in the UK, and the National Centers for Environmental Prediction (NCEP) in the USA. The current model used at ECMWF for seasonal forecasts and ENSO forecasts is called System-2. The atmosphere component is a low resolution version of the model used to produce daily weather forecasts.

1.4.2 ENSO Forecasts

The ENSO forecast we are most interested in is the seasonal forecast: will there be an El Niño event this year, and how will it develop? Ideally, this question should be answered in the winter before the onset of El Niño or earlier. To see how the

Chapter 1. Introduction

models perform, forecasts of the Niño3.4 index at lead times of 1 month, 3 months and 5 months are compared with the observed Niño3.4 index, for the period 1987–2002. The lead time is defined as the period between the analysis (last observations used) and the start of the period we want to forecast. A forecast for the month May using observational data from January 31 is said to have a lead time of 3 months. Operational forecasts for the period 1987–2002 are not available for each of these models, in those cases a hindcast (a forecast starting at a point in the past) is used instead. Figure 1.15 shows the results for the Cliper model, the Markov model, the Gmodel and the ECMWF System-2 (S2) model, for forecast start times in the period 1987–2001. The forecasts were obtained from the model authors, the analysis is described in van Oldenborgh et al. (2005).

At first sight the Cliper model (figure 1.15a) performs quite well, but it does not capture the onset of El Niño and La Niña: the forecast is always lagging behind. The Markov model (figure 1.15b) is better at capturing the onset of El Niño although it still lags behind, and the onset of the 1998 La Niña was captured correctly. The Gmodel (figure 1.15c) is better at predicting the onset of El Niño and La Niña, but because it is linear it cannot capture the asymmetry between El Niño and La Niña: it underestimates El Niño amplitudes and overestimates La Niña amplitudes. The ECMWF System-2 model (figure 1.15d) generally captures the onset of El Niño and La Niña episodes quite well. The amplitude of the 1997/98 event was underestimated, otherwise the System-2 prediction of the Niño3.4 index is one of the best available.

The real merit of predicting El Niño with a GCM is clearly its ability to predict the onset of El Niño and La Niña correctly. This becomes visible when the seasonal dependence of the prediction skill is shown. Once an El Niño event is developing (in northern hemisphere autumn, winter and spring) it can be predicted relatively easily through the first, fourth and third quadrants of figure 1.12. The onset in spring is much harder to predict: persistence of SST is low during this season, this is often called the “spring barrier”. Figure 1.16 shows the skill of the different models in predicting the Niño3.4 index (computed as the correlation coefficient between observation and simulation, 0 is no skill, 1 is perfect) at a lead time of +3 months, as a function of the season. During the spring barrier (June/July predicted in March/April) the Cliper model has a skill of ~ 0.2 , whereas the System-2 model has a skill of ~ 0.8 . The Gmodel performs much better than the Cliper model with a minimum skill of ~ 0.7 , but is outperformed by the GCM. The skill scores have large error margins due to the short period (there are only 5 El Niño events between 1987 and 2002), however the increase in skill from statistical models to intermediate complexity models to GCM’s is robust. Models based on persistence of SST (Cliper) clearly cannot predict through the spring barrier. The reason why intermediate complexity models and GCM’s perform better is that they contain subsurface information: there is persistence and predictability in the simulated thermocline depth and subsurface temperature fields. Another important benefit of using a coupled GCM for ENSO forecasts, is that the detailed SST forecast combined with the atmosphere model make it possible to compute the effects of anomalous SST on the atmospheric circulation in more detail. In principle this leads to better seasonal forecasts of the weather around the world than simple ENSO teleconnections.

1.4. Predicting El Niño

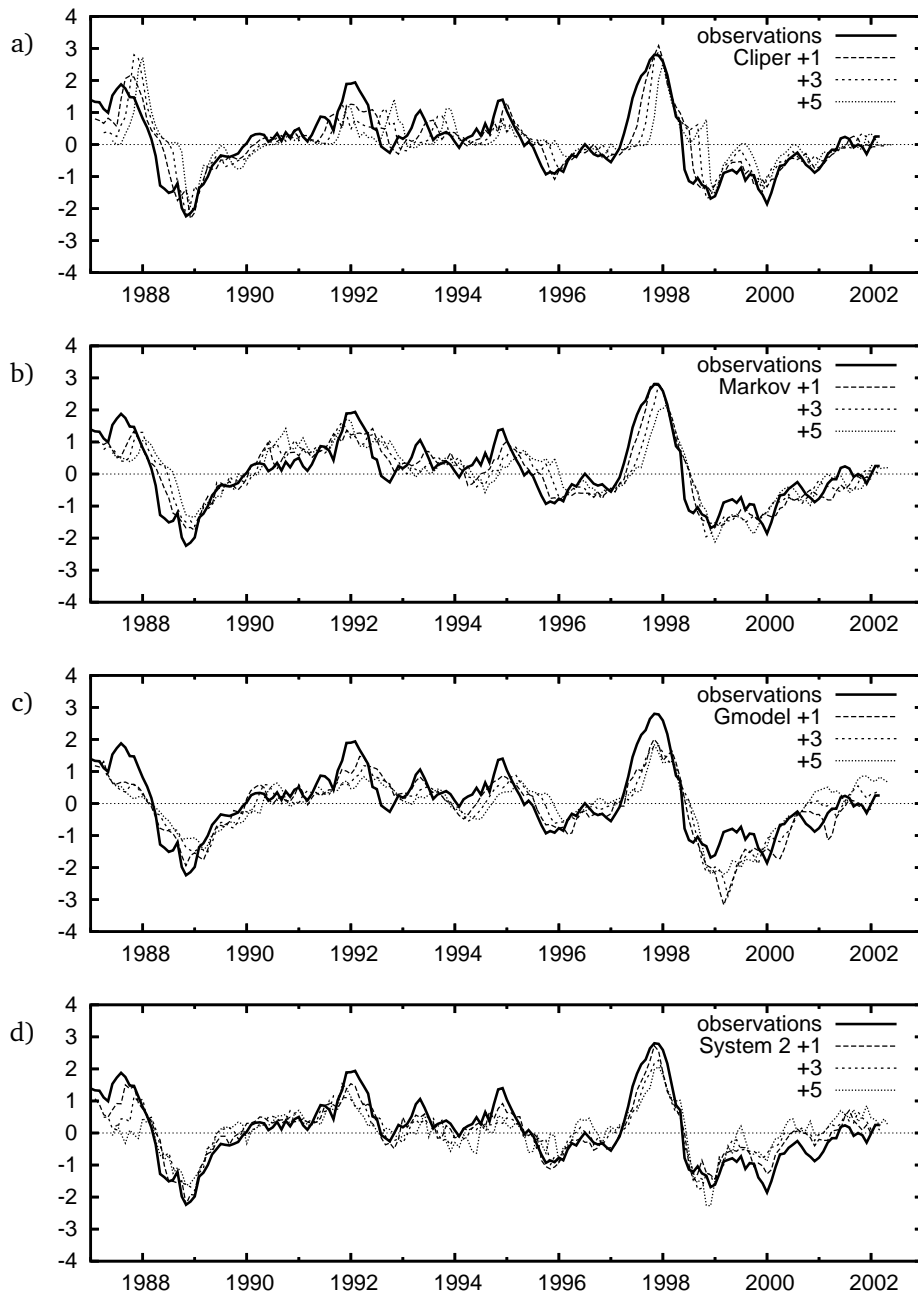


Figure 1.15: Niño3.4 forecasts at lead times of 1 month, 3 months and 5 months. a) Cliper, a statistical model based on persistence. b) The Markov model, based on a 3-variable damped oscillator. c) The Gmodel, a linear shallow water model coupled to a statistical atmosphere model. d) The ECMWF System-2 general circulation model.

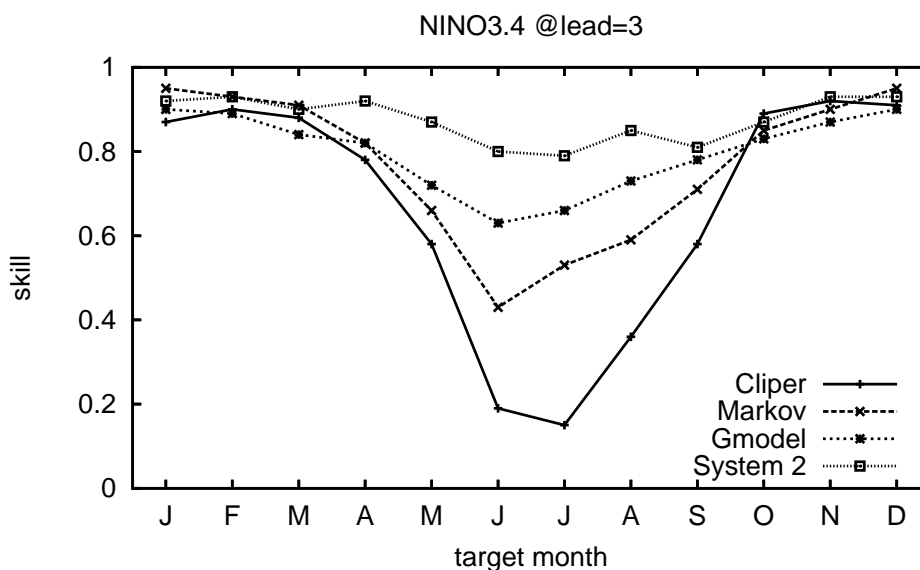


Figure 1.16: The skill in predicting the Niño3.4 index at a lead time of +3 months

Concluding, current GCM's are significantly better at predicting El Niño than simple statistical models, and the results are still improving as new models are being developed. Forecasting the onset of El Niño remains difficult, but in most cases El Niño and La Niña are predicted with reasonable accuracy at lead times of +3 months or more.

1.4.3 The effect of global change

Another matter of interest is how El Niño will respond to global warming due to the enhanced greenhouse effect. It is not easy to predict how ENSO will change as the background temperature increases. A hypothetical scenario could be as follows:

Global warming does not occur evenly throughout the globe: the poles show stronger warming than the equator. This reduces the meridional temperature gradient between the equator and the poles. The Hadley circulation is driven by this temperature gradient, and may weaken as a result, resulting in a weakening of the trade winds in the equatorial Pacific. Together with the rising mean temperature, the weakened trade winds will cause the warm pool region and the 28°C isotherm to move eastward into the central Pacific. The region of atmospheric convection will expand to the central Pacific as well.

One could thus expect an eastward shift in the pattern of El Niño variability. However, the increased size of the convective region may also strengthen the Walker circulation

1.5. This thesis

and the equatorial trade winds, partially canceling the effect of the weakened Hadley circulation and reducing the eastward expansion of the convective region.

There is currently no agreement on how El Niño will change under the effect of global warming (IPCC, 2001; Collins and coauthors, 2005). Several models predict that ENSO will stay approximately the same, but other models predict a change toward a more El Niño-like state or toward a more La Niña-like state. There may be changes in the mean state of the equatorial Pacific region (SST, trade winds, the location of the convective region) but also in the variability (amplitude, frequency, regularity and skewness) of ENSO. In chapter 4 this problem is addressed in more detail.

1.5 This thesis

Detailed observations of the tropical Pacific are finally available for a period sufficiently long to contain several full El Niño–La Niña cycles. This enables us to study and verify mechanisms quantitatively, something which was not possible before. Such analyses will increase our understanding of the mechanisms behind El Niño, which can eventually lead to improved ENSO forecasts.

Chapter 2 focuses on mechanisms related to thermocline depth variability, as described in section 1.3.2. The connection between thermocline depth anomalies and SST anomalies is investigated in detail. There is a time delay between a local thermocline depth anomaly and the resulting SST anomaly at the surface. The delay varies with longitude. An analysis of this delay leads to a better understanding of the balance between wind driven mechanisms (zonal advection, evaporation) in the surface layer and upwelling of subsurface temperature anomalies in the generation of SST anomalies along the equator. The analysis results in a useful method to verify the quality of model El Niño simulations. One of the main results from chapter 2 is that wind related mechanisms (as described in section 1.3.3) are dominant in the generation of SST anomalies in the western and central equatorial Pacific.

The relation between surface winds and SST anomalies in this region is discussed in more detail in chapter 3. In a budget study, it is shown how SST anomalies propagate zonally from the western Pacific to the central/eastern Pacific and back during the development and decay of an El Niño event. The mechanisms that cause the growth and zonal movement of SST anomalies are determined using an ocean model simulation. The analysis emphasizes the importance of wind-related mechanisms during the development of El Niño. Mixed layer depth anomalies turn out to be an important factor in the development of SST anomalies in the western and central equatorial Pacific. A better understanding is gained of the processes responsible for the onset and decay of an El Niño event. This provides a framework for assessing the performance of general circulation models in a region where many models have problems.

Chapter 4 deals with the question “How does El Niño change under the influence of human induced global warming?” discussed in section 1.4.3. An analysis is performed that makes use of data from the “Dutch Challenge Project”: an ensemble of 62

Chapter 1. Introduction

model simulations over the period 1940–2080. The goal of the project is to analyze the effects of a (modest) future greenhouse scenario on the earth climate system. A statistical analysis of several ENSO-related variables within this dataset is performed, for each individual ensemble member and for the ensemble mean. The results indicate no significant changes in ENSO characteristics, despite a global average warming of $\sim 1.5\text{K}$. A detailed investigation is performed to find out why El Niño is insensitive to global warming in this model, and if the outcome is likely to be true for the real El Niño. The analysis leads to a conclusion about the value of this model simulation for predicting future changes in ENSO due to global warming. A recommendation for model improvement (for this model and other coupled models) is formulated.

Chapter 2

SST and thermocline depth

The time dependence of the local relation between sea surface temperature (SST) and thermocline depth in the central and eastern equatorial Pacific is analyzed for the period 1990 – 1999, using subsurface temperature measurements from the TAO/TRITON buoy array. Thermocline depth anomalies lead SST anomalies in time, with a longitude dependent delay ranging from two weeks in the eastern Pacific to one year in the central Pacific. The lagged correlation between thermocline depth and SST is strong, ranging from $r > 0.9$ in the east to $r \approx 0.6$ at 170°W . Time lagged correlations between thermocline depth and subsurface temperature anomalies indicate vertical advection of temperature anomalies from the thermocline to the surface in the eastern Pacific.

The measurements are compared with the results of forced OGCM and linear model experiments. Using model results, it is shown that the delay between thermocline depth and SST is caused mainly by upwelling and mixing between 140°W and 90°W . Between 170°E and 140°W the delay has a different explanation: thermocline depth anomalies travel to the eastern Pacific, where upwelling creates SST anomalies which in turn cause anomalous wind in the central Pacific. SST is then influenced by these wind anomalies.

¹This chapter is based on the paper “On the relationship between sea surface temperature and thermocline depth in the eastern equatorial Pacific” by H. Zelle, G. Appeldoorn, G. Burgers and G. J. van Oldenborgh, published in *J. Phys. Oceanogr.* 2004, **34**, 643–655

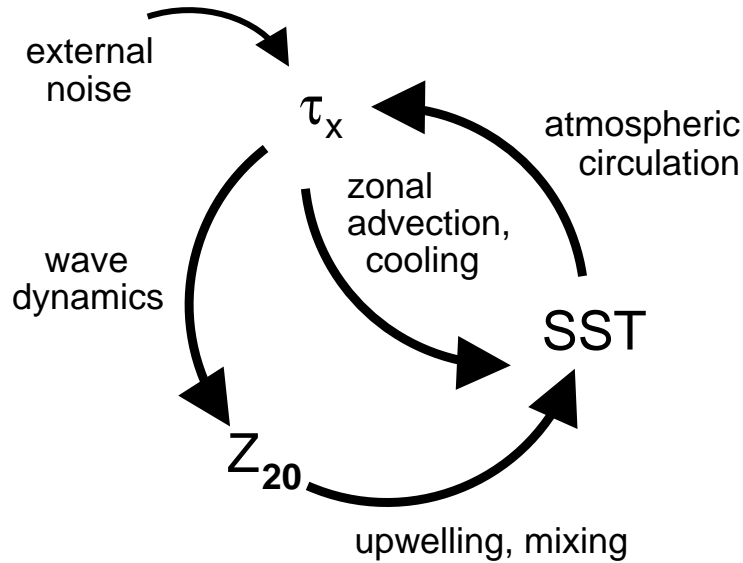


Figure 2.1: The main feedbacks in the ENSO cycle. Z_{20} denotes the thermocline depth and τ_x the zonal wind stress.

2.1 Introduction

The interactions that drive El Niño – Southern Oscillation (ENSO) are sketched in Figure 2.1. Sea surface temperature is chosen as a starting point along the cycle: large sea surface temperature variations, mostly in the eastern equatorial Pacific, change the strength of the trade winds, mainly in the center of the Pacific. The change in wind stress influences the local sea surface temperature directly by means of anomalous zonal advection, Ekman pumping (upwelling of cold water), evaporative cooling and mixing. Also, it produces planetary (Kelvin) waves, which influence the depth of the thermocline. The change in thermocline depth leads to a change in sea surface temperature in the east by upwelling and mixing, completing the cycle. Negative feedback is provided by Rossby waves generated in the east, traveling to the western coast where they reflect as downwelling Kelvin waves, reversing the process. Suarez and Schopf (1988) and Battisti and Hirst (1989) describe this feedback loop as a delayed oscillator. A discussion of important mechanisms for El Niño variability is given in the review of Dijkstra and Burgers (2002).

In the ENSO cycle as described above, sea surface temperature (SST) and thermocline depth play important roles. SST anomalies are the manifestation of an El Niño event, while thermocline depth anomalies mark the onset and ending of an El Niño event.

According to previous studies, the two most important mechanisms influencing

2.1. Introduction

SST in the equatorial Pacific are zonal advection of mean temperature by anomalous zonal currents (often called zonal advective feedback), and mean vertical advection of subsurface temperature anomalies (often called thermocline feedback). The importance of thermocline feedback is stressed in the concepts of the delayed oscillator (Battisti and Hirst, 1989; Suarez and Schopf, 1988) and the recharge oscillator model (Jin, 1997). Anomalous zonal advection and vertical advection are two of the most important terms in the SST equation of the Zebiak Cane model (Zebiak and Cane, 1987). Kleeman (1993) finds that thermocline depth changes have the strongest influence on SST in a coupled model, while zonal advection has a smaller influence. Picaut et al. (1996) stress the influence of zonal advection on SST in the equatorial Pacific in their analysis of TOGA/TAO measurements.

Jin and An (1999) confirm, in a study using NCEP reanalysis data and a simple recharge oscillator model, that anomalous zonal advection and mean vertical advection are the essential mechanisms that influence SST. They find that the influence of mean vertical advection is restricted to the eastern Pacific, while zonal advection influences mostly the central Pacific but also the eastern Pacific.

Kang et al. (2001) use a budget study of NCEP reanalysis data to investigate the relative importance of the various terms in the SST budget. They derive a simplified SST equation for ENSO, in which mean upwelling ($\overline{wT'_z}$) and anomalous zonal advection ($u'T'_x$) are the main contributing terms. Upwelling is dominant between 140°W and 90°W on the equator, and is found to be most important during the mature phase of El Niño, while during the developing phase zonal advection and upwelling are equally important. Wang and McPhaden (2000, 2001) perform a similar study of mechanisms influencing SST in the equatorial Pacific, based on TAO/TRITON observations at 4 locations along the equator, for the 1997–98 El Niño. They also find that zonal advection is important in the central Pacific, and that vertical advection is important in the eastern Pacific. The influence of zonal advection was mostly restricted to the onset of El Niño while vertical entrainment and diffusion were the most important processes during the termination phase. Vialard et al. (2001) have analyzed an OGCM forced by TAO/TRITON and ERS1/2 wind stress fields. They emphasize the importance of vertical advection and mixing in the eastern equatorial Pacific, and of zonal advection in the western and central equatorial Pacific. Mixing, a mechanism related to mean upwelling, is also emphasized as an important mechanism by Galanti and Tziperman (2002): subsurface temperature anomalies are transported vertically by mixing in the upper layer of the ocean.

Fedorov and Philander (2001) use a stability analysis of a coupled ocean-atmosphere model to show how two unstable modes (one corresponding to the delayed oscillator, and another associated with surface dynamics) with different behavior form the building blocks for ENSO. The second mode, associated with zonal advective feedback, is strongest in the central Pacific.

Other mechanisms play a role as well in the SST budget. Both anomalous advection of mean temperature and advection of anomalous temperature by mean current play a role in the zonal, meridional and vertical directions, and surface fluxes are important as well. The budget study of Kang et al. (2001) provides useful maps of the relative importance of these mechanisms in the NCEP reanalysis. They show that

mean zonal advection ($\overline{w'T'_x}$) is a small term, except in the western Pacific. Anomalous meridional advection ($v'T'_y$) is also found to be a small term. Mean meridional advection ($\overline{v'T'_y}$) can be a large term, especially during ENSO episodes when the eastern equatorial Pacific is very warm, and the meridional temperature gradient is high just off the equator. However, it effectively acts as a part of the Newtonian cooling term, only transporting excess heat away from the equator. Finally, they find that anomalous upwelling ($w'T'_z$) may be large at times in the eastern Pacific, but it is small on average compared to the mean upwelling term. Jin et al. (2003) show that the nonlinear upwelling term $w'T'_z$ is also important during strong events. Wang and McPhaden (2000, 2001) emphasize that there is not one dominating mechanism and that the relative importance of the mechanisms varies with the seasonal and ENSO cycle.

Harrison and Vecchi (2001) investigate the instantaneous correlation between thermocline depth and SST in the equatorial Pacific, using TAO/TRITON subsurface temperature data and NCEP gridded SST data. They only find a significant correlation in the eastern and east-central Pacific, and conclude that SST anomalies cannot be attributed to thermocline depth anomalies.

Building on their work, the subject of this study is the time structure of the local relation between thermocline depth and SST in the central and eastern equatorial Pacific. There is a strong, time-lagged relationship between the two variables. By which pathways are thermocline depth anomalies connected to SST anomalies? Which mechanisms are involved in these pathways? What time scales are associated with the different mechanisms? Can we derive from the relation between thermocline depth and SST what the relative importance of the mechanisms is, and where they are most important?

The starting point of our investigation is the lag correlation between observed thermocline depth anomalies and SST anomalies along the equator. This is shown in figure 2.2, using monthly subsurface temperature measurements from the TAO/TRITON array (McPhaden et al., 1998b) from the period 1990 – 1999. A monthly climatology was computed over this period and subtracted from the measurements to produce the anomalies. The depth of the 20°C isotherm is used as a proxy for the depth of the thermocline, it is denoted by Z_{20} . A similar but non-local correlation (between upper ocean heat content and Niño3 index) is shown by Latif et al. (2001) in a comparison study of coupled ocean-atmosphere models.

Figure 2.2 visualizes the time structure of the local relationship between SST and Z_{20} on the equator. The correlation between Z_{20} anomalies and SST anomalies is plotted as a function of longitude (horizontal axis) and lag (vertical axis). Contours show the strength of the correlation, while the thick line indicates the lag value where the correlation is maximal. Positive lag values mean that Z_{20} anomalies precede SST anomalies in time. There is a strong, direct relation ($r > 0.8$ at a lag of 2 weeks) between thermocline depth and SST in the eastern Pacific. In the central Pacific the relation is weaker ($r > 0.5$) and has a much larger lag (≈ 12 months). In the western Pacific the relation is reversed, with SST anomalies leading Z_{20} variations by about 4 months ($r \approx -0.4$).

Apart from the TAO/TRITON subsurface temperature measurements, we make use

2.1. Introduction

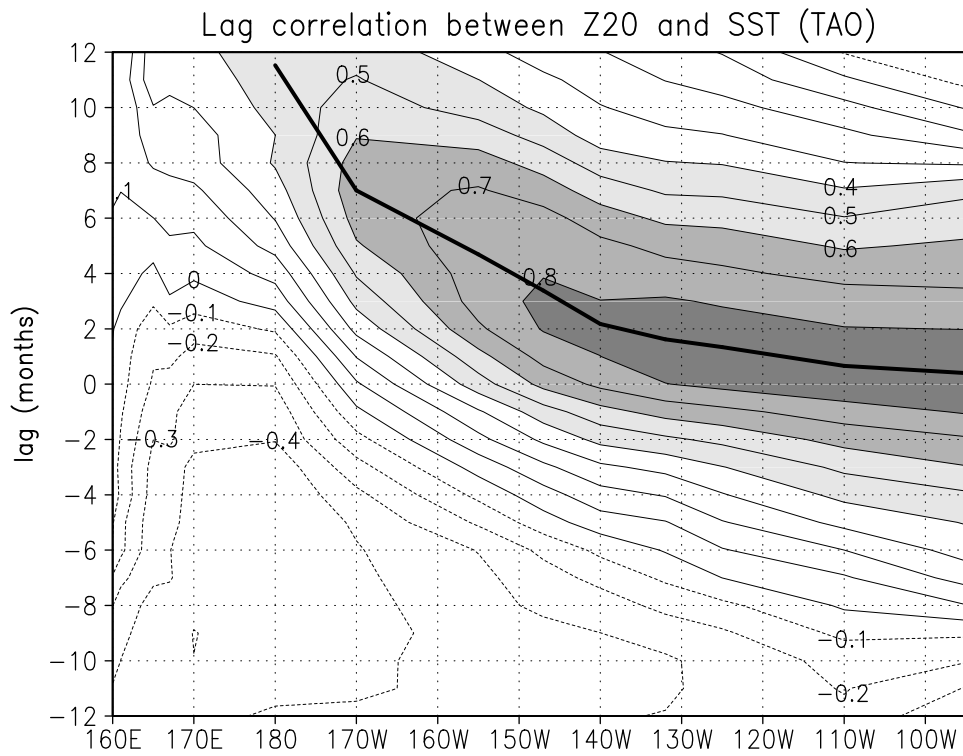


Figure 2.2: Lag correlation between observed Z_{20} anomalies and SST anomalies on the equator. A positive lag means Z_{20} is leading SST. The correlation was computed using monthly temperature data from the TAO/TRITON array for the period 1990 – 1999.

of the output of a forced OGCM simulation to obtain variables that are not available from measurements, such as vertical velocities. To assess the importance of different mechanisms, a linear shallow water model is used as well. It has a SST equation which can easily be modified, which makes it possible to test the importance of separate feedbacks by varying their strength without influencing other feedbacks.

The chapter is organized as follows: in section 2.2, the observational data are described. The models and their outputs are described in section 2.3. In section 2.4 the observational data are analyzed, and it is explained how the models were used to analyze the mechanisms found in the measurements. Section 2.5 presents two pathways by which Z_{20} anomalies are linked to SST anomalies in the equatorial Pacific, and discusses them in detail. A discussion of the analysis is presented in section 2.6 and the conclusions are listed in section 2.7.

2.2 Observations

For an investigation of the relation between Z_{20} and SST with observational data, measurements of Z_{20} and SST spanning several ENSO cycles are required. These measurements are available from the TAO (Tropical Atmosphere Ocean) / TRITON (TRIangle Trans-Ocean buoy Network) array, for the period 1990 – now (McPhaden et al., 1998b).

The array consists of a set of buoys in the Pacific ocean positioned at regular intervals on and around the equator. The buoys are positioned with a latitudinal spacing of 2° ($8^\circ\text{S} - 8^\circ\text{N}$) and a longitudinal spacing of approximately 15° . Temperature measurements are performed at depths up to 500 m, at intervals of about 25 m from the surface to the thermocline. Both wind and air temperature measurements are performed at the surface.

We have converted the daily temperature observations to monthly means, filling gaps by linear interpolation where the time interval was shorter than 10 days. For wind measurements, the average of at least 10 daily measurements was used. These means were interpolated linearly in space to a regular grid. No interpolation was attempted if the vertical distance to a measurement was more than 10 m or 25% of the distance between measurements, the meridional distance was more than 1° , or the zonal distance was more than 10° . Also, values were not interpolated if the temperature difference was larger than 1 K. The depth of the 20°C isotherm (Z_{20}) was found by linear interpolation in the resulting dataset.

2.3 Model Runs

Two models are used to complement the analysis of observational data. The first is an OGCM, used to provide quantities that are not directly measured, such as the upwelling velocity. The second model is a simple linear shallow-water model, used to analyze mechanisms involved in the problem.

2.3. Model Runs

2.3.1 HOPE

HOPE (Hamburg Ocean Primitive Equation Model) is a general circulation ocean model. At the ECMWF it is used for seasonal forecasts. The ocean model provides detailed fields of u , v , w , S and T , which are reasonably realistic (Stockdale et al., 1998; van Oldenborgh et al., 1999). The vertical velocity is especially important, since no adequate measurements of this quantity are available.

Details of the model physics and the applied numerical scheme are described in Wolff et al. (1997). The horizontal resolution of the model varies from $2.8^\circ\text{lon} \times 0.5^\circ\text{lat}$ at the equator, to $2.8^\circ\text{lon} \times 2.8^\circ\text{lat}$ at mid-latitudes.

The upper 300 meters of the ocean contain 10 depth levels, the deep ocean contains another 10. The model uses a shear enhanced mixing scheme similar to Pacanowski and Philander (1981). In addition, a mixed layer is simulated by increasing the mixing to $D = 2 \cdot 10^{-3}\text{m}^2\text{s}^{-1}$ when $\text{SST} - T_{\text{sub}} < 0.5\text{K}$.

A 10 year hind-cast run (1990 – 1999) was performed, using daily ECMWF analysis fields of wind stress, heat flux and fresh water flux as external forcing. The time period 1990 – 1999 was chosen for availability of TAO/TRITON buoy measurements and model forcing fields. SST was relaxed to observations with a strength of $40\text{Wm}^{-2}\text{K}^{-1}$, weak enough to allow dynamical variability in the region of interest. However, east of 100°W , and to a lesser degree west of 170°E , HOPE simulates SST relatively poorly and relaxation has a significant effect. The simulation of Z_{20} is very good east of 160°W .

West of the dateline the quality of the Z_{20} simulation is somewhat reduced due to too strong diffusion, but it remains good.

2.3.2 Linear shallow-water model

The linear model used in this study is a 1.5 layer shallow-water anomaly model of a baroclinic mode on a beta-plane (Burgers et al., 2002), combined with a linear SST equation. The SST equation in the model has the following generic form

$$\frac{dT}{dt} = \alpha(x)Z_{20}(x, y) + c\beta(x)\tau_x(x, y) - \gamma(x)T(x, y) \quad (2.1)$$

with T the SST anomaly field, Z_{20} the thermocline depth anomaly field and τ_x the zonal wind stress forcing anomaly field. The equation consists of three terms. The first term is proportional to Z_{20} , representing mean upwelling of anomalous temperature. Kleeman (1993) uses a similar term in his model. The second term is proportional to τ_x which is a proxy for zonal advection caused by zonal wind stress and other local effects. Latif (1987) describes this simple relationship between SST and wind stress, and applies it in a conceptual model. The last term is a relaxation term proportional to T . The strength of the wind stress term can be changed with the constant factor c to determine the effect of a zonal wind stress coupling.

The model has a 2° zonal grid spacing and a 1° meridional grid spacing, in a meridional domain of $[30^\circ\text{S}, 30^\circ\text{N}]$. The model is forced with FSU wind stress fields (Stricherz et al., 1997). Two model runs are performed. In the first run there is no

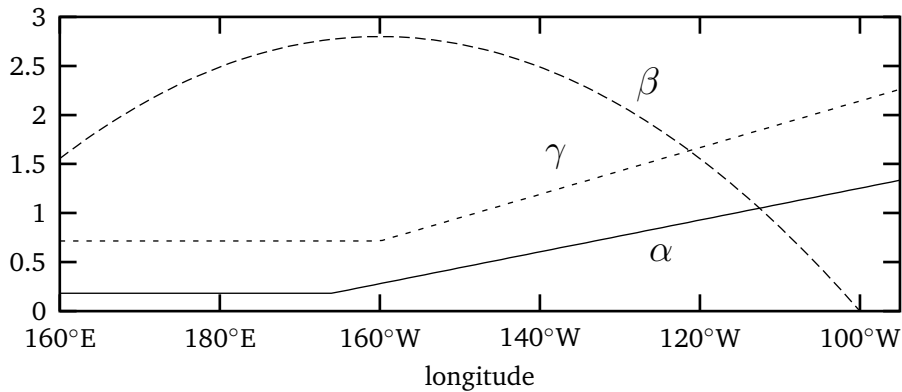


Figure 2.3: Linear model parameters that determine the strength of various terms in the SST equation (arbitrary units).

local coupling between τ_x and SST: $c = 0$. In the second run τ_x and SST are coupled ($c = 1$). The strength of the coupling $\beta(x)$ varies with location, depending on local climatological zonal wind stress and zonal temperature gradient conditions. Figure 2.3 shows the zonal dependence of the parameters α , β and γ , subjectively tuned to obtain the best Niño3 and Niño4 simulations in forced runs when $c = 1$. Both model runs reproduce Niño3 variability, with high correlations between model results and observations in the eastern equatorial Pacific (Burgers and van Oldenborgh, 2003).

2.4 Data analysis

2.4.1 Lag correlation between thermocline depth and SST, using TAO / TRITON data

Figure 2.2 shows that there is a strong relationship between Z_{20} anomalies and SST anomalies along the equator. Between 180°W and 90°W, the maximum correlation between Z_{20} and SST is in the range $0.5 < r < 0.9$. There is a gradually increasing time lag (maximum correlation line) between Z_{20} and SST anomalies, when moving from 90°E towards the dateline. Near the east coast the signal takes only 2 weeks to reach the surface, while near the dateline there is a lag of almost a year between Z_{20} and SST anomalies. As the time lag increases, correlation values decrease. West of the dateline the maximum correlation at positive lag is much lower ($r < 0.4$), indicating a different relationship between Z_{20} and SST in that region.

Further insight in the relationship between Z_{20} and SST is gained by plotting the correlation between Z_{20} anomalies and T_{sub} anomalies on the equator in a vertical cross section. Figure 2.4 shows such cross sections for the TAO/TRITON data, for increasing lag values (again, a positive lag means Z_{20} leads SST). At lag 0 the thermocline is clearly visible as a band of very high correlations, since thermocline depth anomalies are equivalent to local subsurface temperature anomalies. As time pro-

2.4. Data analysis

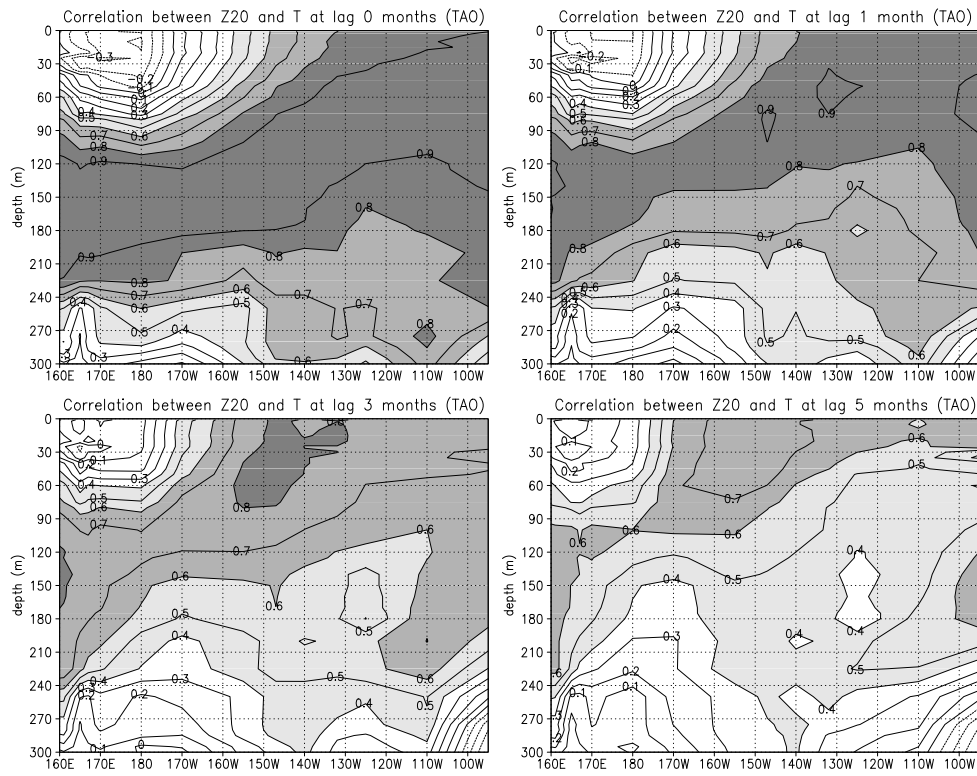


Figure 2.4: Correlation between Z_{20} anomalies and T_{sub} anomalies on the equator (TAO/TRITON), for increasing lag values. A positive lag means Z_{20} is leading T_{sub} .

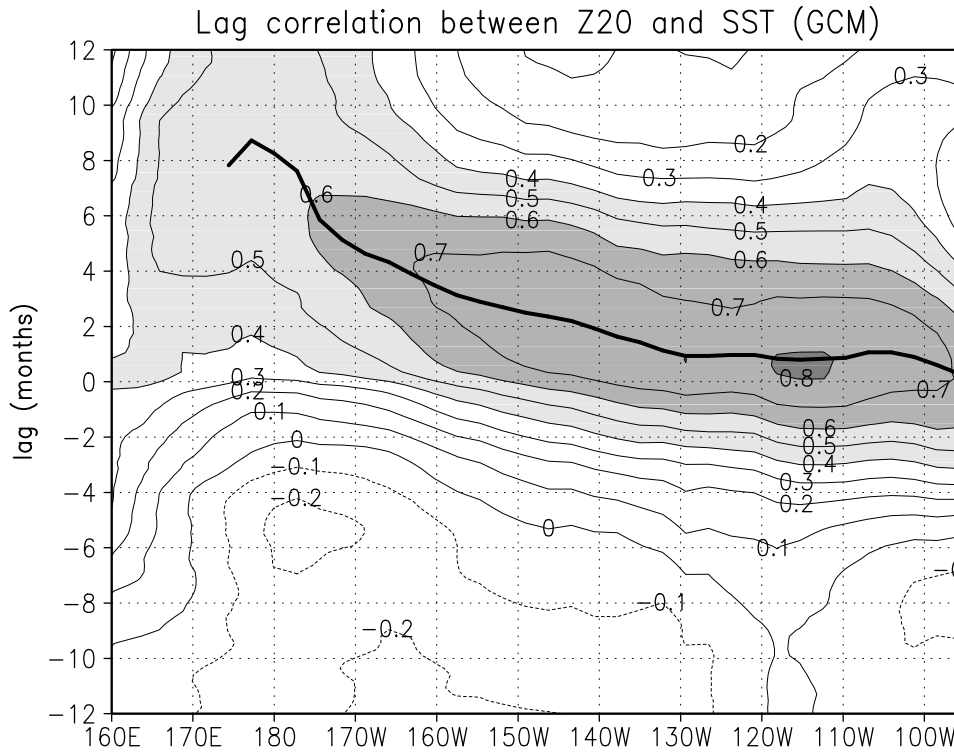


Figure 2.5: Lag correlation between Z_{20} anomalies and SST anomalies on the equator, for HOPE model output. A positive lag means Z_{20} is leading SST.

gresses the line of high correlations moves up towards the surface, representing a temperature anomaly traveling from the thermocline to the surface. Across the whole section correlation values are reduced in time, indicating the decay of the original thermocline depth signal. Note that at first strong signals ($r > 0.5$) only appear at the surface east of 160°W . After 4 months they also appear at 170°W , but never west of 180°W . West of the dateline there is little direct coupling between Z_{20} and SST: here Z_{20} anomalies and subsurface temperature anomalies are only coupled below 70 m – 100 m depth.

2.4.2 Lag correlation between thermocline depth and SST, using HOPE model output

The lag correlation between Z_{20} anomalies and SST anomalies in the HOPE model run is shown in figure 2.5. The model data compare reasonably well with the TAO/TRITON data, most features in the relation between Z_{20} and SST are present. The lag at which the correlation is maximal compares well in the eastern equato-

2.4. Data analysis

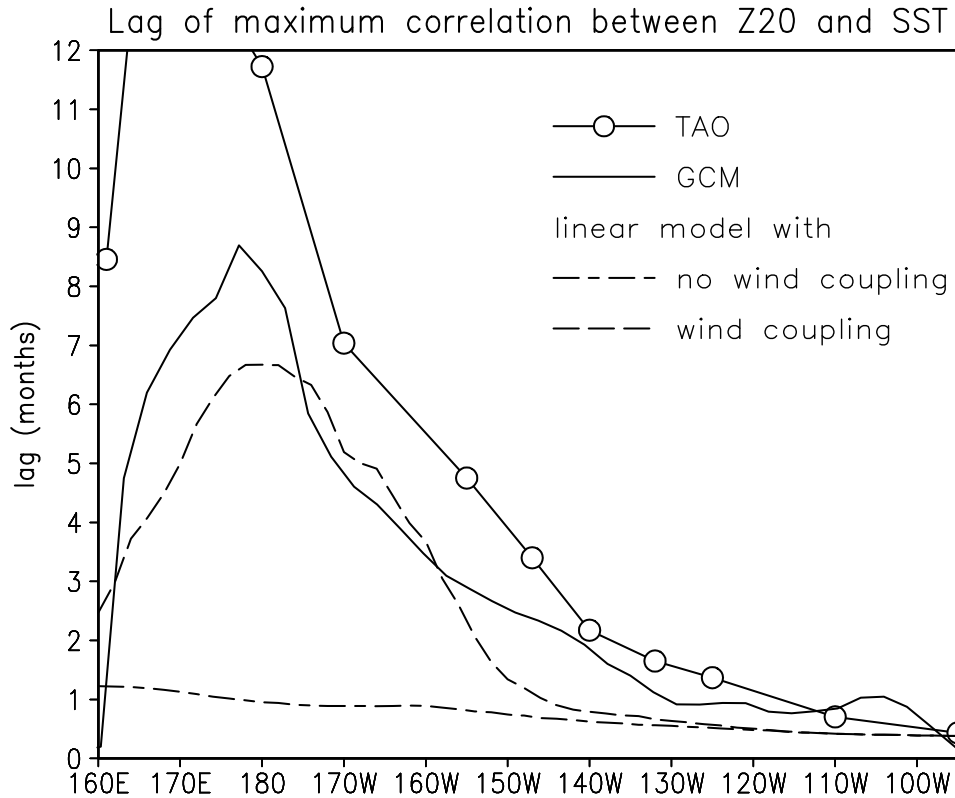


Figure 2.6: Lag at which the correlation between Z_{20} anomalies and SST anomalies is maximal. This represents the time a Z_{20} anomaly needs to manifest itself as a SST anomaly.

rial Pacific. Figure 2.6 shows these lags for TAO/TRITON data, HOPE model output, and the output of the linear shallow-water model described in section 2.3.2. East of 145°W the comparison between HOPE and TAO/TRITON is good. Further west HOPE starts to underestimate the lag, with a maximum error of 4 months at 170°E . The maximum correlation values are about equal, with correlations of around 0.8 between 150°W and 100°W .

Figure 2.7 shows the same cross sections on the equator as in figure 2.4, this time taken from HOPE model output. The comparison with figure 2.4 is reasonable. East of the dateline the correlations generally agree above the thermocline. West of the dateline, HOPE underestimates the strength of the relation between Z_{20} and T_{sub} around the depth of the thermocline and overestimates the strength in the surface layer. Similar to the observations, HOPE does show an area west of the dateline where the effects of Z_{20} anomalies do not penetrate to the surface, although the region is

Chapter 2. SST and thermocline depth

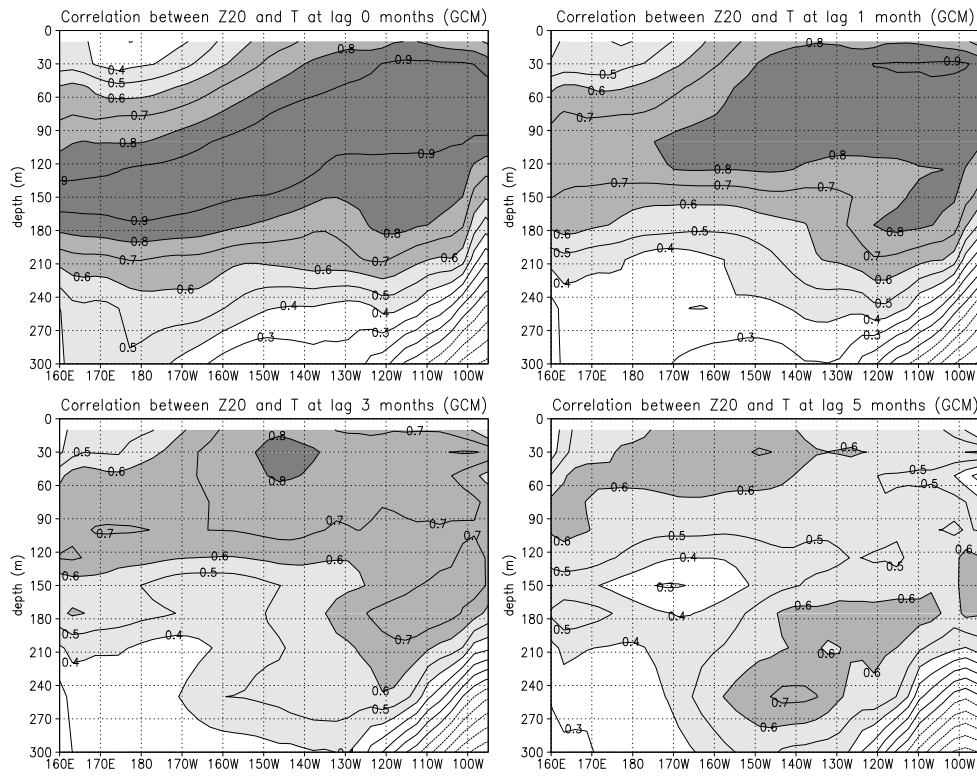


Figure 2.7: Correlation between Z_{20} anomalies and T_{sub} anomalies on the equator (HOPE), for increasing lag values. A positive lag means Z_{20} is leading T_{sub} .

2.4. Data analysis

shallower (0 – 50 m) and lies further west than in the observations.

The differences between HOPE and observations in the western Pacific are probably related to too strong mixing in HOPE around the thermocline in the western Pacific. Subsurface temperature profiles along the equator of the HOPE model run compare well with TAO/TRITON observations, but too strong mixing (and possibly upwelling) will cause a subsurface temperature response to thermocline anomalies too close to the surface. A comparison with Latif et al. (2001) shows that both in forced and coupled HOPE runs, the lag between Z_{20} anomalies and SST response in the western Pacific is underestimated.

Concluding, HOPE reproduces most features of the lag correlation between Z_{20} and SST in the central and eastern equatorial Pacific, and can be used for studying the mechanisms behind this relationship.

2.4.3 Lag correlation between thermocline depth and SST, using linear model output

First the linear model run without local wind feedback ($c = 0$) is analyzed. Figure 2.8 shows the lag correlation between Z_{20} anomalies and SST anomalies as in figure 2.2. It is immediately clear that, in this configuration, the relation between Z_{20} and SST is described incorrectly by the linear model. Figure 2.6 shows the lag where the correlation has a maximum, compared to TAO/TRITON and HOPE data. In the very east the lag is as observed, but it hardly increases towards the central Pacific.

The second linear model run, with local wind feedback ($c = 1$), performs much better. Figure 2.9 shows the lag correlation between Z_{20} anomalies and SST anomalies. The introduction of local τ_x -SST coupling clearly improves the situation in the east and central Pacific. Figure 2.6 shows that the simulation is still lacking in two respects: the increase in lag only appears west of 150°W instead of 120°W , and the maximum lag value at 180°W is 6 months, instead of 12 months as observed in the TAO/TRITON data. The overall picture has improved considerably, however. There is an approximately linear relation between the strength of the wind coupling and the lag, for values of c smaller than the default value $c = 1$. For higher values of c the lag increases more slowly. The model was tuned so that a value of $c = 1$ produces the best Niño3 and Niño4 simulations.

Figure 2.8 also sheds some light on the deficiencies of the HOPE model in the western Pacific. HOPE displays a lag between Z_{20} and SST anomalies that is too short, with too weak negative correlations at negative lags. The linear model without local wind coupling shows the same behavior, albeit more extreme. One could see it as the limiting case where vertical diffusion is infinitely strong: a thermocline depth anomaly translates directly into an SST tendency. Figures 2.8 and 2.5 suggest that in the western Pacific, the HOPE simulation lies between this limiting case and observations: diffusion is too strong or the local wind coupling is too weak. Figure 2.6 shows that the time lag around the dateline in HOPE is underestimated by around 3 months. This results in an ENSO cycle that is too short when HOPE is coupled to a statistical atmosphere, as described by van Oldenborgh et al. (1999). Latif et al. (2001) also find a too short oscillation period in a coupled version of the HOPE model.

Chapter 2. SST and thermocline depth

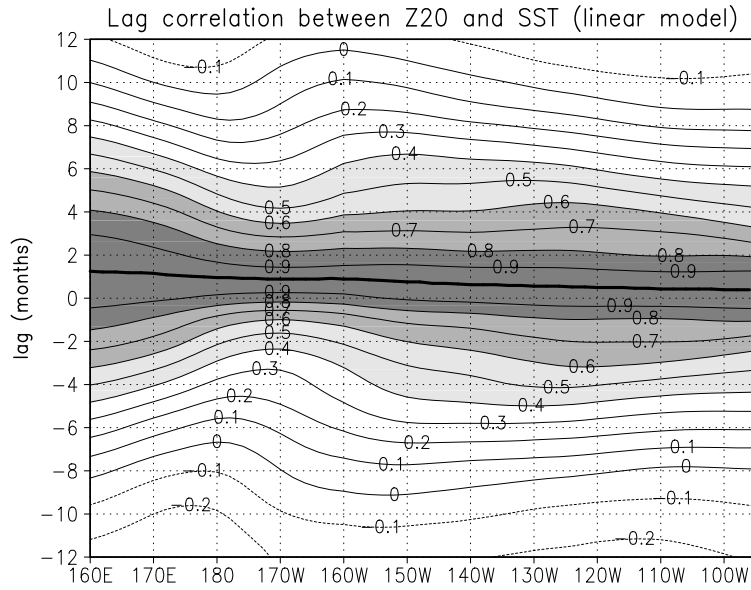


Figure 2.8: Lag correlation between Z₂₀ anomalies and SST anomalies on the equator, for linear model output without wind stress coupling ($c = 0$). A positive lag means Z₂₀ is leading SST.

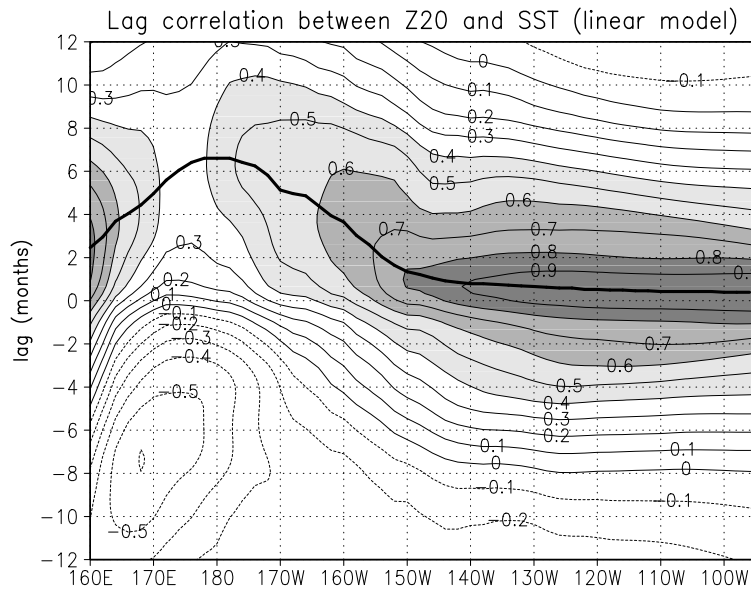


Figure 2.9: Lag correlation between Z₂₀ anomalies and SST anomalies on the equator, for a linear model run with direct coupling between τ_x and SST ($c = 1$). A positive lag means Z₂₀ is leading SST.

2.5 Two pathways

As discussed in the previous section, there is a clear relationship between Z_{20} and local SST in the TAO/TRITON data as well as the HOPE model run, especially east of 180°W . Following a Z_{20} anomaly, a SST anomaly appears at the surface with a time delay depending on latitude. We discuss two pathways by which Z_{20} anomalies may lead to SST anomalies:

1. A Z_{20} anomaly is equivalent to a subsurface temperature anomaly T_{sub} at the level of the thermocline, which is transported upward by upwelling until it reaches the surface. Mixing also contributes to the vertical transport of temperature anomalies. This will be called the *upwelling pathway*. The upwelling pathway includes any SST feedback that is directly related to thermocline depth anomalies. It is a *local* pathway.
2. A downwelling Z_{20} anomaly travels from the central equatorial Pacific to the eastern Pacific, where it causes a positive SST anomaly. This SST anomaly causes an eastward shift in the region of atmospheric convection above the equatorial Pacific, and produces a westerly wind anomaly in the central Pacific. The wind anomaly drives anomalous eastward zonal advection across the temperature gradient in the central Pacific, thereby causing a positive SST anomaly in the central Pacific. Also, the wind anomaly heats the surface waters directly through reduced evaporative cooling and reduced Ekman pumping, diminishing upwelling of colder subsurface waters.

This pathway relies on wind feedbacks: local effects of anomalous wind on SST. It will be called the *wind coupling pathway*. Contrary to the upwelling pathway, a remote coupling through wave dynamics and an atmospheric response is required. This pathway is *non local*: it makes an excursion to the eastern Pacific. Note that the upwelling pathway is included as a part of this pathway.

A passing Kelvin wave (Z_{20} anomaly) also induces anomalous zonal currents which, in the presence of a zonal temperature gradient, directly influence SST and T_{sub} . This effect is included in the correlation analysis, as it involves a local connection between Z_{20} and SST. It is similar to the upwelling pathway.

Figures 2.10 and 2.11 show schematic representations of these pathways. Their existence and importance will now be investigated in the two ocean models.

2.5.1 The upwelling pathway

Identifying the upwelling pathway is not easy, since measurements of upwelling velocities are not readily available. Johnson et al. (2001) give an analysis of upwelling velocities computed from observed horizontal velocities and divergence in the equatorial Pacific. In an OGCM like HOPE however, the vertical velocity field, w , is explicitly modeled. In section 2.4 it was established that the HOPE OGCM reproduces most features of the Z_{20} -SST relationship in the central and eastern equatorial Pacific.

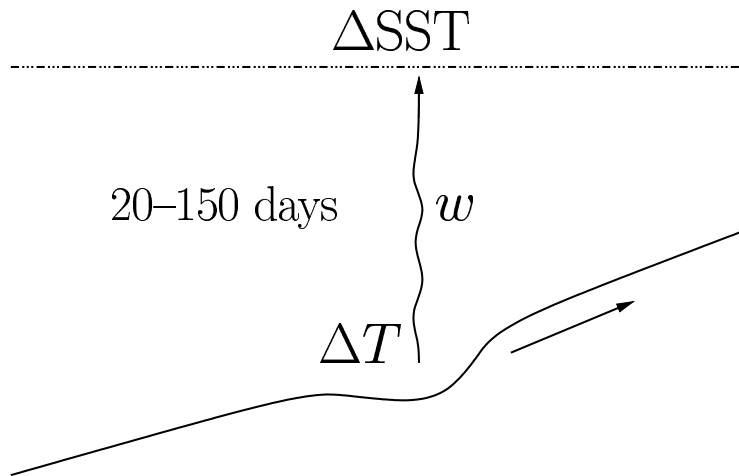


Figure 2.10: Sketch of the upwelling pathway.

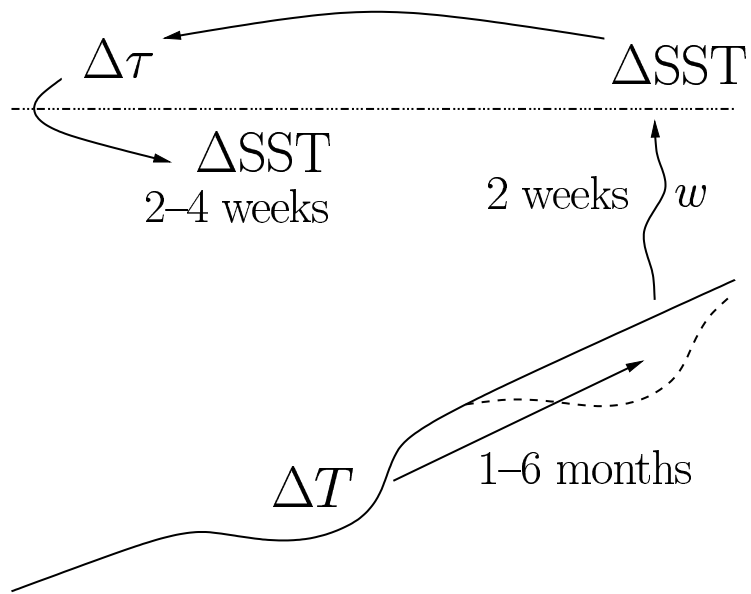


Figure 2.11: Sketch of the wind coupling pathway.

2.5. Two pathways

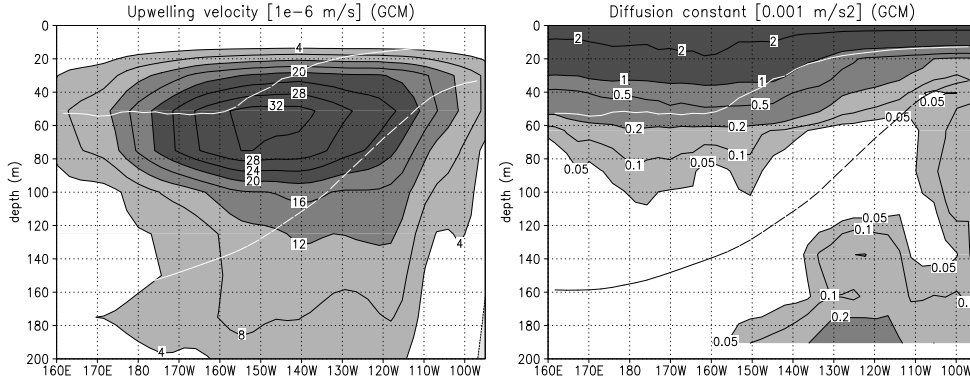


Figure 2.12: Vertical sections on the equator of vertical advection w (left) and diffusion coefficient D (right) in the HOPE model. Values were time averaged over the 10 year period. Both figures show the average mixed layer depth (upper line) and thermocline depth (lower line) in HOPE.

The time scales of upwelling and mixing will be discussed, and an assessment of the importance of the upwelling pathway in HOPE (including mixing) for the relation between Z_{20} and SST is made.

The relevant time scales of upwelling and mixing in the relation between SST and Z_{20} depend on the depth of the mixed layer and the thermocline, respectively. For a given temperature profile $T(z)$, a proxy of the mixed layer depth Z_{mix} was determined by

$$\text{SST} - T(Z_{\text{mix}}) = 0.5 \text{ K}$$

The average depth of the mixed layer proxy (from HOPE model output) is shown in figure 2.12, and varies approximately from 50 m at 180°W to 10 m at 120°W . Figure 2.12 also shows the average thermocline depth approximated by Z_{20} , which is about three times as deep as the mixed layer. Vertical sections on the equator are shown of the upwelling velocity and diffusion coefficient in the HOPE model output, averaged over the 10 year period. Using the model results, mixing and upwelling have been compared. Generally, in the HOPE model, mixing is a fast process compared to upwelling in the upper mixed layer of the ocean and a slow process below the mixed layer. In the mixed layer, diffusion is the strongest process. In about 14 days, the typical penetration distance for diffusion (\sqrt{Dt} , $D \approx 2 \cdot 10^{-3} \text{ m}^2 \text{ s}^{-1}$) is of the order of the mixed layer depth. Upwelling velocities reach maxima of about 2 m dy^{-1} ($w \approx 2 \cdot 10^{-5} \text{ m s}^{-1}$) at the bottom of the mixed layer. Between the mixed layer and the thermocline, upwelling is the strongest process. Here, the penetration distance for diffusion is much smaller, of the order of 10 m in 14 days ($D \approx 10^{-4} \text{ m}^2 \text{ s}^{-1}$).

To investigate the time scale of the upwelling pathway in HOPE, an estimate for the time lag between Z_{20} and SST anomalies calculated from upwelling velocities will be compared to the actual time lag found in the model run. First we consider the upwelling field w in HOPE. Figure 2.13 shows the mean upwelling velocity \bar{w} and the

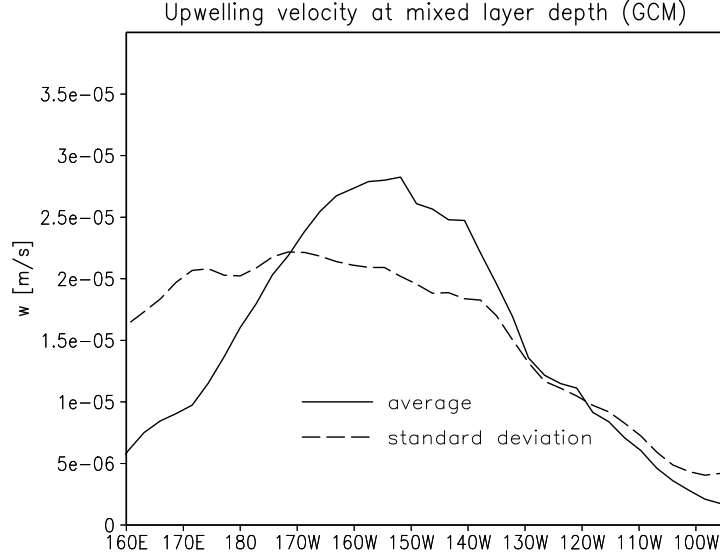


Figure 2.13: Mean upwelling velocity \bar{w} (m s^{-1}) in the HOPE model run, at the bottom of the mixed layer along the equator.

standard deviation of w , at the bottom of the mixed layer on the equator. Figure 2.13 shows a steady increase in \bar{w} from 160°E to 160°W . Between 160°W and 140°W \bar{w} reaches a maximum value of $3 \cdot 10^{-5} \text{ m s}^{-1}$ ($\approx 2.6 \text{ m dy}^{-1}$). This value is of the same order of magnitude as the $(1.9 \pm 0.9) \cdot 10^{-5} \text{ m s}^{-1}$ reported by Johnson et al. (2001). Further east \bar{w} decreases strongly along the equator, to a minimum at 100°W . (The upwelling zone is located further south and continues along the South American coast.) The variability of w is large: the standard deviation of w has the same order of magnitude as the mean \bar{w} across the equatorial Pacific.

One would expect that if upwelling were the only term involved in the relationship between Z_{20} and SST, the lag would be directly related to the upwelling velocity and thermocline depth. Higher upwelling velocities would give rise to shorter lags, while a deeper thermocline would imply longer lags. Figure 2.2 indeed shows an increasing time lag when moving west from 90°W . To see if this increasing lag corresponds to the local upwelling velocities and increasing thermocline depth, the expected lag is computed from the model output as:

$$\Delta t_w = \int_{Z_{20}}^0 \frac{1}{\bar{w}(z) + w_d(z)} dz \quad (2.2)$$

An effective vertical velocity component representing diffusion, w_d , is crudely estimated as follows: the penetration depth by diffusion is $z = \sqrt{Dt}$, we take the time derivative to estimate a 'velocity' w_d . Substituting $w_d = z/t$ leads to the approximation $w_d(z) = D/2z$. This correction to w is only important in the mixed layer.

2.5. Two pathways

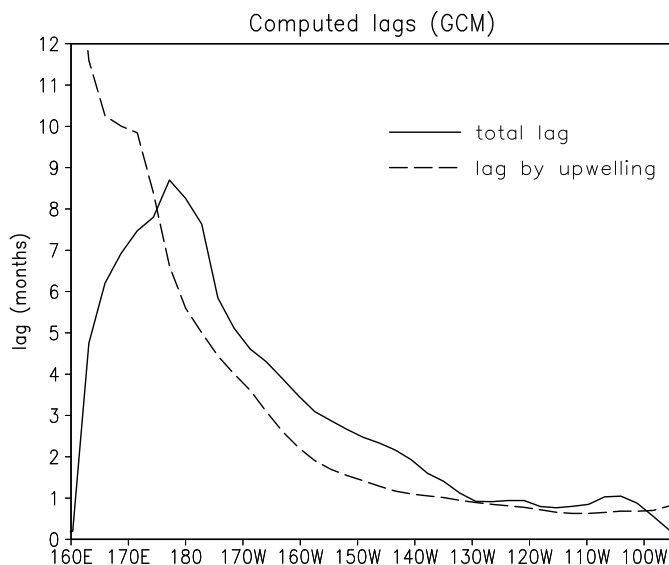


Figure 2.14: Time lag between Z_{20} signal and SST response. Comparison of observed lag with computed lag for upwelling, both using HOPE model output.

The integral in equation 2.2 is dominated by the mean upwelling term. The next step is to compare this “lag caused by upwelling” with the actual lag found in the model output (figure 2.6). The lags are plotted in Figure 2.14. They compare well in the east ($140^{\circ}\text{W} - 90^{\circ}\text{W}$, lag up to 2 months), while further westward ($180^{\circ}\text{W} - 140^{\circ}\text{W}$) the modeled lag is larger (by up to three months) than the computed lag for upwelling. West of the dateline, the longitudinal dependence of the modeled and the computed lag is quite different.

The effect of anomalous upwelling has been left out of the analysis presented here. In the introduction it was noted that this term is small on average but may be large at times. The effect on the mean time lag Δt_w as presented in figure 2.14 is small (not shown). In certain cases the lag may increase due to reduced upwelling, like at the end of the '97/98 El Niño, when zonal wind was reduced as far east as 100°W (McPhaden, 1999). During La Niña the lag will be smaller.

The conclusion is that in the HOPE model, mean upwelling of anomalous temperature is probably the most important pathway in the range 140°W to 90°W : it explains the observed lag of 2 weeks to one month between Z_{20} and SST. Further west, another pathway than upwelling is playing a role. The wind coupling pathway is the most likely cause: section 2.5.2 describes how wind coupling becomes more important in this region. Upwelling still contributes, but it is no longer the dominant pathway: it cannot explain the observed lag. The wind coupling pathway must be slower than the upwelling pathway: time lags increase rapidly where the wind coupling becomes more important.

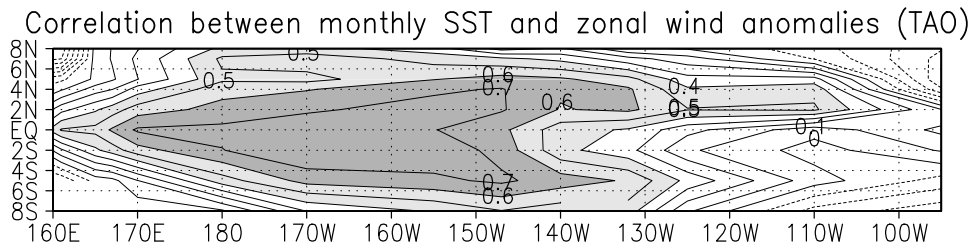


Figure 2.15: Correlation between zonal wind anomalies and SST anomalies, as computed from observed TAO/TRITON data (1990 – 1999).

2.5.2 The wind coupling pathway

We will try to verify the existence and importance of the wind coupling pathway using the TAO/TRITON data and with the aid of a simple linear model.

A simple way to illustrate that zonal wind has a strong influence on local SST in the equatorial Pacific is to plot the correlation between the two, using TAO/TRITON measurements. Figure 2.15 shows that zonal wind has a strong coupling with SST in the range $170^{\circ}\text{E} - 140^{\circ}\text{W}$. The correlation between Niño3 and zonal wind in the central equatorial Pacific is also high (not shown). The causal relationships behind these correlations are as follows: in the western Pacific SST is directly influenced by local zonal wind anomalies, while SST anomalies in the eastern Pacific are the cause of these wind anomalies. This corresponds with the previous section where it was expected that west of 140°W a pathway other than upwelling becomes important. On the equator, the correlation between meridional wind and SST is very weak (not shown).

To see if a zonal wind coupling can indeed introduce lags of 9 to 12 months in the central equatorial Pacific, the two linear model runs without and with direct wind-SST coupling (figures 2.8 and 2.9) are compared. The introduction of the wind coupling pathway increases the lag around the dateline from about 1 month to 6–8 months (the maximum correlation in figure 2.9 occurs at a lag of 6 months, but at a lag of 8 months correlation values are almost identical). Although the lag in the central Pacific is shorter than observed, the linear model now has a lag structure similar to that of HOPE, even in the western Pacific, contrary to the computed lag for the upwelling pathway in figure 2.14. East of 140°W the lag structure does not improve, because the upwelling pathway is dominant there. This shows that a coupling between zonal wind and SST can indeed produce lag correlation patterns similar to the observations in the central equatorial Pacific.

The total response time for the upwelling pathway (figure 2.10) varies from 14 days in the very east to 150 days at the dateline. Based on the speed of a free Kelvin wave, which is $\approx 2.5\text{m s}^{-1}$, the total time for the wind coupling pathway (figure 2.11) would vary between 65 days (140°W) and 85 days (180°W). This may appear to

2.6. Discussion

be an inconsistency: an 85 day lag cannot explain the observed lag of 250 days at the dateline (see figure 2.6). It was just shown, however, that direct wind coupling *can* produce such lags (of ≈ 8 months) in a simple model. How can this apparent inconsistency be explained?

When a free Kelvin wave departs from the central Pacific, it will indeed arrive at the east coast in 1 – 2 months, where it will produce SST anomalies within 2 weeks. However, generally Z_{20} anomalies are not part of a free Kelvin wave, as discussed e.g. in the review of Neelin et al. (1998).

Consider the shallow water equation for zonal advection (e.g., Gill, 1982):

$$\frac{\partial u}{\partial t} - fv + g' \frac{\partial \eta}{\partial x} = \tau_x \quad (2.3)$$

On the equator ($f = 0$), τ_x is balanced by $\partial u/\partial t + g'\partial\eta/\partial x$. In a linear model, zonal current changes only when there is an imbalance between zonal wind stress and the slope of the thermocline. As discussed by Neelin et al. (1998), Z_{20} anomalies will propagate as a forced Kelvin wave: in an approximate balance between thermocline depth slope and zonal wind stress. The coupled system travels eastward at a much slower rate than the free Kelvin wave speed.

This explains how the lag associated with the wind coupling pathway can be as long as 250 days (figure 2.6). A second explanation for the large observed lag in the linear model could be westward propagation of SST anomalies accompanied by a westward shift of zonal wind anomalies, as described by Neelin (1991). However, although episodes of westward SST propagation occur, diagrams of the lagged correlation between local SST and SST at 120°W show no systematic westward propagation of SST anomalies.

One might argue that the models used in this study do not simulate the full wind coupling pathway as described in section 2.5. Because the models are forced by observed surface winds, there is no simulated atmospheric response to SST anomalies in the eastern Pacific, breaking the connection between Z_{20} anomalies and SST anomalies in the central Pacific. A coupled version of the linear model (Burgers and van Oldenborgh, 2003) shows the same behavior however, indicating that the observed lag between Z_{20} and SST anomalies in the central Pacific is indeed caused by the interaction between Kelvin waves, SST anomalies in the eastern Pacific and the wind response to those anomalies.

2.6 Discussion

A comparison with previous studies shows that our results generally agree with earlier work. The strong simultaneous correlation between Z_{20} and SST that Harrison and Vecchi (2001) find in the eastern Pacific is confirmed. However, in the central Pacific *lagged* correlations are much stronger than non-lagged correlations. The present study shows that SST anomalies as far west as 140°W can be partially attributed to local Z_{20} anomalies, a result which does not follow from the analysis of Harrison and Vecchi (2001).

In section 2.5.1 it was shown that the upwelling pathway is dominant in the range $140^{\circ}\text{W} - 90^{\circ}\text{W}$, while in section 2.5.2 it was shown that west of 140°W the wind coupling pathway is most important. Using the two main influences on SST, the thermocline feedback and the wind feedback, we have constructed these pathways by which local SST can be related to local Z_{20} . The two pathways are sufficient to explain the structure of the lag correlation between SST and Z_{20} anomalies. The areas of influence of the feedbacks needed to obtain this result are consistent with the results of Kang et al. (2001); Vialard et al. (2001) and others mentioned in the introduction, who agree that mean upwelling is the most important contribution to SST in the eastern equatorial Pacific, while further west anomalous zonal advection (caused by wind) is the most important.

Upwelling and zonal advection are not the only mechanisms that play a role in the two feedbacks. Mixing in the upper ocean layer of the eastern Pacific, found to be important by Galanti and Tziperman (2002); Vialard et al. (2001), is included in the thermocline feedback. Wang and McPhaden (2001) find that both zonal advection and vertical heat flux (anomalous upwelling) are important in the central Pacific, these mechanisms are included in the wind coupling feedback together with other local effects of wind on SST. Our results provide no information on seasonal dependence and ENSO phase dependence such as the work of Wang and McPhaden (2001), it does however use observational data from a 10 year time period showing that the pathways are valid in general and not just for the 1997/1998 El Niño.

The thermocline feedback and wind coupling feedback discussed above are closely related to the SST and delayed oscillator modes described by Neelin (1991) and Fedorov and Philander (2001). Our work emphasizes the distinction between SST tendencies directly related to thermocline depth, and those related to the local influence of wind on SST. The distinction between the two feedbacks provides a natural spatial separation between the central and eastern equatorial Pacific. This is different from the usual distinction between zonal advection and upwelling through the base of the mixed layer, which are both important across the central and eastern Pacific (Jin and An, 1999; Wang and McPhaden, 2000, 2001). Burgers and van Oldenborgh (2003) make a similar distinction as in this chapter, showing the importance of local wind feedback in the central Pacific for a realistic simulation of the ENSO cycle in a linear coupled model.

Figure 2.8 emphasizes that models that lack mechanisms which are vital to the ENSO cycle, such as those in the wind coupling feedback, will fail to reproduce the time structure of the relation between Z_{20} and SST. Comparing the lag correlation between Z_{20} and SST with actual measurements is a good test of the ENSO dynamics in a model, as it is sensitive to the balance between the two most important mechanisms that influence SST. The test has also been applied to the model of Zebiak and Cane (1987). In this model, both the strength and the time structure of the Z_{20} -SST correlation do not compare very well with observations, with too low correlations in the central Pacific, and no noticeable time lag between Z_{20} and SST. Latif et al. (2001) use a similar test, the correlation between upper ocean heat content and the Niño3 index, to compare a large number of coupled ocean-atmosphere models.

The main difference between our test and the test of Latif et al. (2001) is that

2.7. Conclusions

because our test uses local SST, it is sensitive to the strength of the local wind feedback. This allows it to distinguish between linear model runs with and without wind feedback.

2.7 Conclusions

This study investigates the relationship between thermocline depth (Z_{20}) and SST in the equatorial Pacific.

TAO/TRITON Z_{20} and SST measurements are strongly correlated ($r > 0.8$ in the far east, $r > 0.5$ as far west as the dateline) at time lags between 2 weeks (90°W) and 12 months (180°E). Two important pathways are distinguished that cause the relation between Z_{20} and SST: the ‘upwelling pathway’ (figure 2.10) and the ‘wind coupling pathway’ (figure 2.11).

The upwelling pathway consists of vertical advection of temperature anomalies from the thermocline to the surface. These temperature anomalies are caused by thermocline depth anomalies, and are transported to the surface by a combination of upwelling and vertical mixing. At the surface they appear as SST anomalies. The wind coupling pathway starts with a thermocline depth anomaly in the central Pacific which travels east as a set of Kelvin waves, causing SST anomalies in the eastern Pacific. These SST anomalies induce zonal wind anomalies in the central Pacific. The anomalous zonal winds cause SST anomalies through anomalous upwelling and evaporation and through anomalous zonal advection across the edge of the warm pool.

Using the output of the HOPE OGCM and a simple linear model, the relative importance of these pathways was investigated. A comparison of the lag observed in the HOPE model with a lag value computed from the upwelling velocity and thermocline depth, shows that the upwelling pathway is most important in the region $140^\circ\text{W} - 90^\circ\text{W}$. In this region, the lag between Z_{20} and SST ranges from 2 weeks to 2 months. Mean upwelling exists as far west as the dateline in HOPE, but its influence is much smaller there, due to a deeper thermocline. A test with the linear model where a local coupling between zonal wind stress and SST was introduced, shows that the zonal wind coupling pathway is most important in the region $170^\circ\text{E} - 140^\circ\text{W}$. In this region, the lag between Z_{20} and SST ranges from 2 – 12 months. East of 140°W , there is no direct coupling between zonal wind and local SST. This is because the zonal wind shows little response to anomalous SST in the eastern Pacific. Another factor is the weaker zonal temperature gradient in the surface water. Considering the continuity of the increasing lag between Z_{20} and SST when moving westward from the east coast, it is most likely that west of 140°W the two pathways overlap, and zonal wind coupling slowly takes over from upwelling in importance.

The lagged relationship between Z_{20} and SST, as found in TAO/TRITON measurements, is shown to be modeled reasonably well by the HOPE OGCM. The linear model used in this study showed a much improved relationship after introduction of a direct coupling between zonal wind stress τ_x and SST. Both thermocline coupling and wind coupling are required for the linear model to properly simulate SST across the

Chapter 2. SST and thermocline depth

equatorial Pacific. A comparison of the time structure of the Z_{20} -SST relationship between ocean models and observations is shown to be a good test for ENSO models (both forced and coupled), that is sensitive to the strength of the mechanisms that influence SST. The use of such a test may contribute to the improvement of model El Niño simulations.

Chapter 3

Evolution of SST anomalies in the warm pool

The growth and evolution of interannual SST anomalies in the western and central equatorial Pacific are studied using observational data and a model simulation. At the onset of an El Niño event SST anomalies often develop in the far western Pacific, the warm pool region. At the peak of the event the region of positive SST anomalies is east of the dateline, during the decay phase the SST anomalies often withdraw to the west.

A budget study is performed with an ocean general circulation model simulation to analyze the mechanisms behind the growth and zonal movement of these SST anomalies. The model uses isopycnic coordinates, allowing for a closed mixed layer budget with a variable mixed layer depth.

We find that all factors controlling the initial development of SST anomalies in the western Pacific are related to changes in local wind speed or zonal wind stress. Anomalous latent heat flux, upwelling and zonal advection generate and reinforce the initial SST anomaly by increasing the net heat flux into the surface layer. Anomalous westerly winds reduce the local mixed layer depth; this affects the balance between mean horizontal and vertical fluxes and causes a vertical redistribution of heat, resulting in an increase of SST. This effect dominates the eastward propagation of SST anomalies. Westward movement of the SST anomaly after the peak of the event is caused by a combination of radiative cooling in the central Pacific caused by increased cloud cover and mean zonal advection pushing warm water back to the western Pacific.

¹This chapter is based on the paper “The evolution of SST anomalies in the warm pool during El Niño” by H. Zelle, G. J. van Oldenborgh, G. Burgers, S.-I. An and F.-F. Jin, as submitted to *J. Phys. Oceanogr.*, December 2004.

3.1 Introduction

There are two positive feedback loops that make El Niño — Southern Oscillation (ENSO) oscillations stronger and more persistent than SST perturbations in other regions (Neelin et al., 1998; Fedorov and Philander, 2001; Burgers and van Oldenborgh, 2003; Zelle et al., 2004). The first is the classical thermocline feedback loop first proposed by Bjerknes (1966): A zonal wind stress anomaly excites anomalies in the thermocline depth that travel eastwards and surface as SST anomalies. These in turn affect the wind in the central Pacific, reinforcing the original anomaly. Delayed negative feedback is exerted by the loss of warm water to off-equatorial regions, shallowing the thermocline along the whole equator and eventually ending the event (Jin, 1997). The second feedback loop is confined to the surface of equatorial Pacific around the edge of the warm pool: a zonal wind stress anomaly generates an SST anomaly by advection and changes in evaporation and upwelling; this SST anomaly in turn affects the mean zonal wind (e.g. Neelin, 1991; Picaut et al., 1996; Wang et al., 1999).

SST anomalies in the eastern Pacific are controlled mostly by the thermocline feedback (An et al., 1999; Kang et al., 2001). They are described well by either the first EOF of SST in the tropical Pacific or by the Niño3 index, which are highly correlated and describe SST variations in the climatological cold tongue. SST anomalies in the central Pacific are controlled by the wind stress surface feedback. This aspect of El Niño is described by the Niño4 index, which is correlated to the Niño3 index ($r \approx 0.75$), but also shows its own dynamics, especially in boreal spring and summer. Anomalies also persist longer in the central Pacific than in the east.

The balance between the two feedback loops differs from event to event. Figure 3.1 shows a Hovmöller diagram of SST in the equatorial Pacific, averaged from 2°S to 2°N , as measured by the TAO/TRITON array of moored buoys (McPhaden et al., 1998a) over the period 1990–1996. During the large 1997/98 El Niño the maximum SST anomalies (more than 5 K) occurred near the South-American coast, and were driven mainly by the thermocline feedback (McPhaden, 1999). In contrast, during the recent 2002/03 El Niño the largest anomalies (2.5 K) were in the central Pacific. This shows the relative importance of the surface feedback during this event. The 1991/92 and 1994/95 El Niños seem similarly dominated by the central Pacific surface feedback.

When the positive SST anomalies around the dateline are examined in more detail, it becomes apparent that they move zonally in time. This is especially visible shortly before and after the El Niño events. First, positive SST anomalies develop in the western Pacific. They move eastward across the dateline and form the start of the El Niño event. After the weaker events the reverse process occurs: when the strongest SST anomalies in the central Pacific have died out, the remaining positive anomalies around the dateline move back to the west. During this zonal movement the line where zonal wind is zero (figure 3.1, right pane) follows the maximum SST anomalies.

The surface feedback in the warm pool plays a relatively large role during the development and termination of El Niño events. A proper understanding may help in

3.2. Observations

predicting when El Niño events start and end. The location also makes the feedback important: the atmosphere is sensitive to changes in SST around the edge of the warm pool, because the 28°C isotherm represents a threshold for atmospheric convection. The importance of the movement of the edge of the warm pool in ENSO has been addressed by Fu et al. (1986), who indicate that areas of strong convection are linked to the eastern edge of the warm pool. Picaut et al. (1996, 1997) confirm this and find zonal advection to be the main factor for zonal movement of the 28°C isotherm. Wang and McPhaden (2000) show that surface heat fluxes also have a large influence on SST in the warm pool region. Wang et al. (1999) discuss how evaporation may not just act as a damping term but can also generate SST anomalies in a positive feedback between wind speed, latent heat flux and SST.

In this chapter we will investigate the processes that first enhance and later reduce SST anomalies in the warm pool, and explain the zonal movement of these SST anomalies. The balance between zonal advection, surface heat fluxes and the associated feedback loops will be discussed. These questions shall be addressed by computing the mixed layer heat budget in MICOM, an isopycnic coordinate ocean model, forced with reanalysis data. The model simulation is validated by comparing with observations and reanalysis data. The budget enables us to investigate the strength of individual terms in the SST equation. The effects of wind, mixed layer depth and surface fluxes on the budget will be discussed.

In section 3.2 the growth and decay of SST anomalies is examined using observational data. The model setup and computation of the surface layer temperature budget are described and verified with observational data in section 3.3. The results of the budget study are described and analyzed in section 3.4. A summary and conclusions are presented in section 3.6.

3.2 Observations

Fig. 3.1 shows a Hovmöller diagram of SST anomalies (left panel) and zonal wind anomalies (right panel) at the equator in the Pacific. The data shown are observations from the TAO/TRITON mooring array (McPhaden et al., 1998a) for the period 1990–2004. The onset of El Niño shows a similar pattern in the western Pacific for all events: SST anomalies develop in the far western Pacific around 150°E and move eastward until the peak of the event. The peak is qualitatively different for the larger events (e.g. 1982/83, 1997/98) and the weaker events (e.g. 1991/92, 1992/93, 1994/95 and 2002/03). The large events show SST anomalies of up to +5 K, while SST anomalies during the weaker events do not exceed +2.5 K. The maximum SST anomalies during weaker events are not located in the eastern Pacific, but in the central Pacific around 160°W. The end of weak El Niño events is characterized by a westward movement of SST anomalies to approximately 150°E. The warm pool dynamics are shown most clearly in these weaker events, which will therefore be used to illustrate the mechanisms behind the dynamics.

The goal of this chapter is to explain why SST anomalies in the western Pacific move zonally, and which mechanisms are responsible for their development. The

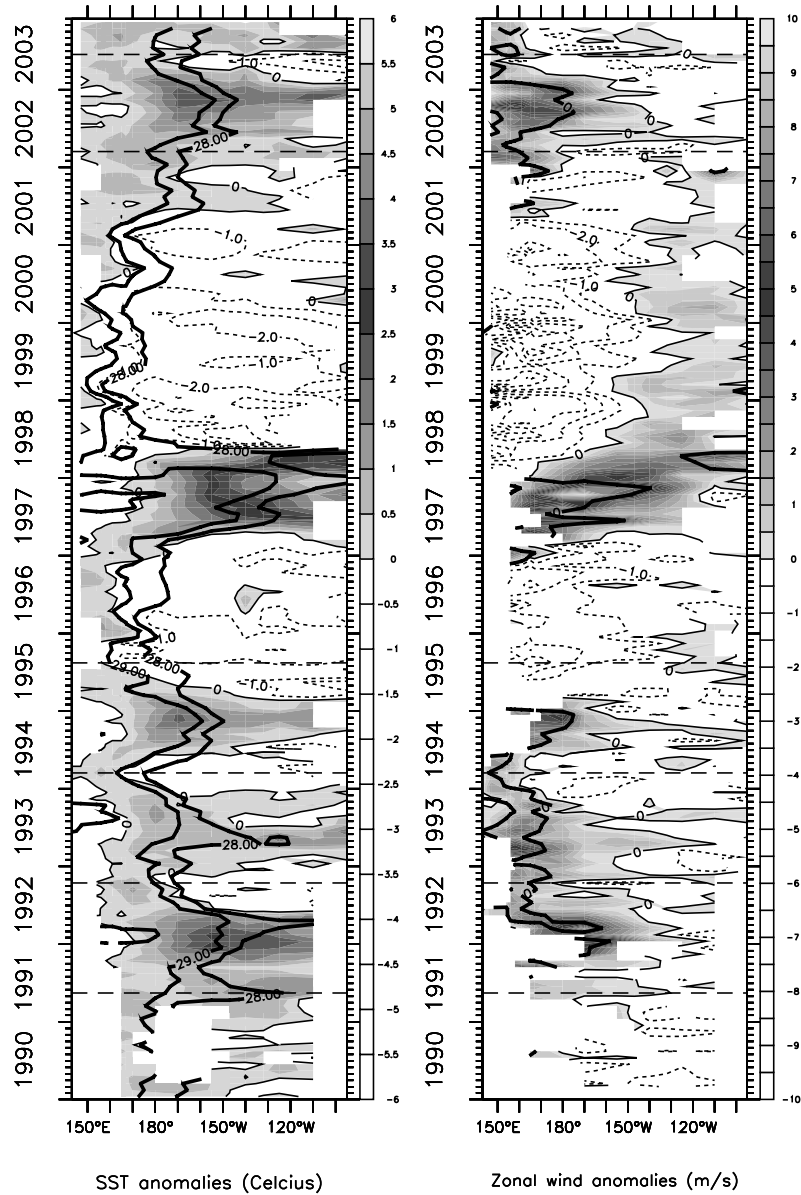


Figure 3.1: Hovmöller diagram of SST anomalies (left) and zonal wind anomalies (right) from TAO/TRITON observations. The selected El Niño events are indicated by dashed lines. In the left panel the 28°C and 29°C isotherms are indicated by black contours, representing the zonal movement of the edge of the warm pool. The black contour in the right panel indicates where the zonal wind is zero, indicating zonal movement of the wind field.

3.2. Observations

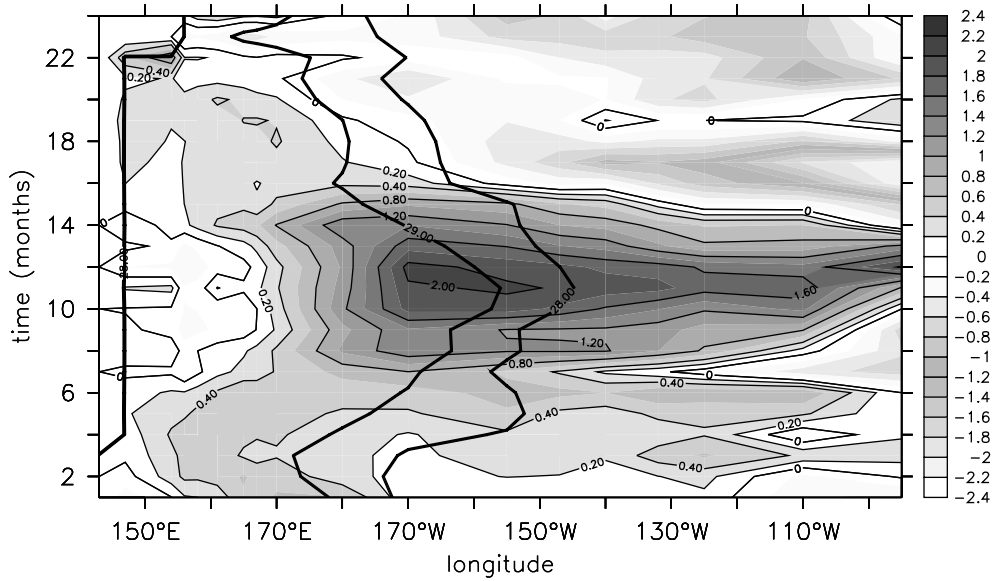


Figure 3.2: A composite plot of SST anomalies (K) from TAO/TRITON observations for the 1991/92, 1994/95 and 2002/03 El Niño events. The zonal movement of SST anomalies during the development and breakdown phases is clearly visible. The 28°C and 29°C isotherms are indicated by black contours.

development and zonal movement can be visualized by creating a composite image where several events are averaged together, after aligning the peaks in time. This was done for the 1991/92, 1994/95 and 2002/03 events in figure 3.2. Over a period of approximately 18 months, SST anomalies travel from the western Pacific (150°E) to the central Pacific (160°W) and back. The composite zonal wind field is shown in figure 3.3. The zonal wind field is linked to the SST anomalies: westerly wind anomalies are located west of the maximum SST anomaly. Finally, the surface wind speed is also available from TAO/TRITON observations, the composite field is plotted in Fig. 3.4). There is a clear match between areas with positive SST anomalies and areas of reduced wind speed, suggesting a causal relationship between wind speed and SST.

Several mechanisms are known to have an important influence on SST in the western and central Pacific: latent heat flux, short wave and long wave radiation, horizontal and vertical advection. The advection fields are not readily available from observations, and the effect of the surface fluxes on SST is hard to determine without knowledge of the depth of the mixed layer on which they act. We therefore revert to the use of a model simulation which enables us to compute the surface layer heat budget and compare the different terms quantitatively.

Chapter 3. Evolution of SST anomalies in the warm pool

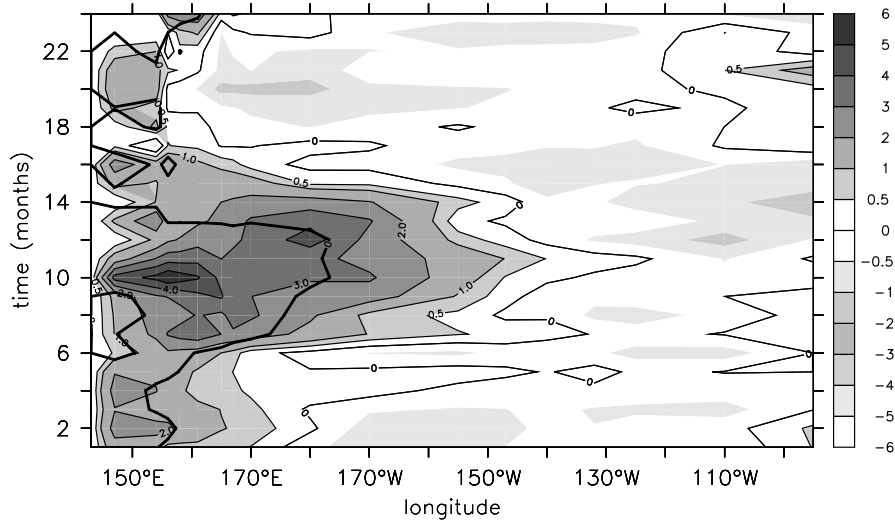


Figure 3.3: A composite plot of zonal wind anomalies (m s^{-1}) from TAO/TRITON observations for the 1991/92, 1994/95 and 2002/03 El Niño events. The zonal movement of the SST anomalies can be seen in the zonal wind pattern as well. The black contour indicates where the total zonal wind is zero.

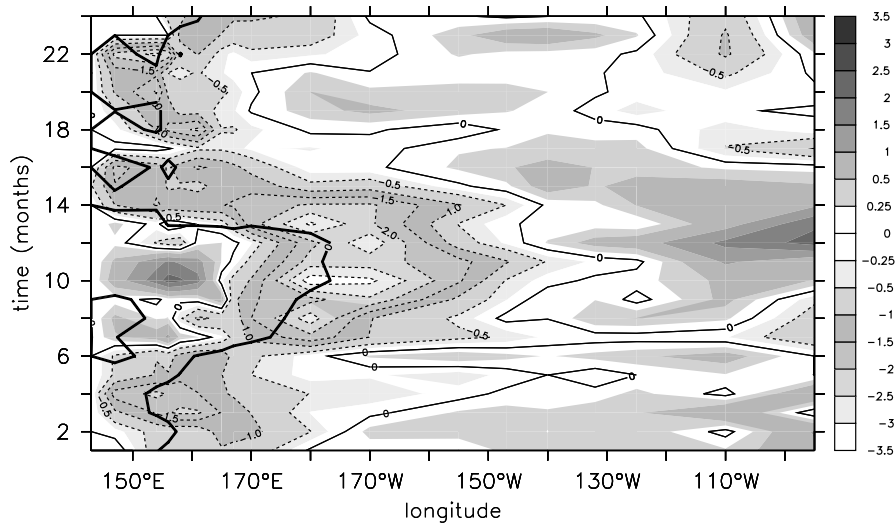


Figure 3.4: A composite plot of wind speed anomalies (m s^{-1}) from TAO/TRITON observations for the 1991/92, 1994/95 and 2002/03 El Niño events. The SST anomaly patterns in figure 3.2 are accompanied by areas of reduced wind speed, which causes reduced latent heat flux into the atmosphere and a reduction of the mixed layer depth. The black contour indicates where the total zonal wind is zero.

3.3 Model

3.3.1 Setup

The model used for the budget study is MICOM (Miami Isopycnic Coordinate Ocean Model) as described in Bleck et al. (1992). MICOM is an ocean model which does not use a regular depth axis but defines vertical layers in density coordinates. The model is forced with surface fluxes from the ERA40 reanalysis dataset, which is based on observations. ERA40 data is available from late 1957 to 2002, a MICOM simulation is performed for the period Jan-1985 to Jun-2002. The model resolution is approximately 1° for both longitude and latitude, with 20 layers and a vertical resolution at the surface of approximately 20 m. The selected domain includes the Indian ocean and the equatorial Pacific: 30°E – 70°W , 30°S – 30°N .

The model results generally show good agreement with observations of the tropical Pacific. The ERA40 wind forcing results in a good simulation of zonal and meridional currents, compared to TAO/TRITON observations. The mean SST is simulated reasonably well with the cold tongue somewhat too cold (down to $\sim 21^\circ\text{C}$ at 110°W) and the warm pool slightly too warm at just over 30°C west of 150°E . There are three points where the model deviates significantly from observations. SST variations are too strong: during El Niño events the maximum SST anomalies in the model are up to 50% stronger than the observed SST anomalies. This is most likely caused by the second problem: the mean mixed layer depth. Fig. 3.5 shows the simulated mean mixed layer depth, it is up to a factor 2 too shallow compared to observational data from LODYC (de Boyer Montégut et al., 2004, uses a 0.03 kg m^{-3} density criterion). The largest deviations occur in the central Pacific, around 160°W . In the eastern and western equatorial Pacific the model does much better, with simulated mixed layer depths close to observations. The effect of the shallow mixed layer will be discussed in section 3.5.2. Despite deviations in the mean, the mixed layer depth variability in the model is reasonable, when compared with TAO/TRITON observations using $\text{SST} - 0.25 \text{ K}$ as the mixed layer depth criterion in both datasets. Finally, the vertical temperature gradient below the mixed layer is too strong in the model, leading to an overestimation of the contribution of upwelling to the mixed layer temperature budget.

3.3.2 Budget study

The isopycnic coordinate system used in the model is an advantage for this study: the mixed layer below the ocean surface is always defined as a single layer, even when it varies in depth. It is therefore relatively easy to compute a closed temperature budget for this layer. The SST equation for the model can be written as

$$\frac{\partial T}{\partial t} = -uT_x - vT_y - \frac{\theta(w_e)(T - T_s)w_e}{h} + \frac{w_c}{h} + \frac{F}{\rho c_p h} + \frac{D}{h} \quad (3.1)$$

where T is SST, T_s is the temperature of the second layer, u and v are zonal and meridional currents, w_e is entrainment defined as the flux passing through the

Chapter 3. Evolution of SST anomalies in the warm pool

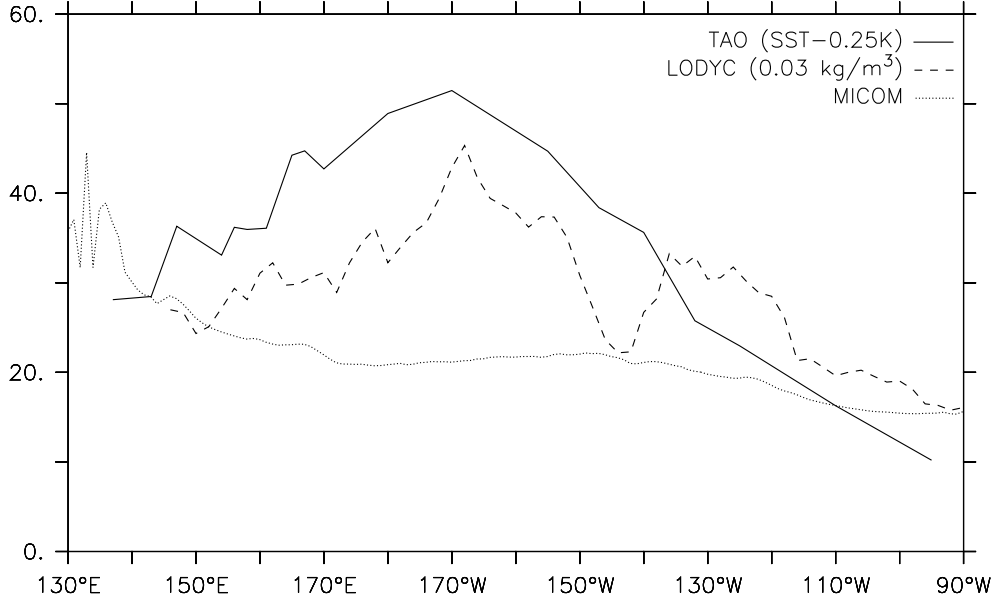


Figure 3.5: Annual mean mixed layer depth for TAO/TRITON data (SST - 0.25 K), LODYC (density criterion, 0.03 kg m^{-3}) and MICOM .

bottom of the mixed layer, θ is a step function depending on the sign of w_e , h is the mixed layer depth, w_c is convection to deeper layers, F is the surface forcing and D is horizontal diffusion within the surface layer.

The following contributing terms are distinguished in the budget: horizontal advection ($-uT_x - vT_y$), vertical advection including both upwelling and entrainment ($-\theta(w_e)(T - T_s)w_e/h$), surface fluxes ($F/(\rho c_p h)$) split up in net radiation, latent and sensible heat flux, convection to deeper layers (w_c/h) and diffusion (D/h). Each of these terms is defined in units of K month^{-1} . Within the selected domain the convection, diffusion and sensible heat flux terms are negligible compared to the other budget terms. The advection terms are computed by the model, net radiation is a prescribed forcing term and latent heat flux is computed by the model, closing the budget.

To visualize the results of the budget study, they are averaged over the region 2°S – 2°N and smoothed with a 10° zonal boxcar filter. By selecting a single point in time (snapshot), the contribution of all budget terms can be shown together in one plot, as a function of longitude. This is repeated for different times during the development of a single El Niño event to show how the contributions of the budget terms change.

The development and breakdown of the El Niño event will be shown, while focusing on the zonal movement. Three time points are selected during the development of an event: one during the growth phase when there is eastward propagation of the SST anomalies, one at the peak of the event and one during the westward propaga-

3.4. Results

tion of SST anomalies after the peak. Because the development of an El Niño event is coupled to the seasonal cycle, these 3 points occur approximately in the same month: August, December and April. The model simulation ends in June 2002, therefore the 2002/03 event has been left out of the analysis.

3.4 Results

The budget terms for the 1991/92, 1992/93 and 1994/95 events are shown in figures 3.6, 3.7 and 3.8. For each point in time (shown in the top left corner) the upper panel shows the SST and τ_x anomalies. The lower panel shows the budget terms in units of K month^{-1} : fluxes have effectively been converted to SST tendencies by dividing by the local heat capacity of the mixed layer. Fig. 3.6 shows the onset of the events, Fig. 3.7 shows the peak and Fig. 3.8 shows the decay phase. The relative importance of the budget terms as well as the mechanisms behind them will be discussed for each of these phases.

3.4.1 Growth phase

During the growth phase, the initial SST anomaly moves from about 150°E to 170°W . In figure 3.6 the SST anomaly has arrived approximately at 170°E . The westerly wind anomalies already extend eastward to 140°W , but the strongest zonal wind anomaly is just west of the maximum SST anomaly.

Horizontal advection

The horizontal advection term in the budget ($-uT_x - vT_y$ in Eq. 3.1) is dominated by zonal advection. This has been verified with the NCEP Ocean Reanalysis dataset, by computing the various contributions of meridional and horizontal advection to the heat budget. In MICOM the contribution of horizontal advection is relatively small: the main effect is warming at the center of the SST anomaly, reinforcing it without causing a zonal shift. A second, weaker effect is cooling east of the SST anomaly. The warming effect is of the same strength as the combined warming by all terms, but it is weaker than the individual warming by entrainment and latent heat flux. During the growth phase of the El Niño event, warming by horizontal advection is caused mostly by anomalous zonal advection across the mean zonal temperature gradient $u' \partial \bar{T} / \partial x$.

Entrainment

During the growth phase warming by entrainment ($-\theta(w_e)(T - T_s)w_e/h$ in Eq. 3.1) occurs approximately centered under the SST anomaly around 170°E . The strength of the warming is moderate, comparable to warming by latent heat flux and the net total warming by all budget terms. East of the SST anomaly entrainment causes weak cooling. Anomalous upwelling is the main factor in the entrainment term, on the

Chapter 3. Evolution of SST anomalies in the warm pool

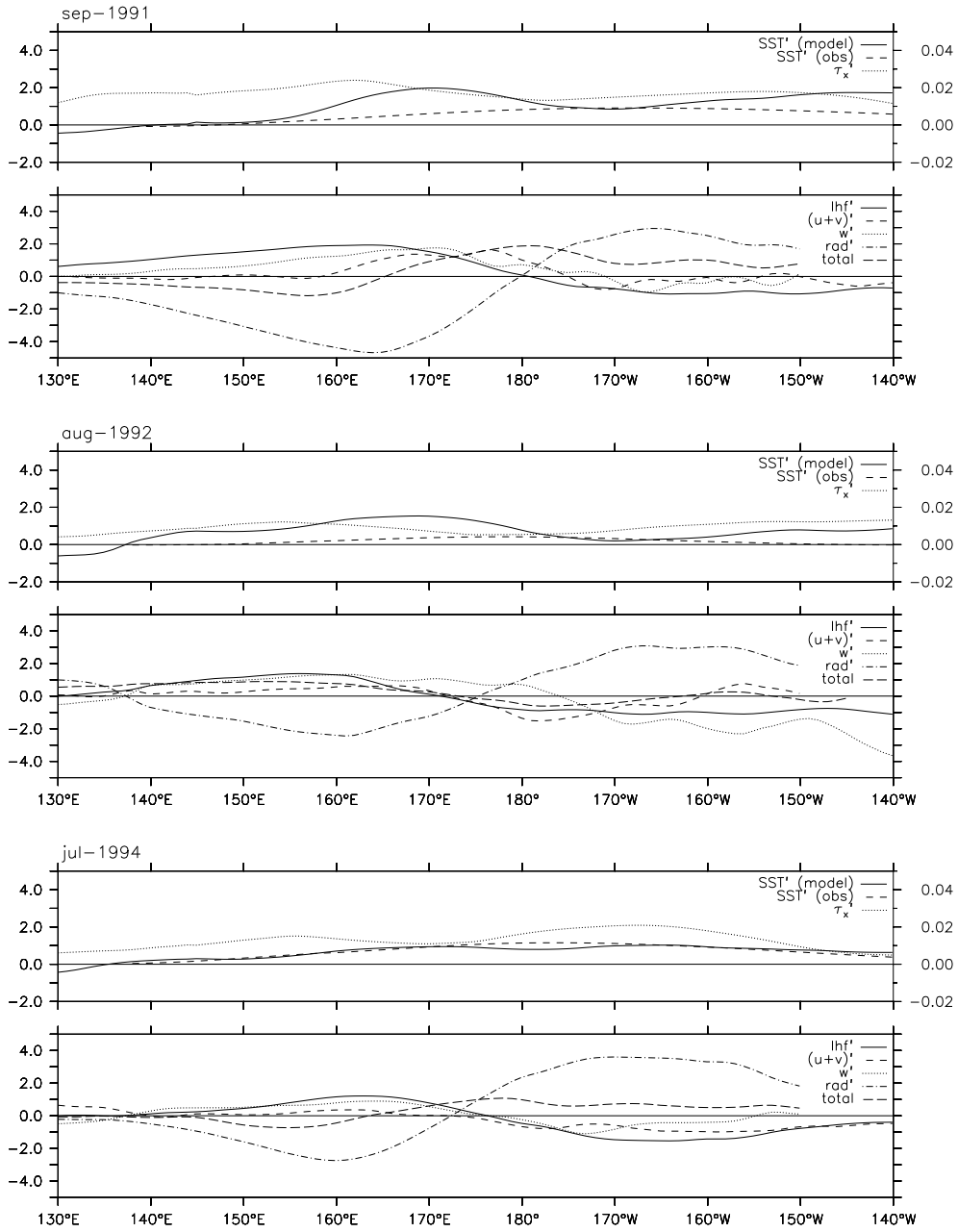


Figure 3.6: SST anomalies, wind stress anomalies (top panels) and mixed layer budget terms presented as temperature tendencies (bottom panels) for the onset of the 1991/92 (top), 1992/93 (center) and 1994/95 (bottom) El Niño events. Units are K for SST (left axis), Pa for wind stress (right axis) and K month⁻¹ for the budget terms.

3.4. Results

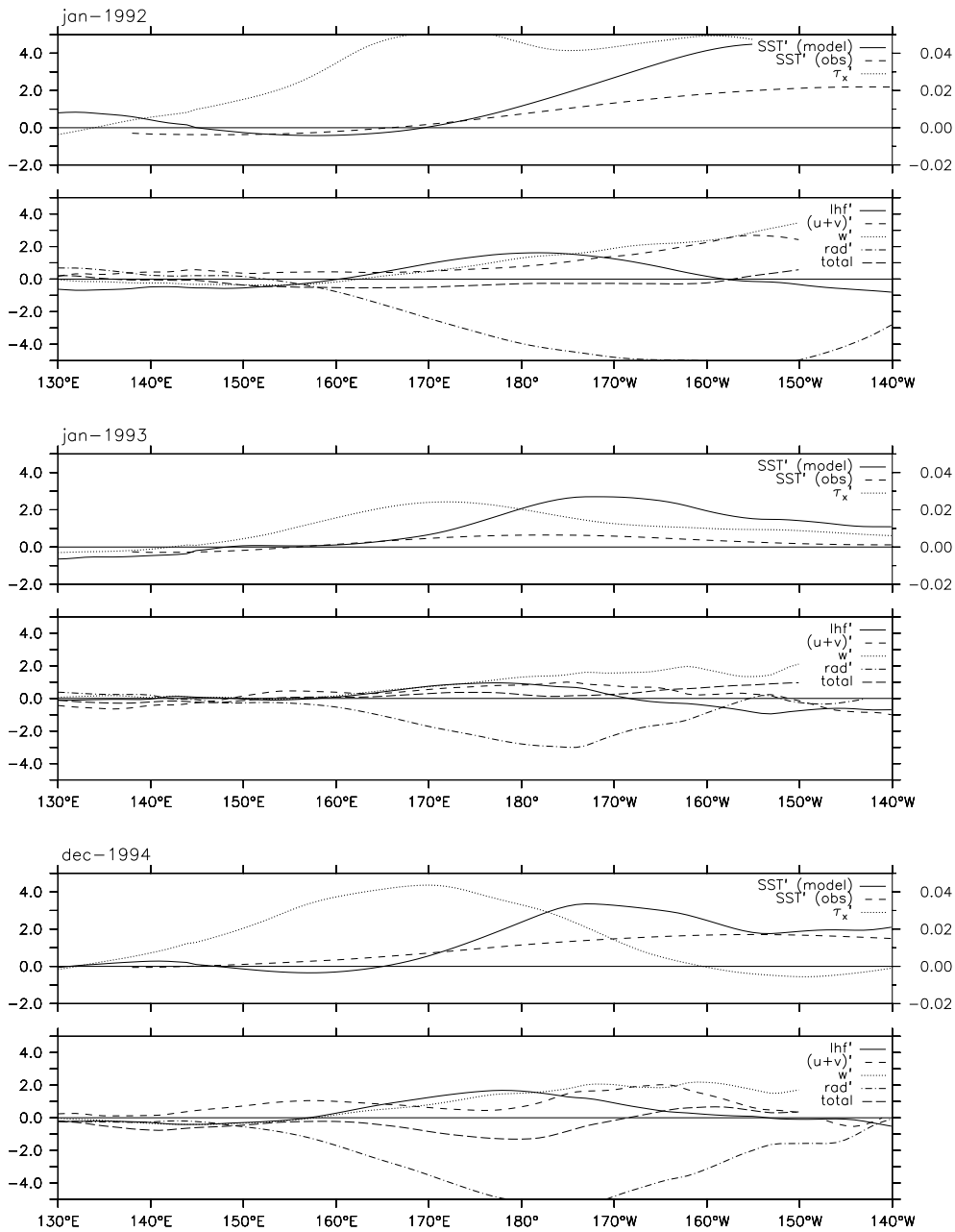


Figure 3.7: SST anomalies, wind stress anomalies (top panels) and mixed layer budget terms presented as temperature tendencies (bottom panels) for the peak of the 1991/92 (top), 1992/93 (center) and 1994/95 (bottom) El Niño events. Units are K for SST (left axis), Pa for wind stress (right axis) and K month⁻¹ for the budget terms.

Chapter 3. Evolution of SST anomalies in the warm pool

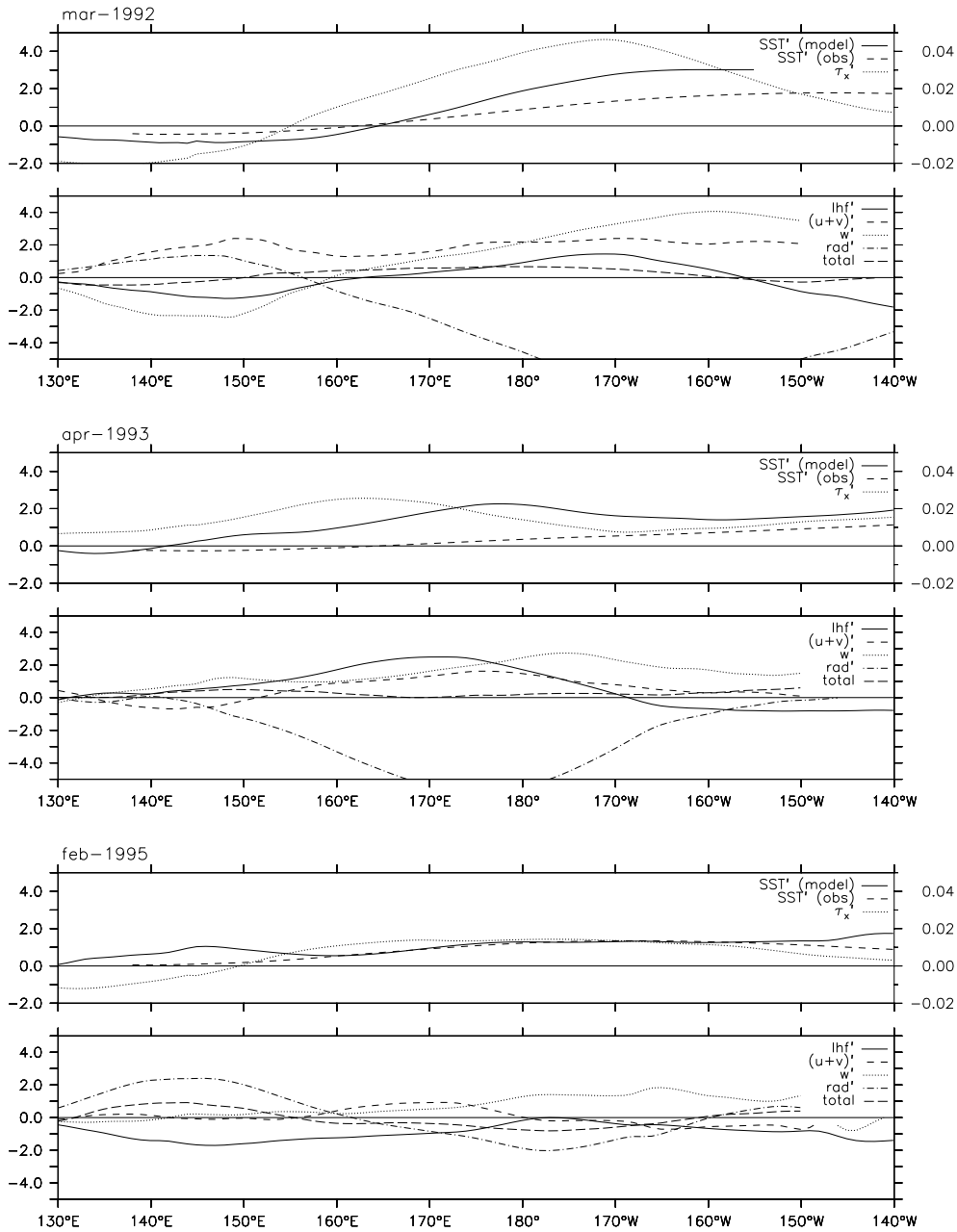


Figure 3.8: SST anomalies, wind stress anomalies (top panels) and mixed layer budget terms presented as temperature tendencies (bottom panels) for the decay phase of the 1991/92 (top), 1992/93 (center) and 1994/95 (bottom) El Niño events. Units are K for SST (left axis), Pa for wind stress (right axis) and K month⁻¹ for the budget terms.

3.4. Results

equator it is controlled by anomalous zonal wind. Note that the strength of this budget term is overestimated in the model, due to a too strong mean vertical temperature gradient below the mixed layer.

Surface forcing

Warming by reduced latent heat flux occurs just west of the maximum SST anomaly. East of the SST anomaly latent heat flux has a cooling effect, hampering the eastward development of the SST anomaly. Latent heat flux is directly related to surface wind speed, the relation between zonal wind and wind speed will be investigated in more detail in section 3.5.

The largest single term contributing to the budget is net radiation. West of and centered at the SST anomaly cooling occurs, dominated by reduced incoming short wave radiation due to increased cloud cover (cloud feedback). Surprisingly, east of the SST anomaly and the dateline *warming* occurs due to the radiation term. This is the only term in the budget which explains the eastward zonal movement of the SST anomaly during the growth phase of El Niño. An investigation of the separate short wave and long wave radiation terms shows that there is only a small increase of the net radiation flux into the ocean. The cause of the warming trend is shoaling of the mixed layer in the east when the El Niño event develops. The mean net radiation flux into the ocean (which compensates cooling by mean upwelling, latent heat flux and horizontal advection) now acts upon a more shallow layer of water with a lower heat capacity. This results in anomalous warming by mean radiation and a vertical redistribution of heat between the mixed layer and the layer below it. The effects of mixed layer depth will be discussed further in section 3.5.

3.4.2 Peak phase

At the peak of the event, the maximum SST anomaly lies between 170°W and 150°W. There is a strong westerly wind anomaly west of the maximum SST anomaly extending east as far as 140°W, except in December 1994 where it stops at 160°W. The decay phase is about to set in, so from here on the SST anomaly will weaken and move westward. West of 160°E, all budget terms are small.

Horizontal advection

Horizontal advection has a relatively strong warming effect approximately centered under the maximum SST anomaly. This is caused by anomalous zonal advection driven by the westerly wind anomaly.

Entrainment

Entrainment is the strongest warming term during the peak, starting at the SST anomaly and growing stronger to the east. In the west entrainment is dominated by reduced anomalous upwelling driven by the anomalous westerly wind, further

east it is dominated by thermocline feedback due to mean upwelling, deepening of the thermocline and the resulting reduction of the vertical temperature gradient.

Surface forcing

Reduced latent heat flux due to reduced wind speed generates warming on the western flank of the SST anomaly. The effect is weaker than the warming by upwelling and horizontal advection.

Radiation provides a strong cooling term approximately centered on the SST anomaly. Similar to the peak phase, the cooling is caused mostly by cloud feedback which reduces incoming solar radiation. During the event the cooling effect gradually becomes stronger than the combined warming by latent heat flux, horizontal advection and upwelling. Radiation is the main term responsible for the weakening of the SST anomaly directly after the peak of the event.

3.4.3 Decay phase

The SST anomaly has been reduced in strength and smoothed zonally, there is no longer a clear peak to be seen. The SST anomaly is still weakening, and it moves westward with the eastern side cooling and the western side warming up. Due to differences between the events it is much less clear which budget term is the most important here. We focus on the 1991/92 and 1992/1993 events (Fig. 3.8) because they resemble observational data the most.

Horizontal advection

Horizontal advection provides warming west of the SST anomaly leading to westward movement, both in March 1992 and April 1993. Using the NCEP Ocean Reanalysis it is confirmed that the horizontal advection term generally is the dominant warming term in the west, responsible for the westward shift of the SST anomaly. The warming is caused by mean zonal advection across an anomalous zonal temperature gradient. The anomalous westerly winds have been reduced in strength across the western/central Pacific, but the central and eastern Pacific are still anomalously warm. The mean trade winds and corresponding zonal advection transport the warm water back to the western Pacific.

Entrainment

The effect of entrainment during the decay phase is similar to the peak phase, relatively strong warming is generated mostly east of the dateline. This warming slows the extinction of the SST anomaly in the central and eastern Pacific.

3.5. Discussion

Surface forcing

Net radiation is still the main cause for cooling at the SST anomaly, acting as a damping term. The latent heat flux term provides cooling east of 160°W . This is because the westerly wind anomaly has been reduced in strength, increasing the wind speed and latent heat flux. The mixed layer depth increases as a result of the increased wind speed, up to approximately twice the mean depth. This reverses the process described in section 3.4.1 and causes anomalous cooling by radiation, which is only partially canceled by anomalous warming through latent heat flux and entrainment. In March 1992 this occurs around 170°W – 160°W , in April 1993 it occurs around 170°E – 180° .

3.4.4 Summary

Figure 3.9 summarizes the effects of zonal advection, latent heat flux and mixed layer depth anomalies on SST, for the growth phase and decay phase of an El Niño event. The results were obtained from an idealized one-dimensional model. Annual mean SST, zonal wind, mixed layer depth and vertical heat flux were obtained from observations. An artificial SST anomaly is prescribed, typical for the growth and decay phase respectively. For the growth phase an artificial westerly wind event is prescribed, for the decay phase the zonal wind response to the prescribed SST field is computed. Zonal advection and mixed layer depth are then computed from zonal wind. In each panel of figure 3.9, two lines show how SST would develop in one month if only the specified mechanism was active.

During the growth phase, the idealized model confirms that zonal advection sharpens the SST anomaly without moving it zonally. Latent heat flux strengthens the SST anomaly and causes weak eastward propagation. Mixed layer depth anomalies cause eastward propagation of the SST anomaly without strengthening it. During the decay phase, both zonal advection and latent heat flux cause westward propagation of the SST anomaly. The mixed layer is deepened around the dateline, resulting in cooling.

3.5 Discussion

The results from the budget study show that not only zonal wind anomalies are important (driving anomalous zonal advection and anomalous upwelling) but also surface wind speed anomalies: these affect latent heat flux and the mixed layer depth. Mixed layer depth anomalies are found to be important during the development of an El Niño event, as they generate warming east of the SST anomaly which causes eastward propagation. During the decay of the event the opposite occurs: mixed layer depth anomalies generate cooling which weakens the SST anomaly and causes westward propagation. To gain a better understanding, the relation between zonal wind and wind speed is discussed first, followed by the effect of mixed layer depth anomalies on the budget.

Chapter 3. Evolution of SST anomalies in the warm pool

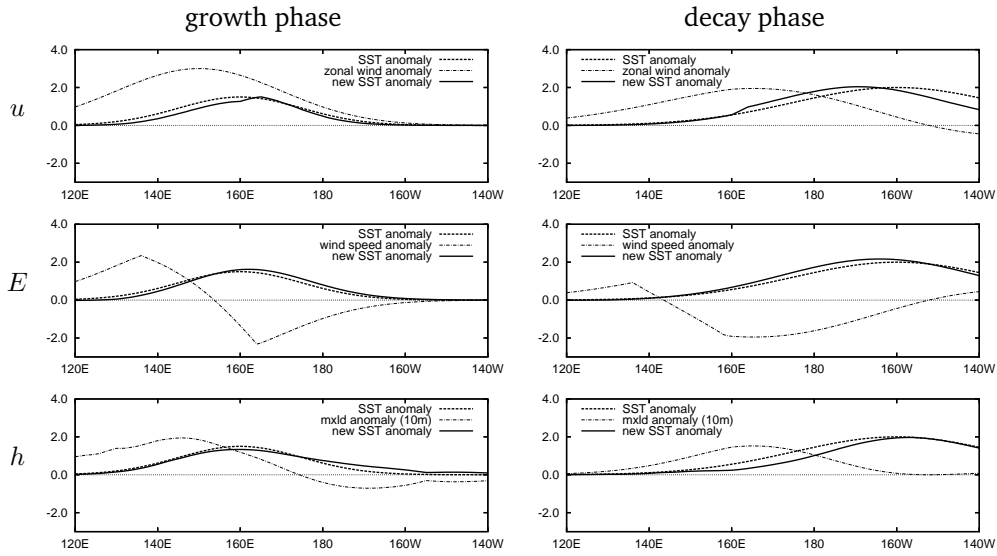


Figure 3.9: From top to bottom: the effect of zonal advection, latent heat flux and mixed layer depth anomalies on SST in an idealized model. The left column shows the growth phase of the event, with a prescribed initial SST anomaly (K, dashed line) and westerly wind anomaly (m s^{-1} , dash-dot line). The right column shows the decay phase of the event, with SST prescribed and the zonal wind response computed from the prescribed SST field. The model calculates SST development for one month (solid line), only for the selected mechanism.

3.5. Discussion

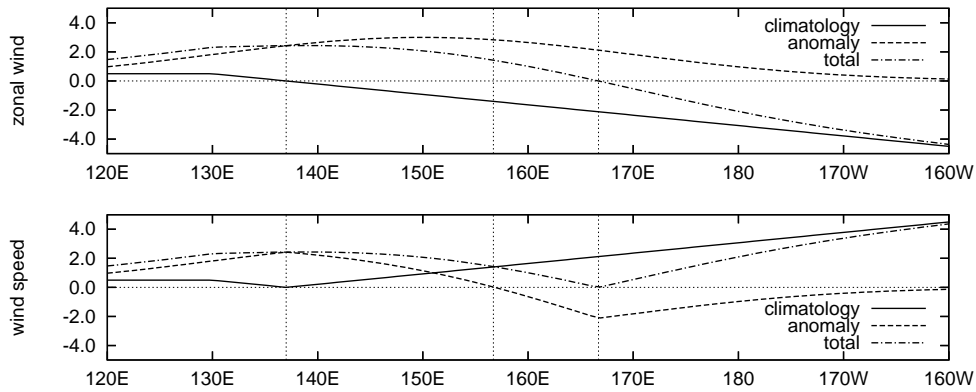


Figure 3.10: Top panel: the equatorial climatological zonal wind field, a westerly wind anomaly and the resulting total zonal wind field. Bottom panel: the climatological wind speed (neglecting meridional wind), the total wind speed and the wind speed anomaly.

3.5.1 Zonal wind and wind speed

Fig. 3.10 (top panel) shows a schematic representation of the climatological zonal wind. When a westerly wind anomaly occurs (either an external weather event or the response to an existing SST anomaly) a new zonal wind field is obtained as shown in the top panel of Fig. 3.10. A schematic representation of the resulting wind speed is shown in the bottom panel of Fig. 3.10. To simplify matters meridional wind is ignored, this does not make a significant difference because the zonal wind component is generally much stronger in the equatorial Pacific. In the far western Pacific the total wind speed increases toward the east. From the climatological zero point toward the east total wind speed decreases, up to a point where the westerly wind anomaly compensates the easterly trade winds and the wind speed is now zero. East of that zero point the wind speed increases again as the background winds become stronger than the westerly wind anomaly. The resulting wind speed anomaly is positive in the western Pacific and negative in the central Pacific and as far east as the westerly wind anomaly extends. This matches well with both observations and model results.

3.5.2 Mixed layer depth

The relation between wind speed and mixed layer depth is controlled by the turbulent kinetic energy (TKE) balance as described in Kraus and Turner (1967). Changes in mixed layer depth h are computed by

$$\Delta h = \frac{E\Delta t}{b_{\text{mix}} - b_{\text{sub}}} \quad (3.2)$$

Chapter 3. Evolution of SST anomalies in the warm pool

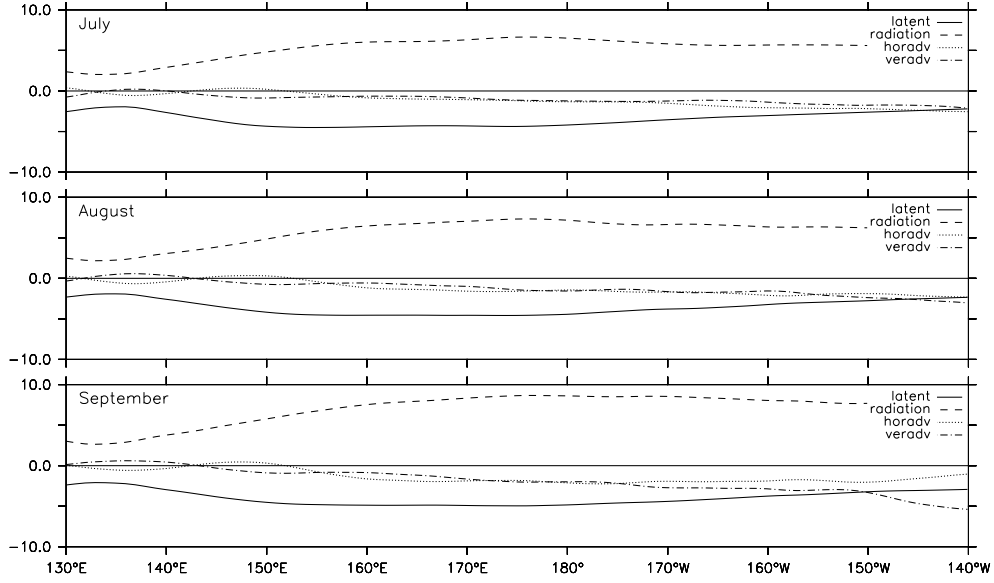


Figure 3.11: The mean surface layer budget terms for the months July (top panel), August (middle panel) and September (bottom panel). Variables shown are latent heat flux, net radiation, horizontal advection and vertical advection. All variables in units of K month^{-1} .

where $E\Delta t$ is the change in TKE and b_{mix} and b_{sub} are the buoyancy of the mixed layer and the layer below it. The TKE equation as used in the MICOM model is

$$\underbrace{mu_*^3}_{(1)} - \frac{h}{2} \underbrace{(B(h) - w_e \Delta b)}_{(2)} - \underbrace{h\epsilon_m}_{(3)} = 0 \quad (3.3)$$

(1) represents TKE generated by wind, with m a constant and u_* the friction velocity: changes in wind speed have a strong influence on the mixed layer depth. (2) is TKE generated by buoyancy fluxes with $B(h)$ the surface buoyancy flux, w_e the entrainment velocity and Δb the jump in buoyancy at the bottom of the mixed layer. (3) represents dissipation of TKE into heat.

The climatological balance between the terms in the SST equation will be used to illustrate and quantify the warming that results from a reduction of the mixed layer depth. Fig. 3.11 shows the climatological budget terms radiation, latent heat flux, horizontal advection and vertical advection in K month^{-1} for the months July, August and September. There is a balance between these mean terms, their sum is approximately zero as seasonal changes in surface temperature are much smaller than the individual terms. In the warm pool, radiation and latent heat flux are the two dominant opposed terms. A change in mixed layer depth changes its heat capacity, shifting the balance between the horizontal and vertical budget terms. This results

3.6. Summary and Conclusions

in net warming (cooling) when the mixed layer shoals (deepens). The warming can be computed by applying the change in heat capacity only to the vertical terms, the horizontal advection term is unaffected. Equation 3.4 shows the linearization of the warming effect of the vertical heat flux F_v on the mixed layer of depth h . The first term is the effect of anomalous heat flux F'_v , the second term is the effect of anomalous mixed layer depth h' :

$$\left(\frac{F_v}{h}\right)' \approx \frac{F'_v}{\bar{h}} - \frac{h'}{\bar{h}} \frac{\overline{F_v}}{\bar{h}} \quad (3.4)$$

The warming related to mixed layer depth changes is computed for September 1991, August 1992 and July 1994, matching the three events in Fig. 3.6. The strongest warming by radiation occurs around 165°W. Averaged over the three events, the surface wind speed at this location was reduced from approximately 6 m s⁻¹ to 5 m s⁻¹. The mixed layer depth is reduced to roughly 60% of the climatological mean (from 25 m to 15 m). The sum of the mean vertical budget terms (warming by radiation, cooling by latent heat flux and entrainment) is approximately +1.5K month⁻¹ on average, the reduced heat capacity increases this to approximately +2.5K month⁻¹. The resulting net warming of the surface layer is approximately 1 K month⁻¹. During the decay phase as shown in Fig. 3.8 the opposite occurs: the mixed layer depth increases to approximately 180% of the climatological mean (from 25 m to 45 m), resulting in a net cooling of approximately 0.6 K month⁻¹.

Warming of the mixed layer due to a reduction of the mixed layer depth occurs in all three events. The increased warming by mean solar radiation is not compensated by the increased cooling by mean latent heat flux and mean vertical advection. Heat is redistributed between the mixed layer (warmer) and the layer below it (colder). The opposite effect occurs when the mixed layer depth is increased.

Both the simulated mean mixed layer depth and the variability are approximately a factor two too small when compared to TAO/TRITON observations, using SST - 0.25 K as the mixed layer depth criterion. However, the patterns of mixed layer depth anomalies and the relative mixed layer depth variations are simulated reasonably well. Warming of the surface layer due to a reduced mixed layer depth occurs in the observations at similar times and locations during the development of the events as in the simulations. The strength of the observed warming is weaker than in the simulation though, approximately 0.5 K month⁻¹.

The mixed layer depth was found to be an important factor in the surface layer temperature equation. Especially when the time-mean fluxes are large with a balance between vertical and horizontal fluxes, a change in mixed layer depth can cause relatively strong anomalous heating or cooling.

3.6 Summary and Conclusions

El Niño events generally start and sometimes end in the western equatorial Pacific, and are characterized by zonal movement of SST anomalies. The mechanisms behind the growth, movement and decay of these SST anomalies have been investigated.

This was done with a mixed layer heat budget of the equatorial Pacific, obtained from a forced ocean model simulation. The model uses isopycnic coordinates and simulates a mixed layer that varies in depth. For each term in the heat budget the contribution to the temperature tendency of the mixed layer is computed separately.

The results of the budget study emphasize the importance of the SST-wind coupling in the western and central Pacific. Not just zonal wind anomalies (causing anomalous upwelling and zonal advection) but also wind speed anomalies (generating anomalous latent heat flux and changes in mixed layer depth) are important. Changes in mixed layer depth affect the balance between the mean terms in the SST equation, because radiation, latent heat flux and upwelling are affected while horizontal advection is not. The result is a vertical redistribution of heat between the mixed layer and the layer below it, visible as relatively strong surface warming (reduced mixed layer depth) or cooling (increased mixed layer depth) by the mean radiation flux.

During the growth phase of the event anomalous westerly winds extend eastward across the existing SST anomaly, past the dateline into the central Pacific, causing anomalous zonal advection and reducing the wind speed and the mixed layer depth. The reduced mixed layer depth causes warming as described above, and contributes to the eastward growth of the SST anomaly together with anomalous zonal advection. After the peak of the event, weakening of the SST anomaly is caused by radiative cooling, both through decreased net incoming radiation and by deepening of the mixed layer as the easterly trade winds pick up strength. After the peak of the event westward movement of the SST anomaly is caused by warming in the western Pacific through mean zonal advection across an anomalous temperature gradient, and radiative cooling east of the SST anomaly.

Previous studies of the western Pacific emphasized the importance of zonal advection for the generation of warming that leads to eastward propagation of SST anomalies during the development of an El Niño event. We find that mixed layer depth anomalies also contribute to warming and eastward propagation. Although the effect is somewhat overestimated in the model used for this study, observational data indicates that both mixed layer depth anomalies and anomalous zonal advection are important for the eastward propagation of SST anomalies. Because the time-mean heat fluxes in the equatorial Pacific are large, a shift in the balance due to a change in mixed layer depth can cause relatively strong warming or cooling. This makes surface wind speed an important factor in the development of SST anomalies, not just as a driving force for evaporation, but also as a cause for changes in the mixed layer depth.

Chapter 4

El Niño and greenhouse warming

The changes in model ENSO behavior due to an increase in greenhouse gases (according to the IPCC Business-As-Usual scenario) are investigated using a 62 member ensemble 140-year simulation (1940–2080) with the National Center for Atmospheric Research Community Climate System Model (CCSM, version 1.4). Although the global mean surface temperature increases with about 1.2 K over the period 2000–2080, there are no significant changes in the ENSO period, amplitude and spatial patterns. To explain this behavior, an analysis of the simulation results is combined with results from intermediate complexity coupled ocean-atmosphere models. It is shown that this version of the CCSM is incapable of simulating a correct meridional extension of the equatorial wind stress response to equatorial SST anomalies. The wind response pattern is too narrow and its strength is insensitive to background SST. This leads to a more stable Pacific climate system, a shorter ENSO period and a reduced sensitivity of ENSO to global warming.

¹This chapter is based on the paper “El Niño and Greenhouse Warming: Results from Ensemble Simulations with the NCAR CCSM” by H. Zelle, G. J. van Oldenborgh, G. Burgers and H. Dijkstra, as submitted to Journal of Climate in October 2004 and revised in February 2005.

4.1 Introduction

Interannual variations in the present climate strongly involve El Niño/Southern Oscillation (ENSO) in the tropical Pacific. This phenomenon is caused by ocean-atmosphere interaction in the equatorial Pacific. The surface winds are influenced by the sea-surface temperature (SST) which subsequently affect the ocean currents and ocean heat transport causing changes in SST. The time scale of variability is determined by ocean adjustment processes (Philander, 1990; Neelin et al., 1998; Dijkstra and Burgers, 2002).

From proxy data, more and more information becomes available on the behavior of ENSO under different global mean temperatures. Based on the analysis of annually banded corals from Papua New Guinea, Tudhope et al. (2001) show that ENSO has existed for the past 130 ka. However, there have been substantial changes in its strength through time. Based on analysis of Ecuadorian varved lake sediments, Rodbell et al. (1999) find that ENSO periods were larger than 15 year during the interval 15 ka - 7 ka and that modern periodicities of 2 - 8 years appeared afterward. Data from microfossils show that ENSO events were less intense around 3 ka but more pronounced around 1.5 ka (Woodroffe et al., 2003).

The variations in strength of ENSO events over the last 150 years are better known from observational data. According to NCEP data, the standard deviations of the Southern Oscillation Index (SOI, normalized sea level pressure difference between Darwin and Tahiti) and the Niño3.4-index (SST anomalies averaged over the region 5°S–5°N, 170°W–120°W) for 1951–1975 were 1.59 ± 0.14 and 0.78 ± 0.07 respectively, and 1.82 ± 0.19 and 0.95 ± 0.09 for the period 1976–2000. The error margins indicate the 95% confidence level interval. This shows that the amplitude of these indices has increased (for Niño3.4 this is partly due to better sampling since 1980), raising concern that ENSO may be intensifying as a result of global climate change (Trenberth et al., 1997).

Model studies of the behavior of ENSO in a warmer climate show conflicting results. In some early models (Knutson et al., 1997), the mean zonal sea-surface temperature gradient decreased with little change in El Niño-like activity. In other early models (Timmermann et al., 1999), increasing greenhouse gas concentrations induced a more El Niño like mean state with more pronounced cold events than warm events. In the second version of the Hadley Centre model (HadCM2), changes in El Niño activity, frequency and phase locking are found. However, in the third version of the same model (HadCM3), no change in El Niño statistics is found (Collins, 2000). This is attributed to the differences in physical parameterization and not to the differences in resolution between the two versions of the model. In one coupled model (Noda et al., 1999), a change towards a more La Niña state is found. The credibility of the predictions of the response to global warming in the coupled models (an overview of the models is given in Latif et al., 2001) is also undermined by the lack of confidence in their simulation of cloud feedbacks.

One of the most comprehensive models used for studying the behavior of ENSO under different global mean temperatures is the NCAR - CCSM (Otto-Bliesner and Brady, 2001; Huber and Caballero, 2003). The model ENSO variability under present

4.2. Global warming in the ensemble simulations

climate conditions was studied in Otto-Bliesner and Brady (2001) using a 300 year simulation. The warm-pool/cold-tongue equatorial temperature gradient has a realistic amplitude. However, the cold tongue is located too far to the west and the mean SST is too symmetric with respect to the equator. The equatorial thermocline is slightly more diffuse than in observations. There is a reasonable simulation of the amplitude, phase and propagation features of the SST anomalies and thermocline anomalies. SST anomalies appear as a standing pattern whereas there is a slight eastward propagation of anomalies at the depth of the thermocline. The variability in the model is largest in the Niño3.4 region with a standard deviation of 0.77 K. The wavelet power spectrum shows that the period is in the 2–4 year range and hence relatively short compared with observations, which show a more diffuse spectrum with a period between 3–8 years.

In this study, we address the question of changes in ENSO behavior under an increasing global mean temperature. We use results from a 62 ensemble member simulation of the CCSM version 1.4 over the period 1940–2080, using the IPCC Business-As-Usual scenario for greenhouse gas forcing after 2000. The choice for this model version was motivated by computational constraints, the fact that it was carefully tuned to simulate the ENSO phenomenon rather well (Otto-Bliesner and Brady, 2001) and the relatively small effort involved in preparing the model system for our purpose. The procedure of the ensemble simulations is outlined in section 2, the results on the tropical Pacific climate system and its variability are presented in section 3. In section 4, we perform a detailed analysis using results from intermediate coupled ocean-atmosphere models which leads to the interpretation of the results from section 3. A summary and discussion is provided in section 5.

4.2 Global warming in the ensemble simulations

4.2.1 Model

The CCSM version 1.4 is a global climate model containing a primitive equation ocean and atmosphere model, a sea-ice model and a land-surface model. We have used the configuration as in Ammann et al. (2004). The atmosphere was run at T31 resolution (equivalent to a grid spacing of $3.75^\circ \times 3.75^\circ$) in latitude and longitude with 18 levels in the vertical and the highest model level at about 35 km. The land surface model distinguishes between specified vegetation types and contains a comprehensive treatment of surface processes. The ocean model was run using a grid with 25 vertical levels and a longitudinal resolution of 3.6° . The latitudinal resolution changes from 0.9° in the tropics to 1.8° in higher latitudes. The sea-ice model includes sea-ice thermodynamics and sea-ice dynamics. The coupled system does not require artificial corrections in the heat exchange between atmosphere and ocean to simulate a reasonable climate state (Boville et al., 2001).

An initial state (at 01-01-1940) was obtained from the simulations of Ammann et al. (2004). The climate system was integrated 62 times over the period 1940–2080. During the historical part of the simulation (1940–2000), greenhouse gas (GHG) con-

centrations, sulphate aerosols, solar radiation and volcanic aerosols were prescribed according to observational estimates, kindly provided by C. Ammann (Ammann et al., 2004). From 2000 onwards, the solar constant and sulphate aerosols were kept fixed. Only the GHG concentrations varied according to the IPCC Business-As-Usual scenario which is similar to the SRES-A1 scenario (Dai et al., 2001). The ensemble members differ only in a small random perturbation in the initial temperature field of the atmosphere, enough to lead to entirely different atmospheric evolutions within the first couple of weeks of the integrations. In the following analysis, the first 10 years (1940–1949) of the simulation have been discarded to remove any remaining model spin-up effects.

4.2.2 Changes in the global mean state

Fig. 4.1 shows the global mean surface air temperature as simulated by all 62 members, the ensemble mean and an observational estimate obtained from the Climatic Research Unit (CRU, Jones et al., 2001). The simulated temperatures cover the observations very well. The effects of the volcano eruptions of the Agung (1963), El Chichon (1982) and Pinatubo (1991) are clearly visible as a temporary cooling on the order of several tenths of a degree. The temperature rise after 2000 is solely due to the increasing concentrations of GHGs. Between 2000 and 2080 the global mean temperature has risen 1.2 K, extrapolating the rise from 1990 to 2100 leads to a global warming of about 1.7 K which can be compared with IPCC global mean temperature projections.

The difference pattern of the mean temperature over the 30-year periods 2050–2080 and 1950–1980 is plotted in Fig. 4.2a. Warming of up to 5 K occurs in the region above 40°N. In the equatorial Pacific the warming is less strong at about 1 K, the western equatorial Pacific heats up 0.2 K more than the eastern equatorial Pacific. The changes in precipitation between the 1950–1980 and 2050–2080 periods are shown in Fig. 4.2b as a percentage of the 1950–1980 mean. The largest relative changes are found over the Sahel, Antarctica, Greenland, the northern Indian ocean and the equatorial Pacific. In the western equatorial Pacific precipitation increases by about 2 mm month⁻¹.

Compared to other models that have been used in the IPCC Third Assessment Report (IPCC, 2001, Chapter 8: Model Evaluation), the CCSM configuration used here is on the low end with respect to sensitivity to GHG forcing. The extrapolated 1.7 K global temperature increase between 1990–2100 is just above the lower bound established in the TAR (1.4 K to 5.8 K) based on results from different model simulations and emission scenarios. The patterns of change in temperature and precipitation (up to 2080) have comparable features with those of the other models.

4.3 ENSO and Global Change

From the total data set emerging from the ensemble simulations the equatorial Pacific region was extracted, in particular for the variables zonal wind stress τ^x , the depth

4.3. ENSO and Global Change

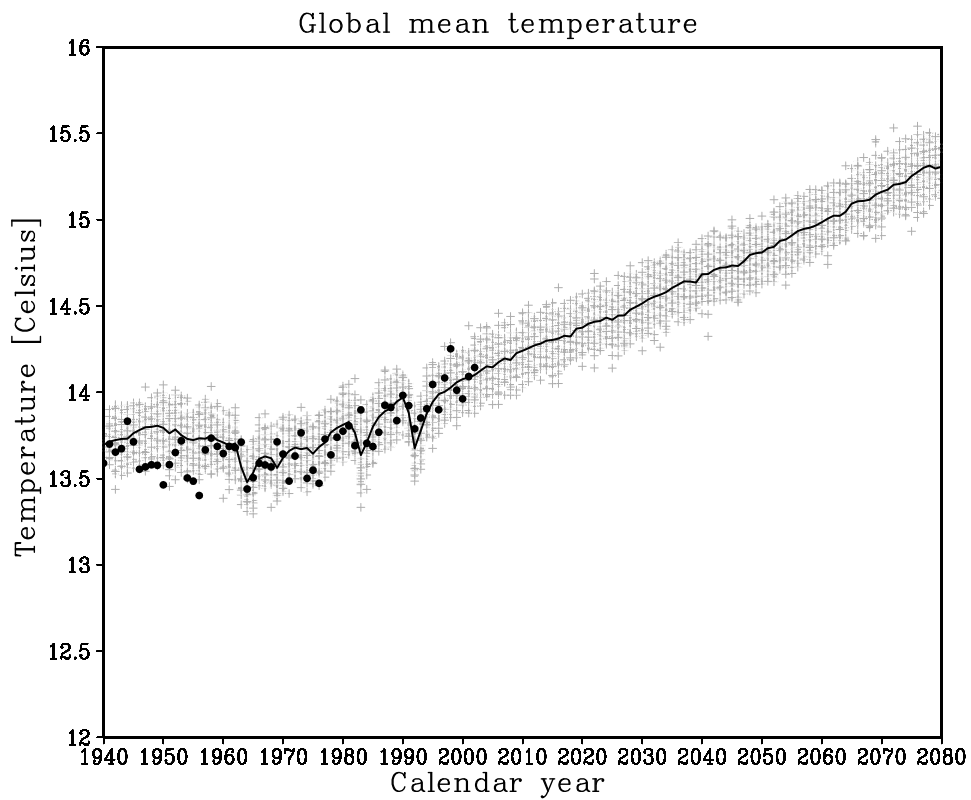


Figure 4.1: Global mean temperatures of all 62 simulations (light crosses), the ensemble mean (solid line) and observed temperatures from the Climate Research Unit (dark dots). The CRU time series obtained are anomalies with respect to the 1960–1990 period. We added the ensemble mean simulated temperature over this period.

Chapter 4. El Niño and greenhouse warming

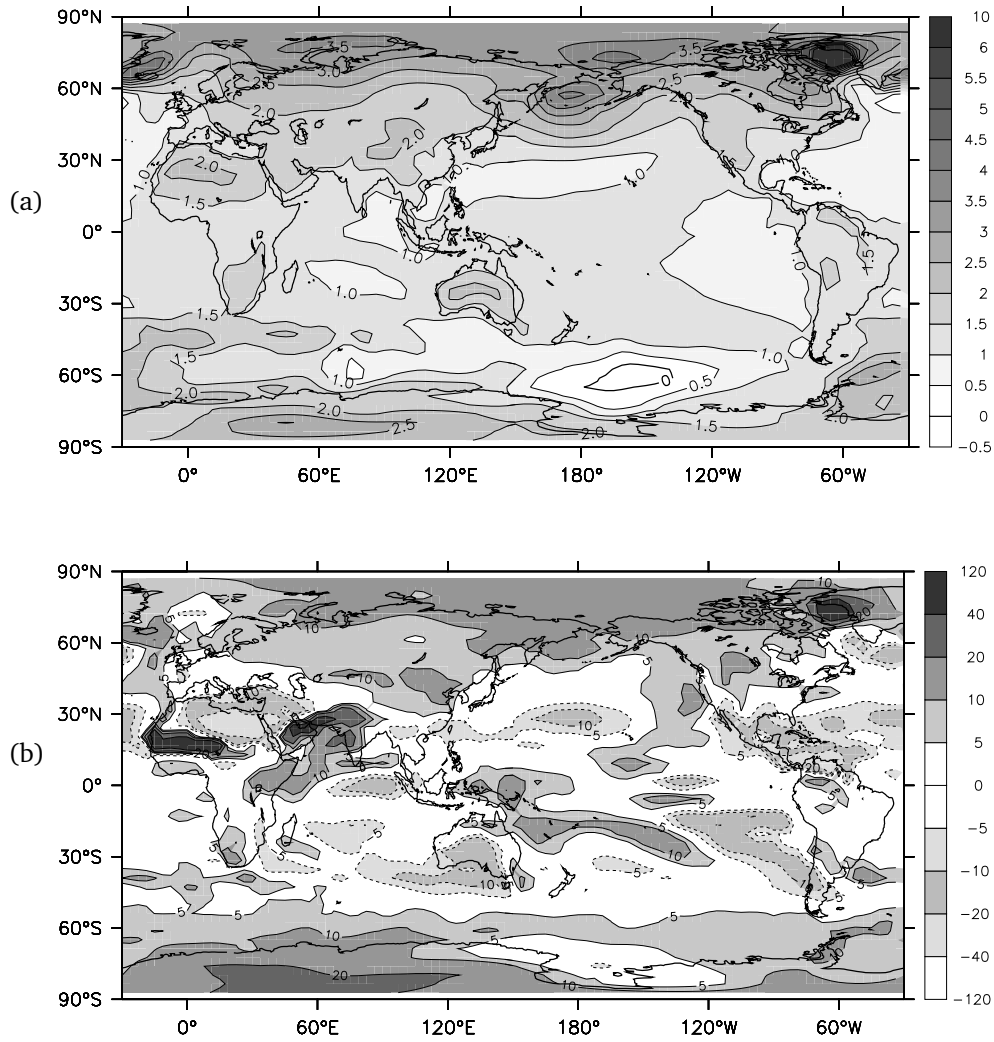


Figure 4.2: Difference of (a) mean surface temperature (K) and (b) mean precipitation (%) between the 30-year periods 2050–2080 and 1950–1980.

4.3. ENSO and Global Change

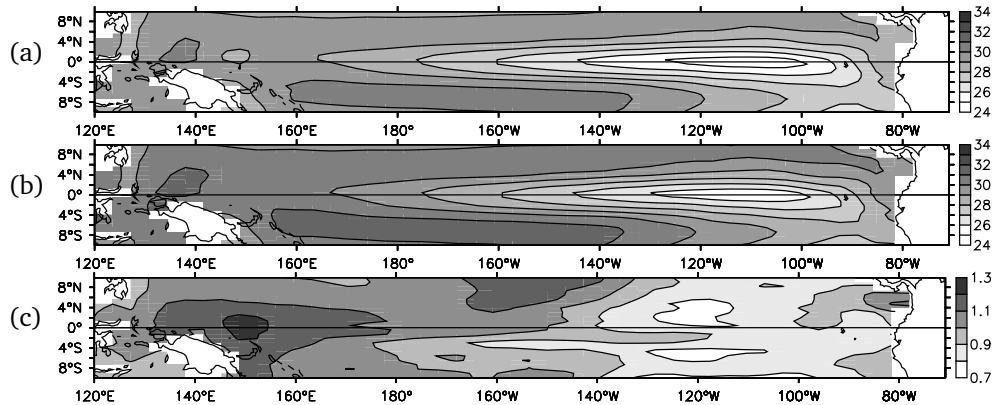


Figure 4.3: (a) 1950–1980 ensemble mean of the sea-surface temperature in the equatorial Pacific, (b) the same for the period 2050–2080 and (c) difference of (b) and (a).

of the 20°C isotherm Z_{20} and the sea-surface temperature SST. The domain used is 12°S–12°N, 120°E–80°W. Because the time mean state of the equatorial Pacific, the seasonal cycle and ENSO variability are strongly linked, we present the changes in each of them subsequently in the following paragraphs.

The ensemble mean sea-surface temperature averaged over the period 1950–1980 is shown in Fig. 4.3a. Although the overall features of the cold tongue warm pool agree reasonably well with observations, there are several deficiencies similar to those in the single simulation described by Otto-Bliesner and Brady (2001). The cold tongue extends too far to the west and the SST pattern is too symmetrical about the equator. The differences in SST between the periods 1950–1960 and 2050–2080 are shown in Fig. 4.3c. There is a nearly homogeneous warming of the tropical Pacific with a slight increase in the equatorial east-west temperature gradient as the western part warms about 0.2 K more than the eastern part.

The ensemble mean seasonal cycle of SST for the period 1950–1980 is shown in Fig. 4.4a. The semi-annual signal in the western Pacific and the annual signal in the eastern Pacific are simulated reasonably well. The timing of the maximum SST in spring is a bit too early but the westward propagation of SST anomalies is in accordance with observations. The differences in the seasonal cycle of SST between the periods 1950–1980 and 2050–2080 are shown in Fig. 4.4c. The figure confirms that the western Pacific is warming up more than the eastern Pacific, otherwise the warming is almost homogeneous.

As already mentioned in Otto-Bliesner and Brady (2001), the variability of the ENSO indices is slightly smaller than what is observed. For the first ensemble member, SST averaged over the Niño3.4 region is shown in the upper panel of Fig. 4.5 together with an estimate of the trend of the ensemble. The detrended Niño3.4 index with seasonal cycle removed is shown in the lower panel of Fig. 4.5. The amplitude is simulated reasonably well with a standard deviation of 0.77 ± 0.01 K, but there is more

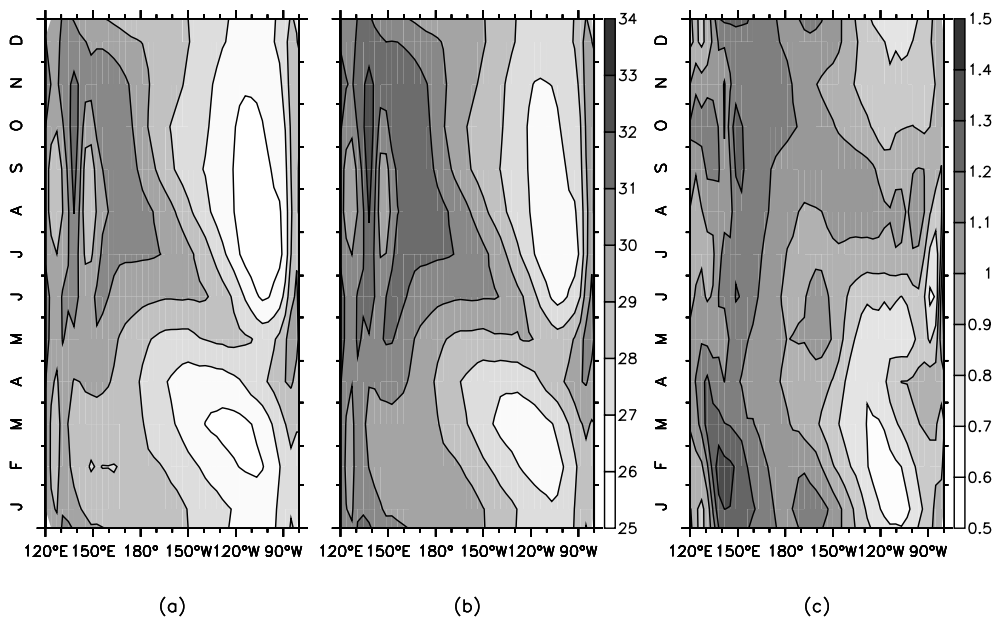


Figure 4.4: (a) 1950–1980 ensemble mean equatorial seasonal cycle of the sea-surface temperature in the Pacific, (b) the same for the period 2050–2080 and (c) difference of (b) and (a).

4.3. ENSO and Global Change

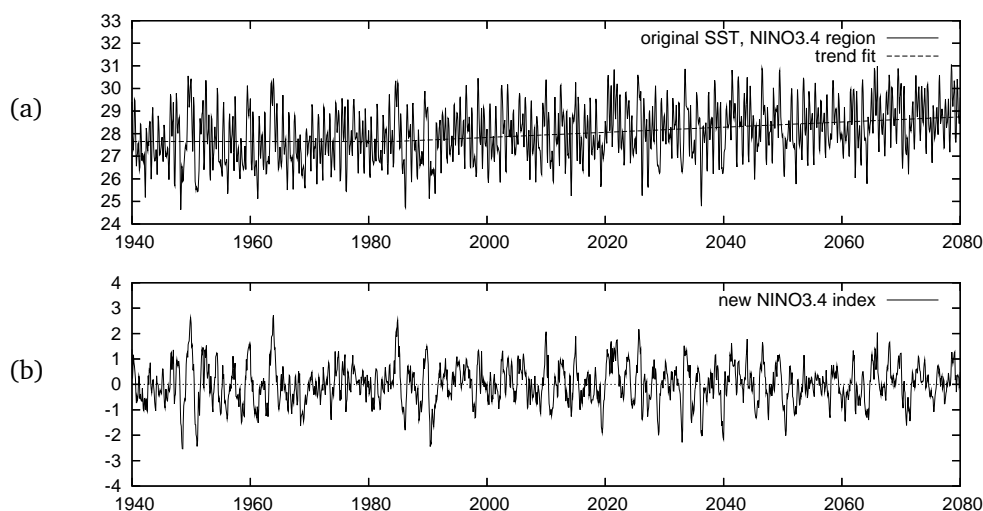


Figure 4.5: (a) SST values in the Niño3.4 region for ensemble member 1 of the CCSM, with an estimate of the ensemble trend. (b) The detrended Niño3.4 index for ensemble member 1, with seasonal cycle removed.

high frequency noise and the oscillation is more regular than the observed Niño3.4 index. The standard deviation was computed for the whole ensemble, but individual members show very similar results. The skewness of the detrended Niño3.4 index is -0.05 ± 0.02 compared to 0.40 ± 0.25 for the NCEP Niño3.4 index: ENSO is almost symmetrical in CCSM. The amplitude of thermocline variability in the Niño3.4 region is too small: 5.6 m compared to 13.0 ± 1.5 m for TAO/TRITON observations (McPhaden et al., 1998b). The amplitude of τ^x variability in the Niño4 region (160°E – 150°W , 5°S – 5°N) is also weaker than observed: $6.5 \cdot 10^{-3}$ Pa compared to $(14 \pm 1) \cdot 10^{-3}$ Pa in the TAO/TRITON observations.

A wavelet spectrum (based on a Morlet-6 transform) indicates that most of the energy is contained in the frequency band of 2.5–3.5 year. Weaker energy in this band occurs during the early and mid 1990's and between 2050 and 2060 (Fig. 4.6a). Spectra based on two thirty-year intervals, averaged over all ensemble members, indicate that the period of ENSO variability is around 2.8 year (Fig. 4.6b) for both periods. In each spectrum of the individual members, there appears to be no significant change in ENSO period and amplitude. Together with the results in Fig. 4.6, this strongly suggests that ENSO variability in this version of CCSM does not change under a moderate global warming.

The pattern of variability associated with ENSO can be determined through the first EOF of SST and is plotted in Fig. 4.7a for the 1950–1980 period. It broadly resembles the observed variability, again with deficiencies in the cold tongue region and the equatorial asymmetry. The EOF pattern hardly changes over the period 2050–2080 (Fig. 4.7b), confirming once more that the ENSO variability is only marginally

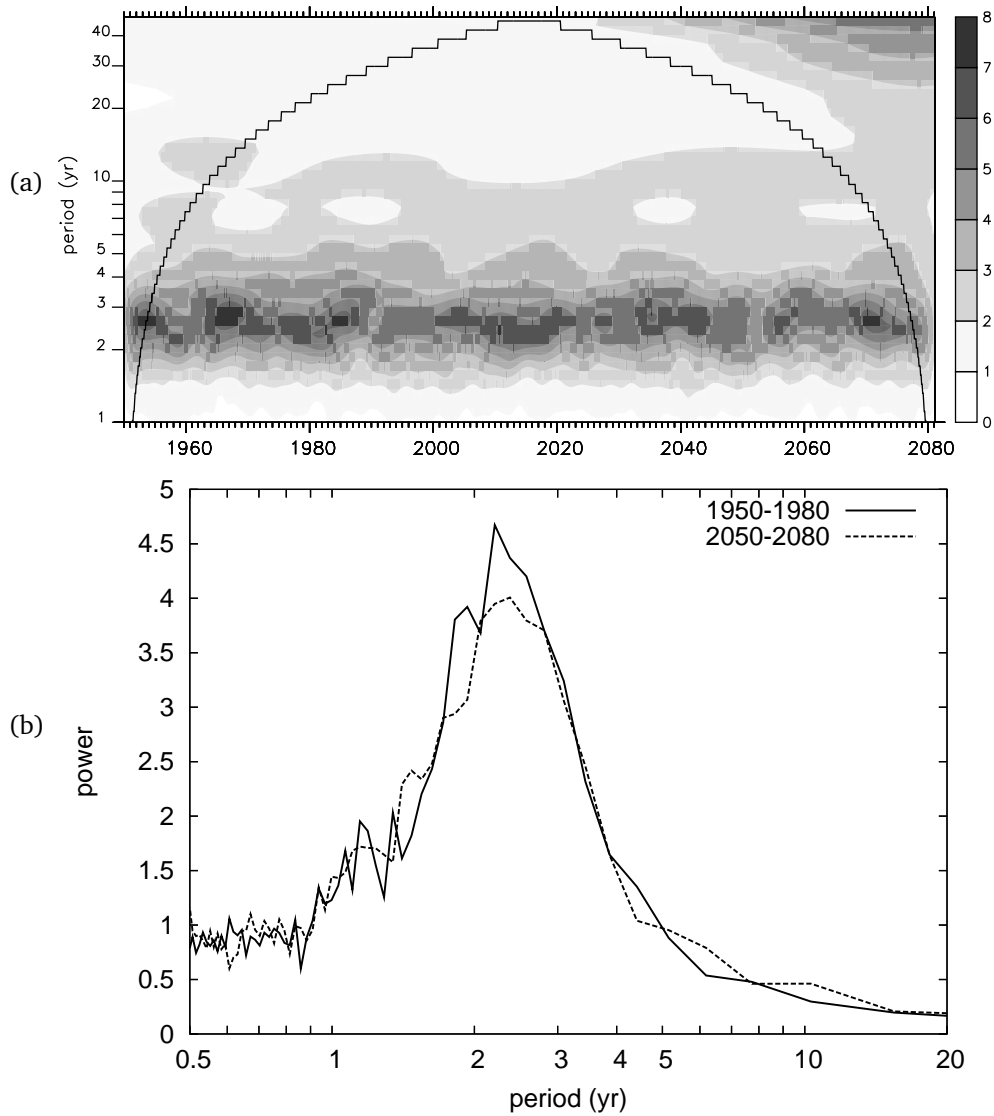


Figure 4.6: (a) Wavelet spectrum (Morlet-6) of the Niño3.4 index of the ensemble simulations. (b) Spectra of the Niño3.4 index for two thirty-year periods, averaged over all ensemble members.

4.4. Analysis

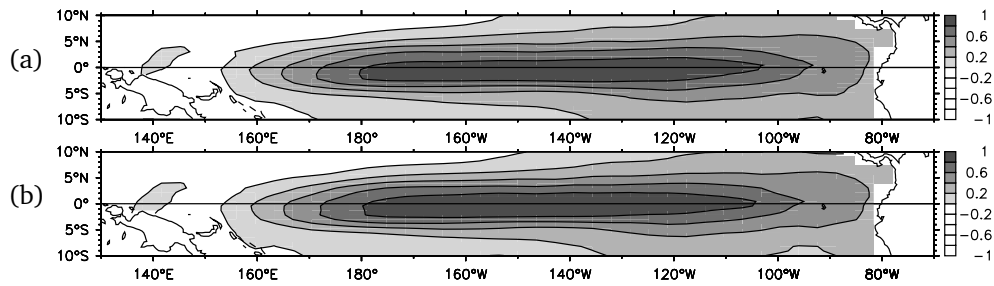


Figure 4.7: First EOF of SST of the ensemble of simulations. (a) Period 1950–1980 and (b) 2050–2080.

affected by the global temperature increase.

A simple conclusion from these results would be that ENSO does not change in a warmer climate. This is in agreement with most studies in state-of-the-art climate models (Collins and coauthors, 2005), such as those used in the IPCC TAR and summarized in Latif et al. (2001). However, there are a few suspicious features which motivate further analysis into the reasons why ENSO does not change in the CCSM simulations. Although the mean state cold-tongue/warm-pool configuration is reasonably simulated, the ENSO period in CCSM is smaller than that observed. Furthermore, the ENSO response is more regular than what is observed, suggesting that nonlinear dynamical effects as found in intermediate complexity coupled models (ICMs) are weaker (or even completely absent) in the CCSM results. Finally, as will be shown below, the equatorial wind response to SST has some deficiencies with respect to observations. In the next section, we will analyze and interpret the CCSM results through a comparison with results from ICMs.

4.4 Analysis

In this section, our main point is to demonstrate that the insensitivity of ENSO to global warming in the CCSM is due to deficiencies in the simulation of the equatorial zonal wind stress response. First we will show that the ENSO behavior in CCSM is likely to be that of a noise-driven stable system. Next, ICMs are used to demonstrate that an enhanced stability of the Pacific climate state and a shorter ENSO period can both be explained by a zonal wind stress field that is strongly confined in the meridional direction. An analysis of the CCSM results will show that the wind stress field is indeed too narrow around the equator, and that the wind response is independent of background SST.

4.4.1 Low-order chaos versus noise driven

In the theoretical framework on ENSO variability, a Hopf bifurcation marking the transition from a stable stationary time-mean state to a periodically varying state is of

central importance (Neelin et al., 1998). The transition from stable to unstable can, for example, be induced by varying the strength of coupled feedbacks in the equatorial Pacific, such as the amplitude of the wind anomaly per degree SST anomaly. The spatial and temporal pattern of the periodically varying state of ENSO can be estimated from observations, even if there are substantial secondary modes (Jiang et al., 1995).

Estimates from observations indicate that ENSO is close to neutral in reality (Fedorov and Philander, 2000; Dijkstra and Burgers, 2002) and, in addition, is quite irregular; this leaves two possibilities. The first possibility is that the Pacific climate state is linearly unstable, that the ENSO amplitude is determined by non-linear dynamics, and that chaotic dynamics cause its irregularity. In this case, ENSO is qualitatively a low-order chaotic system. The second possibility is that at the root of ENSO lies a linearly stable Pacific climate system, with atmospheric noise exciting finite-amplitude fluctuations inducing the irregularity of ENSO. In this case, ENSO is qualitatively a noise-driven stable system. Philander and Fedorov (2003) argue that the latter is most likely what occurs in nature. The term ‘noise’ refers to processes that have much smaller spatial and time scales than ENSO and evolve independently. The complete system (deterministic + noise) has many degrees of freedom.

We have investigated whether ENSO in the CCSM is a low-order chaotic system or not with the method of Tziperman et al. (1994), described in the Appendix. They showed, for example, that the Cane-Zebiak model (Zebiak and Cane, 1987) is a low-order chaotic system. The method estimates the dimension of the attractor from time series of a characteristic variable. The dimension is obtained from the slope of the cumulative distribution function $C_2(r)$ versus the distance between points r in a log-log plot. When the slopes for increasing embedding dimension M converge to a finite value, the attractor dimension is finite and a low-order chaotic system is causing the behavior (see the Appendix for details).

We compared the results for the period 1950-2080 of the CCSM ensemble, 8742 simulated years in total, with a simulation of the Cane-Zebiak model of the same length. As characteristic model variables we took values of the Niño3 index in the Cane-Zebiak model run and of the Niño3.4 index in the CCSM ensemble members, averaged over 3 month intervals. For the Cane-Zebiak model we see that the slopes in Fig. 4.8a slowly converge to an attractor dimension of around 5. This is in agreement with Tziperman et al. (1994) who obtained an estimate of 3.5 from embedding dimensions up to 14. For the CCSM simulations (Fig. 4.8b) there is no sign that the slopes converge and we can only establish a lower bound of about 40 for the attractor dimension.

We conclude that the Niño3.4 behavior in the CCSM simulations is qualitatively similar to that of a stable noise driven system, and does not show dynamics of a low-dimensional chaotic system.

4.4.2 Sensitivities in ICMs

To find the reason for the stability of the Pacific climatology on the one hand and the relatively small ENSO period on the other hand, sensitivity studies which have

4.4. Analysis

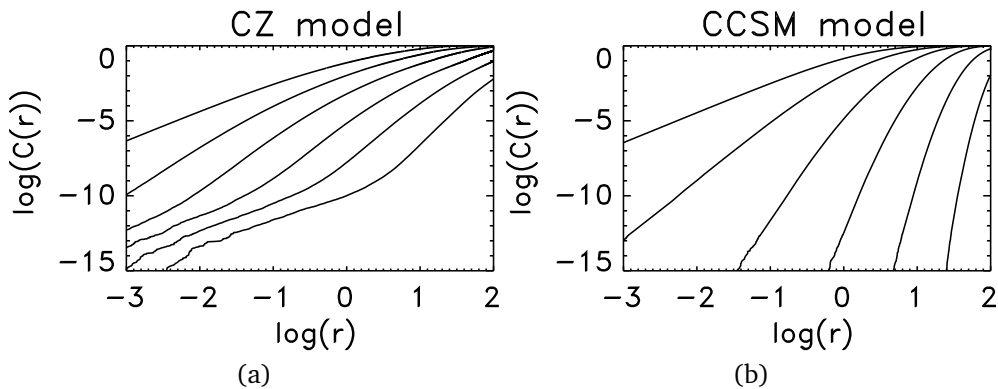


Figure 4.8: Estimates for the dimension of the attractor of a run of the Cane-Zebiak model (a) and the CCSM ensemble simulations (b). From left to right, curves are shown for embedding dimensions M of 2, 4, 8, 16, 32 and 64. The estimate equals the value of the slope of the straight section of the curves in the limit of high embedding dimension and run length. Because the run length is limited (8742 years for both Cane-Zebiak and CCSM), the lines are not straight anymore beyond an embedding dimension of around 30.

been done with ICMs are useful. One of the ICMs that have been used to study the stability of the Pacific climate system is the implicit pseudo-spectral model (IPSM) of van der Vaart et al. (2000). The IPSM is a pseudo-spectral model very similar to the Zebiak and Cane (1987) model in that it couples an ocean model consisting of a shallow water layer with an embedded mixed layer of fixed depth to a Gill (1980) atmosphere model.

Both the mean climate and the stability properties of this state change when parameters like the coupling strength μ are varied. Such parameters are therefore ideally suited for studying sensitivities of ENSO behavior to certain physical processes. For small μ , the steady climate states are stable but above critical values of μ , spontaneous oscillatory behavior appears through the destabilization of Pacific climatology to the ENSO mode. This transition can be shown to be a Hopf bifurcation and in van der Vaart et al. (2000), the position of the Hopf bifurcation and the period of the ENSO mode at criticality was determined over a broad range of parameter space.

One of the interesting results in van der Vaart et al. (2000) is replotted in Fig. 4.9. Here, the value of μ at the Hopf bifurcation, μ_c , as well as the period of the ENSO mode at criticality, P_c , are plotted versus the ratio of the oceanic and atmospheric Rossby deformation radii, α . As α increases, the meridional extent of the atmospheric wind-stress response decreases and becomes more localized near the equator. From Fig. 4.9a we see that with increasing α , the cold-tongue warm pool mean state stabilizes as the Hopf bifurcation shifts to larger values of μ . At the same time the period at criticality decreases, because the forced Rossby waves participating in the adjustment of the ocean do not include the high wavenumber slow modes further away from the equator (Kirtman, 1997).

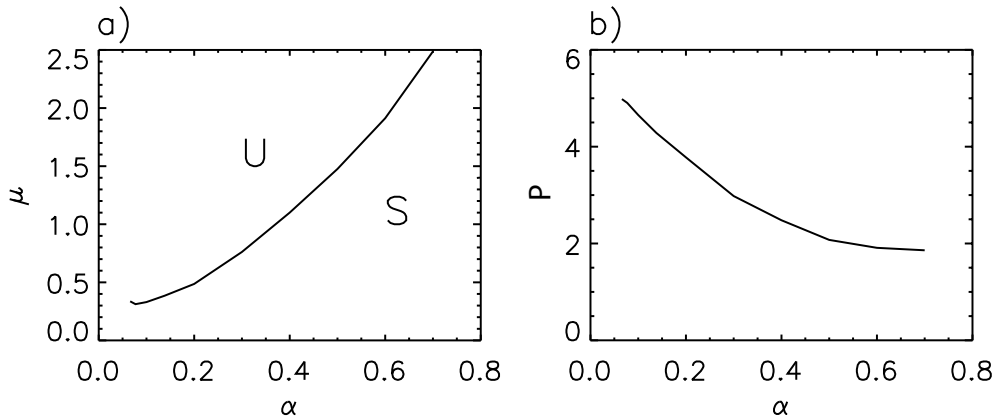


Figure 4.9: (a) The value of the critical ocean-atmosphere coupling strength μ_c at the Hopf-bifurcation as a function of α , the ratio between the oceanic and atmospheric Rossby radii. S (U) indicates regions of linear (un)stable climatology's. (b) The period P of the oscillation (in years) at the Hopf-bifurcation as a function of α .

Although only the dependence of the critical conditions on the meridional extent of the wind stress is considered, the results in Fig. 4.9 strongly motivate us to look further into the effects of the meridional pattern of zonal wind on the ENSO period and the stability of the Pacific climate state. To investigate this in more detail, we make use of a linear shallow water ocean model, the Gmodel as presented in Burgers et al. (2002), coupled to a Gill atmosphere model (Gill, 1980).

In the Gmodel, the reduced-gravity ocean model is forced by zonal and meridional wind stress, and has thermocline depth, zonal and meridional current as output variables; SST is computed only as a diagnostic variable. The Gmodel has been tuned to simulate the observed Niño3 and Niño4 indices well when forced with FSU pseudo wind stress fields (Stricherz et al., 1997). We have also adapted the parameters of the SST equation to represent the results of the CCSM ocean model; this gives essentially the same results. The atmosphere model responds only to the simulated SST field. The response to an SST spike (very narrow in the zonal direction) on the equator is computed with the Gill model (Gill, 1980). The full wind response is obtained by integrating along the equator and multiplying the local SST anomaly with this wind response pattern. The meridional scale of the wind response to SST anomalies can be adjusted with the parameter α , the ratio of the oceanic and atmospheric Rossby deformation radii.

To determine the relation between the ENSO period and the meridional extent of the zonal wind response, three Gmodel runs were performed with different values of α . For each run, the coupling strength μ was set just below the critical value μ_c . A Hovmüller diagram of SST is plotted for different values of α in Fig. 4.10. It is clear that the ENSO period decreases with increasing α (decreasing meridional extent): the period goes down from approximately 8 years to 21 months. The critical coupling

4.4. Analysis

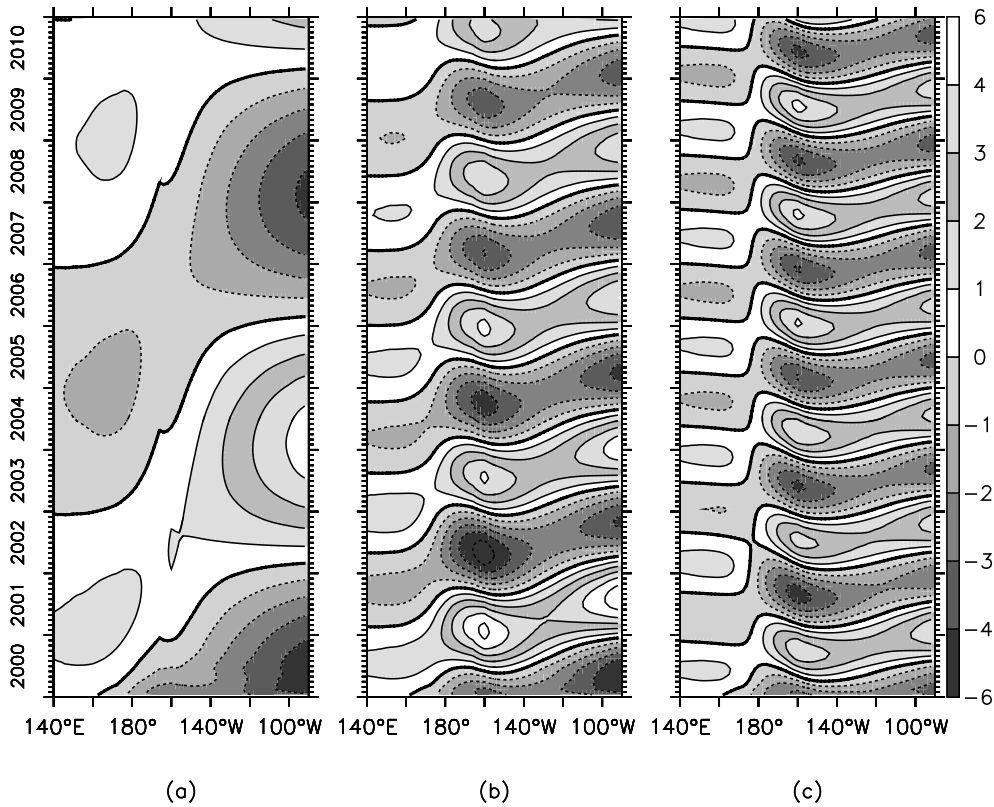


Figure 4.10: Hovmöller diagrams of SST anomalies computed with the Gmodel-Gill model for three different values of α : 0.15 (a), 0.22 (b), 0.3 (c). A larger value of α indicates a more equatorially confined zonal wind response. The ocean-atmosphere coupling strength was tuned to just below the critical value μ_c .

strength μ_c increases with increasing α , consistent with the results in Fig. 4.9a.

4.4.3 The wind response in CCSM

Given that the Pacific climate state in the CCSM appears very stable and the ENSO period is shorter than that observed, the results in the previous section motivate us to investigate the wind response to SST anomalies in the CCSM and to compare this response with observations and with results from the Gmodel.

The response of zonal wind to SST anomalies has been found by a straightforward linear regression (see for example the textbook of Von Storch and Zwiers (1999,2001), §8.3) on the monthly data: $\tau'_x(\mathbf{x}) = \int d\mathbf{x}' A(\mathbf{x}, \mathbf{x}') T'(\mathbf{x}')$ with τ'_x and T' surface fields of zonal wind anomalies and SST anomalies in the equatorial Pacific region, and the function A the response model. Because the model is under determined

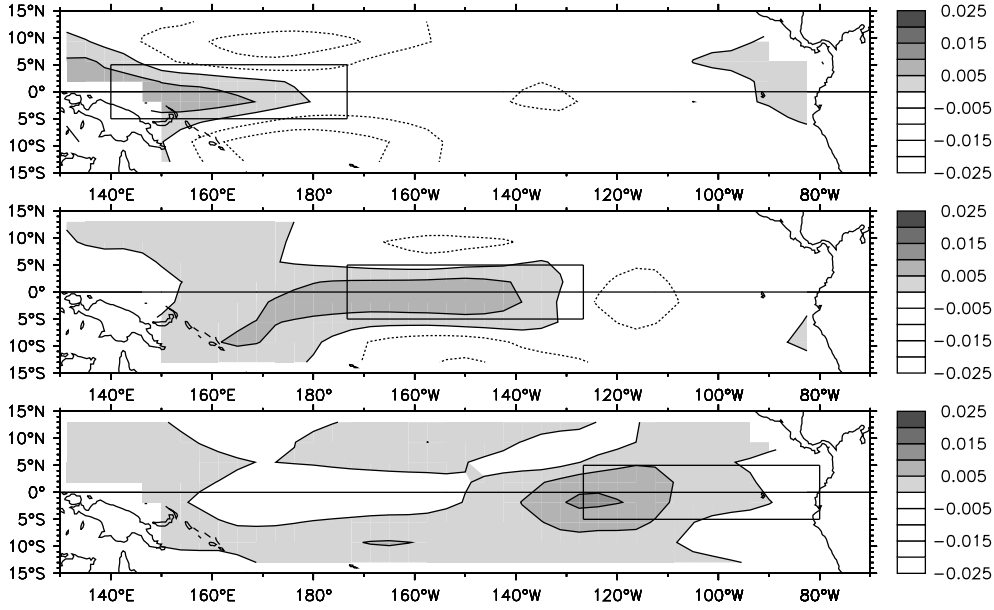


Figure 4.11: The zonal wind stress response of the CCSM to SST anomalies in boxes from 5°S–5°N and 140°E–173°W, 173°W–127°W, 127°W–80°W respectively. There is no significant difference between the periods 1950–1980 and 2050–2080.

even for the large ensemble considered, the dimension has to be reduced. This was achieved by averaging T' over boxes on the equator. The large amount of data from the CCSM simulations ($\sim 10^5$ months) allows up to eight boxes along the equator, but for a comparison with observational data we use only three. The meridional borders of the boxes are at 5°S and 5°N, zonally the boxes are equally divided between 140°E and 80°W.

We switch from x and x' to discrete indices k and ℓ , which gives

$$A_{k\ell} = \langle \tau'_x T' \rangle_{km} \langle T' T' \rangle_{m\ell}^{-1} \quad (4.1)$$

with $A_{k\ell} = A(\mathbf{x}_k, \mathbf{x}'_\ell)$, k an index enumerating τ_x grid points, ℓ an index enumerating the T boxes along the equator and $\langle \dots \rangle$ indicating a time average. The zonal wind response to SST anomalies in the three boxes is shown in Fig. 4.11. The difference between periods 1950–1980 and 2050–2080 is negligible. The same wind response patterns as determined from the ERA-40 dataset are presented in Fig. 4.12. Compared to observations, the zonal and meridional extent of the wind response in CCSM is almost a factor two smaller. When we use the meridional extent of the CCSM wind response pattern in the Gmodel (Fig. 4.13) we find an ENSO period of approximately 2.5 years, comparable to the ENSO period found in the CCSM.

In the CCSM, the wind response to SST anomalies on the edge of the warm pool is not stronger than the response in the middle of the cold tongue; this is contrary to

4.4. Analysis

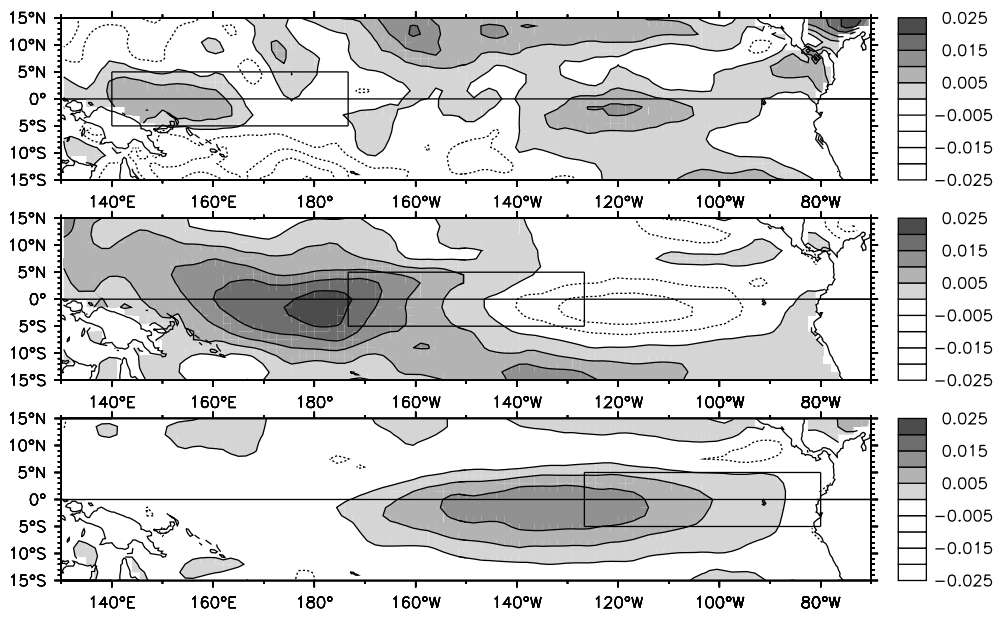


Figure 4.12: The zonal wind stress response of the ERA-40 reanalysis (observations) to SST anomalies in boxes from 5°S–5°N and 140°E–173°W, 173°W–127°W, 127°W–80°W respectively.

Chapter 4. El Niño and greenhouse warming

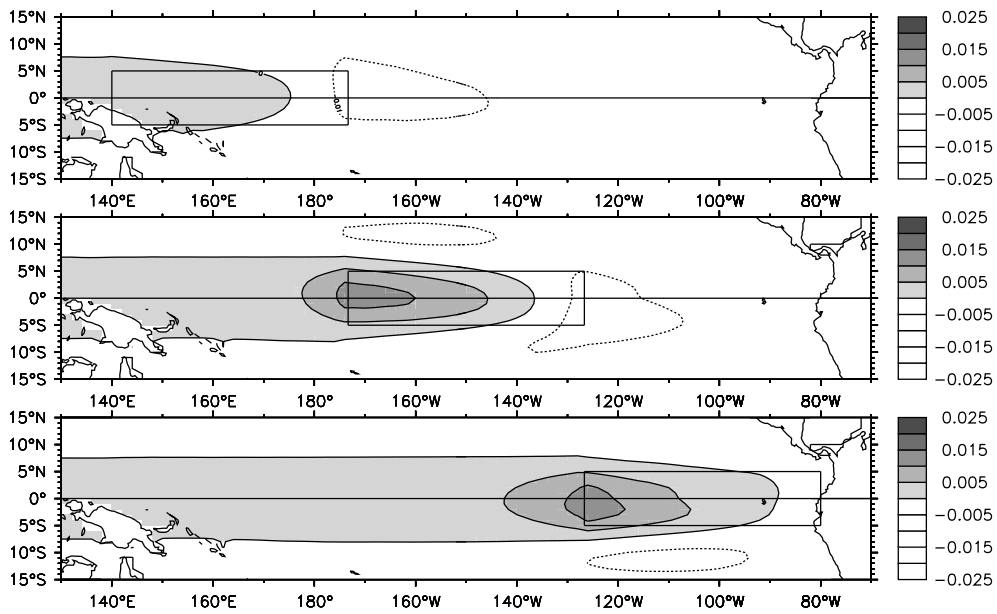


Figure 4.13: The zonal wind stress response of the linear Gmodel to SST anomalies in boxes from 5°S–5°N and 140°E–173°W, 173°W–127°W, 127°W–80°W respectively. The meridional scale of the wind response was adjusted to match the response of the CCSM in figure 4.11.

4.5. Summary and Discussion

observations and other models. Also, the westerly wind response to an SST anomaly extends too far east across the SST anomaly. In observations and other models, the zero contour of the zonal wind response is approximately centered above the SST anomaly. The latter two features are linked. Normally, atmospheric heating occurs somewhat west of the SST anomaly due to the climatological zonal SST gradient and the zonal wind response extends east of the heating region (Clarke, 1994). These offsets compensate each other. In CCSM the dependence on background SST is missing. Therefore atmospheric heating occurs centered above the SST anomaly and the wind response is shifted eastwards compared to observations. The insensitivity of the wind response in CCSM to background SST is consistent with the fact that there is no change in the wind response due to global warming.

4.5 Summary and Discussion

Results from a 62 ensemble member simulation with the NCAR-CCSM version 1.4 were used to investigate the changes in ENSO behavior due to the increase of atmospheric greenhouse gases. Under a global climate change of 1.2 K from 2000–2080, the model ENSO variability does not change significantly in each of the ensemble members. The mean equatorial zonal temperature gradient increases slightly but the ENSO period, amplitude and pattern are basically unchanged.

One could argue that the warming signal is not strong enough and that larger anomalies are needed to obtain a significant change. Indeed, simulations under $6 \times \text{CO}_2$ conditions have shown a significant change in the ENSO response (Otto-Bliesner and Brady, 2001). On the other hand, in ICMs which represent both the time-mean state and the ENSO delayed oscillator mode quite well, both period and amplitude do change when the radiative equilibrium temperature is increased by only 1 K. One possibility is that these ICMs miss some important physics which influences their response to global warming. Another option is that the coupled feedbacks involved in ENSO are not represented well in the CCSM. We have investigated possible flaws of the CCSM and their effects on the response to global warming.

The insensitivity of ENSO in the CCSM to changes in background temperature suggests that the Pacific climate system is stable. This has been confirmed with an analysis of the attractor dimension of the model which indicates that the model behavior is qualitatively similar to that of a stable system driven by stochastic noise. We have shown that the zonal wind response to SST anomalies in the equatorial Pacific is insensitive to changes in background SST due to the zonal SST gradient, which suggests that the wind response is also insensitive to global warming. The zonal wind response is weaker than in observations and the pattern is too narrow around the equator. These results are robust, due to the large amount of data available from the ensemble for statistical analysis.

Using the linear Gmodel, it was shown that the short ENSO period of the CCSM is related to its narrow zonal wind response pattern around the equator. If the wind response becomes wider, as in the observations, the period will increase. Also, the narrow wind response pattern results in a more stable system compared to a wider

Chapter 4. El Niño and greenhouse warming

wind response pattern, consistent with the results from van der Vaart et al. (2000) shown in Fig. 4.9. A more stable ENSO system is less sensitive to changes in the background state than an unstable system.

In conclusion, while the ensemble results may lead one to believe that no significant changes in ENSO are to be expected in the near future, our analysis shows that the insensitivity of ENSO in CCSM to global warming may be largely due to model errors. This indicates that it is necessary to analyze GCMs with respect to these deficiencies and improve them. Only then can the models be used with some confidence to answer the questions whether and how ENSO will change due to global warming.

Appendix: Determination of the dimension of an attractor

The pseudo-state space of dimension M of a generic trajectory of a dynamical system variable $x(t)$ is the space of vectors

$$y(t) = \{x(t), x(t - \Delta), x(t - 2\Delta), \dots, x(t - (M - 1)\Delta)\},$$

where Δ is the so-called delay. The behavior of the vectors $y(t)$ is related to the dynamics of the underlying dynamical system, as discussed e.g. in the textbook of Nayfeh and Balachandran (1995).

The dimension d of the attractor in pseudo-state phase can be estimated from a long sequence

$$y(t_0), y(t_0 + \Delta), y(t_0 + 2\Delta), \dots, (t_0 + N\Delta) \quad (N \gg M),$$

as follows. First one calculates the cumulative distribution function $C_2(r)$ of distances r between points in the sequence. $C_2(r)$ is obtained from calculating the distances $r(y(t_0 + i\Delta), y(t_0 + j\Delta))$ for all possible pairs (i, j) , and sorting the pairs according to these distances. Instead of a single long sequence, one can also use multiple sequences. This has been done for the ensemble of CCSM simulations. Next one estimates d from the relation

$$C_2(r) \sim r^d$$

that holds for distances r that are sufficiently small that only local properties of the attractor play a role. E.g. if the dimension of the attractor is 2, then around a point on the attractor, on the average 4 times as many attractor points lie within a distance $2r$ as within a distance r . For finite sequences, the above relationship will break down for very small distances where the sampling of the attractor is not adequate. By plotting $C_2(r)$ versus r in a double logarithmic plot, d can be estimated conveniently from the slope of the straight section of the curve. The dimension d will generally depend on the embedding dimension M . The amount of data $x(t)$ limits the maximum value of M for which one can make estimates of d . If the dimension of the attractor of the underlying dynamical system is d_s , one has $d = d_s$ for M above some threshold. A sufficient condition for $d = d_s$ is that $M \geq 2d_s + 1$.

Chapter 4. El Niño and greenhouse warming

Chapter 5

Discussion

The aim of this thesis is to improve our understanding of El Niño, by using recently available observational datasets to analyze and verify mechanisms that drive El Niño. A secondary goal is to improve model simulations of El Niño, which can lead to improved forecasts. This is a slow process; like in numerical weather prediction, models used for ENSO forecasting have improved slowly but surely.

Chapter 2 gives an analysis of how changes in SST are related to thermocline depth variability. There is a time delay between a local thermocline depth anomaly and the resulting SST anomaly at the surface. This time delay is important as it partially determines the period of ENSO. It is shown that the delay varies with longitude, from approximately 12 months around the dateline to two weeks in the eastern equatorial Pacific. Two important pathways are distinguished that cause the relation between thermocline depth and SST: the ‘upwelling pathway’ and the ‘wind coupling pathway’. In the upwelling pathway temperature anomalies at the thermocline are transported to the surface by a combination of upwelling and vertical mixing. The wind coupling pathway starts with a thermocline depth anomaly in the central Pacific which travels east as a set of Kelvin waves, causing SST anomalies in the eastern Pacific. These SST anomalies induce zonal wind anomalies in the central Pacific. Positive SST anomalies are generated by reduced anomalous upwelling, reduced evaporation and through anomalous eastward advection across the edge of the warm pool. The upwelling pathway is found to be the dominant link between thermocline depth and SST anomalies in the eastern Pacific, approximately east of 140°W. West of 140°W where the delay is longer, the wind coupling pathway is dominant.

Chapter 3 analyzes the mechanisms that are important for the development of SST anomalies in the western equatorial Pacific, the warm pool region. This is one of the few topics in ENSO research where there is no consensus over which mechanisms are the most important, although there is agreement that surface fluxes play an important role. Mechanisms that generate SST anomalies in the warm pool region are shown to be mostly wind driven in chapter 2. In a budget study it is shown how SST anomalies propagate zonally from the western Pacific to the central/eastern Pacific and back during the development and decay of an El Niño event. An analysis of the

mixed layer heat budget in an ocean model simulation shows that not just zonal wind anomalies (causing anomalous upwelling and zonal advection) but also wind speed anomalies (generating anomalous latent heat flux and changes in mixed layer depth) are important. Changes in mixed layer depth are an important factor by influencing the balance between the mean terms in the SST equation, resulting in warming (reduced mixed layer depth) or cooling (increased mixed layer depth) of the surface layer. Eastward propagation of SST anomalies during the growth phase of El Niño is caused partially by a reduction of the mixed layer depth east of the SST anomaly, and partially by zonal advection. Westward propagation during the decay phase is caused by warming in the western Pacific through mean zonal advection across an anomalous temperature gradient, and radiative cooling east of the SST anomaly.

The theme of chapter 4 is the question “How does El Niño change under the influence of human induced global warming?”. An analysis of 62 coupled ocean-atmosphere model simulations over the period 1940–2080 shows no significant changes in ENSO characteristics, despite a simulated global average warming of $\sim 1.2\text{K}$. A detailed investigation is performed to find out if flaws in the model used for the simulation are responsible for the insensitivity of El Niño to global warming. Analyzing the attractor dimension of the model indicates that the model behavior is qualitatively similar to that of a stable system driven by stochastic noise. The zonal wind response to SST anomalies in the equatorial Pacific is shown to be insensitive to changes in background SST. The zonal wind response pattern is too narrow around the equator, this is shown to lead to a more stable system, insensitive to changes in background temperature. Concluding, model deficiencies make the model insensitive to global warming. It is necessary to analyze and improve coupled general circulation models with respect to these deficiencies before they can be used answer the questions whether and how ENSO will change due to global warming.

There are several limitations to this study. The main goal is to contribute to a better representation of important processes to eventually improve El Niño simulations and forecasts, rather than to better understand general properties of El Niño. The (ocean) models used in this study are only approximations of the real world, resulting in differences between model output and observations. Especially the representation of the mixed layer dynamics is often rather crude. In chapters 2 and 3 we make use of a forced ocean model to simulate El Niño events of the past decades, so coupled processes have not been studied explicitly. In chapter 2 the effect of the seasonal cycle on the lagged relation between thermocline depth anomalies and SST anomalies has not been investigated. The analyses in chapters 2 and 3 consider what happens on the equator, and not what happens in near-equatorial regions. One of the conclusions of chapter 4 is that model deficiencies significantly reduce the sensitivity of the simulated El Niño–Southern Oscillation to changes in background temperature. Repeating the ensemble simulation with a model that has a better representation of El Niño, preferably with a higher resolution in the atmosphere component, is not an easy task. It would however increase the reliability of the results, and could provide insight in what changes in ENSO characteristics we can expect as the earth warms by the greenhouse effect. Plans to perform such a simulation in the near future are currently being worked on.

Apart from improved understanding of ENSO mechanisms, the work in this thesis results in three recommendations for verification and possible improvement of (coupled) ocean-atmosphere model simulations. The analysis of the time delay between SST and thermocline depth anomalies in chapter 2 shows that a general circulation model performs significantly better than a linear model, but nevertheless does not represent the time delay satisfactorily. The ocean model used in chapter 3 performs approximately the same, suggesting that more ocean models may be affected by this problem. The time delay analysis is recommended as a useful test of the balance between upwelling and wind driven mechanisms in the development of SST anomalies along the equator. If the balance between upwelling and wind-related mechanisms as well as the time delay between thermocline depth and SST anomalies is improved in model simulations, improvement can also be expected in the simulated ENSO period, the balance between SST anomaly development in the eastern and western Pacific during El Niño, and possibly in the simulation of El Niño along the coast of south America.

Chapter 3 shows the impact of the mixed layer depth on the development of SST anomalies in the western and central equatorial Pacific. A comparison of the simulated mixed layer depth with observations is recommended as a test for ocean models when the development of SST anomalies is of interest. If an improvement in the simulated mixed layer depth can be achieved, the simulation of the initial development of El Niño with relatively weak SST anomalies in the western/central Pacific can be expected to improve.

In chapter 4 model deficiencies were found to be responsible for the insensitivity of a coupled general circulation model to global warming. A too narrow meridional extension of the zonal wind response pattern contributes to a too ENSO, with a too short period. Because a too short ENSO period is a common deficiency in coupled general circulation models, a test of the meridional extension of the zonal wind stress response is recommended. Further research is required to find out what causes the wind stress response to be too narrow in coupled ocean-atmosphere models; a recent study (Guilyardi et al., 2004) indicates the problem may be solved with a higher model resolution.

One of the goals of this study is to eventually improve El Niño forecasts. Ideally, the formulated recommendations should be applied to a model, and a forecast with the new version should be compared to an old forecast to see if improvement occurs. This has not been done so far, mainly because improving models is a time consuming and difficult task. Tests and comparisons of coupled models simulating El Niño have been performed before, in studies such as the El Niño Simulation Intercomparison Project (ENSIP; Latif et al., 2001). For example, in ENSIP a test similar to the one in chapter 2 (the lagged correlation of thermocline depth and the Niño3 index) is performed on the output of many coupled ocean atmosphere models. The tests presented in this thesis provide additional information, at a more detailed level. They could be used in model intercomparison projects that are organized in the framework of the international Climate Variability and Predictability (CLIVAR) Programme. In a follow-up project on the work in this thesis, the ECMWF System-2 model and available models from the IPCC Fourth Assessment Report will be subjected to these

Chapter 5. Discussion

tests.

The recommendations made in this study can contribute to the development of better models for simulating El Niño–Southern Oscillation, and eventually to more accurate ENSO forecasts. General circulation models have already improved significantly, outperforming simpler models that cannot represent all the important features of the tropical Pacific ocean. The future of ENSO forecasts lies in further improvement of these complex models.

Bibliography

- Allan, R. J., N. Nicholls, P. D. Jones, and I. J. Butterworth, 1991: A further extension of the Tahiti-Darwin SOI, early SOI results and Darwin pressure. *J. Climate*, **4**, 743–749, the series can be found at <http://www.cru.uea.ac.uk/cru/data/soi.htm>.
- Ammann, C. M., J. T. Kiehl, C. S. Zender, B. L. Otto-Bliesner, and R. S. Bradley, 2004: Coupled simulations of the 20th century including external forcing. *J. Climate*, in press.
- An, S.-I., F.-F. Jin, and I.-S. Kang, 1999: The role of zonal advection feedback in phase transition and growth of ENSO in the Cane-Zebiak model. *J. Meteor. Soc. Japan*, **77**, 1151–1160.
- Battisti, D. S. and A. C. Hirst, 1989: Interannual variability in a tropical atmosphere-ocean model: Influence of the basic state, ocean geometry, and nonlinearity. *J. Atmos. Sci.*, **46**, 1687–1712.
- Berlage, H. P., 1957: *Fluctuations of the general atmospheric circulation of more than one year, their nature and prognostic value*. Number 69 in Mededelingen en verhandelingen, KNMI, De Bilt, Netherlands.
- Bjerknes, J., 1966: A possible response of the atmospheric Hadley circulation to equatorial anomalies of ocean temperature. *Tellus*, **18**, 820–829.
- 1969: Atmospheric teleconnections from the equatorial Pacific. *Mon. Wea. Rev.*, **97**, 163–172.
- Bleck, R. et al., 1992: Salinity-driven thermocline transients in a wind- and thermohaline-forced isopycnic coordinate model of the north Atlantic. *J. Phys. Oceanogr.*, **22**, 1486–1505.
- Boville, B. A., J. T. Kiehl, P. J. Rasch, and F. O. Bryan, 2001: Improvements to the NCAR CSM-1 for transient climate simulations. *J. Climate*, **14**, 164–179.
- Burgers, G., M. A. Balmaseda, F. C. Vossepoel, G. J. van Oldenborgh, and P. J. van Leeuwen, 2002: Balanced ocean-data assimilation near the equator. *J. Phys. Oceanogr.*, **32**, 2509–2519.

Bibliography

- Burgers, G. and D. B. Stephenson, 1999: The normality of El Niño. *Geophys. Res. Lett.*, **26**, 1027–1030.
- Burgers, G. and G. J. van Oldenborgh, 2003: On the impact of local feedbacks in the central Pacific on the ENSO cycle. *J. Climate*, **16**, 2396–2407.
- Chen, D., M. A. Cane, A. Kaplan, S. E. Zebiak, and D. Huang, 2004: Predictability of El Niño over the past 148 years. *Nature*, **428**, 733–736.
- Clarke, A. J., 1994: Why are surface equatorial ENSO winds anomalously westerly under anomalous large-scale convection? *J. Climate*, **7**, 1623–1627.
- Collins, M., 2000: Understanding uncertainties in the response of ENSO to greenhouse warming. *Geophys. Res. Lett.*, **27**, 3509–3512.
- Collins, M. and coauthors, 2005: El Niño- or La Niña-like climate change? *Climate Dyn.*, to appear.
- Dai, A., T. M. L. Wigley, B. A. Boville, J. T. Kiehl, and L. E. Buja, 2001: Climates of the twentieth and twenty-first centuries simulated by the NCAR climate system model. *J. Climate*, **14**, 485–519.
- de Boyer Montégut, C., G. Madec, A. S. Fischer, A. Lazar, and D. Iudicone, 2004: Mixed layer depth over the global ocean: an examination of profile data and a profile-based climatology. *J. Geophys. Res.*, in press.
- Dijkstra, H. A. and G. Burgers, 2002: Fluid dynamics of El Niño variability. *Annu. Rev. Fluid Mech.*, **34**, 531–558.
- Doberitz, R., 1968: Cross-spectrum analyses of rainfall and sea temperature at the equatorial Pacific ocean. *Bonner Met. Abh.*, 1–61.
- Fedorov, A. and S. Philander, 2000: Is El Niño changing? *Science*, **288**, 1997–2002.
- Fedorov, A. V. and G. S. Philander, 2001: A stability analysis of tropical ocean-atmosphere interactions: Bridging measurements and theory for El Niño. *J. Climate*, **14**, 3086–3101.
- Fu, C., H. F. Diaz, and J. O. Fletcher, 1986: Characteristics of the response of sea surface temperature in the central Pacific associated with warm episodes of the Southern Oscillation. *Mon. Wea. Rev.*, **114**, 1716–1738.
- Galanti, E. and E. Tziperman, 2002: The equatorial thermocline outcropping — a seasonal control on the tropical Pacific ocean-atmosphere instability strength. *J. Climate*, **15**, 2721–2739.
- Gill, A. E., 1980: Some simple solutions for heat induced tropical circulation. *Quart. J. Roy. Meteor. Soc.*, **106**, 447–462.
- 1982: *Atmosphere–Ocean Dynamics*. Academic Press, 662 pp.

Bibliography

- Guilyardi, E., S. Gualdi, J. Slingo, A. Navarra, P. Delecluse, J. Cole, G. Madec, M. Roberts, M. Latif, and L. Terray, 2004: Representing El Niño in coupled ocean-atmosphere GCMs: The dominant role of the atmosphere component. *J. Climate*, **17**, 4623–4629.
- Harrison, D. and G. A. Vecchi, 2001: El Niño and La Niña — Equatorial Pacific thermocline depth and sea surface temperature anomalies, 1986 – 98. *Geophys. Res. Lett.*, **28**, 1051–1054.
- Hildebrandsson, H. H., 1897: Quelques recherches sur les centres d'action de l'atmosphère I. *Kongl. Sven. Vet. Akad. Handlingar*, **29**.
- Huber, M. and R. Caballero, 2003: Eocene El Niño: Evidence for robust tropical dynamics in the “Hothouse”. *Science*, **299**, 877–881.
- Ichiye, T. and J. Petersen, 1963: The anomalous rainfall of the 1957–58 winter in the equatorial central Pacific arid area. *J. Meteor. Soc. Japan*, **41**, 171–182.
- IPCC, 2001: *Climate Change 2001: The Scientific Basis. Contribution of Working Group I to the Third Assessment Report of the Intergovernmental Panel on Climate Change (IPCC) [Houghton, J.T., Y. Ding, D.J. Griggs, M. Noguer, P.J. van der Linden, X. Dai, K. Maskell and C.A. Johnson (eds)]*. Cambridge University Press, Cambridge, UK and New York, NY, 881 pp., also available from www.ipcc.ch.
- Jiang, N., J. D. Neelin, and M. Ghil, 1995: Quasi-quadrennial and quasi-biennial variability in the equatorial Pacific. *Clim. Dyn.*, **12**, 101–112.
- Jin, F-F, 1997: An equatorial recharge paradigm for ENSO. Part I: Conceptual model. *J. Atmos. Sci.*, **54**, 811–829.
- Jin, F-F and S.-I. An, 1999: Thermocline and zonal advective feedbacks within the equatorial ocean recharge oscillator model for ENSO. *Geophys. Res. Lett.*, **26**, 2989–2992.
- Jin, F-F, S.-I. An, A. Timmermann, and J. Zhao, 2003: Strong El Niño events and nonlinear dynamical heating. *Geophys. Res. Lett.*, **30**, 1120, doi:10.1029/2002GL016356.
- Johnson, G. C., M. J. McPhaden, and E. Firing, 2001: Equatorial Pacific ocean horizontal velocity, divergence, and upwelling. *J. Phys. Oceanogr.*, **31**, 839–849.
- Jones, P. D., T. J. Osborn, K. R. Briffa, C. K. Folland, E. B. Horton, L. V. Alexander, D. E. Parker, and N. A. Rayner, 2001: Adjusting for sampling density in grid box land and ocean surface temperature time series. *J. Geophys. Res.*, **106**, 3371–3380, data are available from <http://www.cru.uea.ac.uk/cru/data/temperature>.
- Kang, I.-S., S.-I. An, and F-F Jin, 2001: A systematic approximation of the SST anomaly equation for ENSO. *J. Meteor. Soc. Japan*, **79**, 1–10.

Bibliography

- Kaplan, A., M. A. Cane, Y. Kushnir, A. C. Clement, M. B. Blumenthal, and B. Rajagopalan, 1998: Analyses of global sea surface temperature 1856–1991. *J. Geophys. Res.*, **103**, 18567–18589, data are available from <http://ingrid.ldgo.columbia.edu>.
- Kessler, W. S., 2002: Is ENSO a cycle or a series of events? *Geophys. Res. Lett.*, **29**, 2125–2128, doi:10.1029/2002GL015924.
- Kiladis, G. N. and H. F. Diaz, 1989: Global climatic anomalies associated with extremes in the Southern Oscillation. *J. Climate*, **2**, 1069–1090.
- Kirtman, B. P., 1997: Oceanic Rossby wave dynamics and the ENSO period in a coupled model. *J. Climate*, **10**, 1690–1704.
- Kleeman, R., 1993: On the dependence of hindcast skill on ocean thermodynamics in a coupled ocean-atmosphere model. *J. Climate*, **6**, 2012–2033.
- Knutson, T. R., S. Manabe, and D. Gu, 1997: Simulated ENSO in a global coupled ocean-atmosphere model: Multidecadal amplitude modulation and CO₂ sensitivity. *J. Climate*, **10**, 131–161.
- Kraus, E. B. and J. S. Turner, 1967: A one-dimensional model of the seasonal thermocline II. the general theory and its consequences. *Tellus*, **19**, 98–105.
- Latif, M., 1987: Tropical ocean circulation experiments. *J. Phys. Oceanogr.*, **17**, 246–263.
- Latif, M., K. Sperber, J. Arblaster, P. Braconnot, D. Chen, A. Colman, U. Cubasch, C. Cooper, P. Delecluse, D. De Witt, L. Fairhead, G. Flato, T. Hogan, M. Ji, M. Kimoto, A. Kitoh, T. Knutson, H. Le Treut, T. Li, S. Manabe, O. Marti, C. Mechoso, G. Meehl, S. Power, E. Roeckner, J. Sirven, L. Terray, A. Vintzileos, R. Voß, B. Wang, W. Washington, I. Yoshikawa, J. Yu, and S. Zebiak, 2001: ENSIP: The El Niño Simulation Intercomparison Project. *Climate Dyn.*, **18**, 255–276.
- Madden, R. A. and P. R. Julian, 1971: Detection of a 40–50 day oscillation in the zonal wind in the tropical Pacific. *J. Atmos. Sci.*, **28**, 702–708.
- Matsuno, T., 1966: Quasi-geostrophic motions in the equatorial area. *J. Meteor. Soc. Japan*, **44**, 25–43.
- McPhaden, M. J., 1999: Genesis and evolution of the 1997-98 El Niño. *Science*, **283**, 950–954.
- McPhaden, M. J., A. J. Busalacchi, R. Cheney, J. R. Donguy, K. S. Gage, D. Halpern, M. Ji, P. Julian, G. Meyers, G. T. Mitchum, P. P. Niiler, J. Picaut, R. W. Reynolds, N. Smith, and K. Takeuchi, 1998a: The Tropical Ocean Global Atmosphere (TOGA) observing system: A decade of progress. *J. Geophys. Res.*, **103**, 14169–14240.

Bibliography

- 1998b: The Tropical Ocean Global Atmosphere (TOGA) observing system: A decade of progress. McPhaden et al. (1998a), 14169–14240, 14169–14240, appendix B1.
- Nayfeh, A. H. and B. Balachandran, 1995: *Applied Nonlinear Dynamics*. John Wiley, New York, U.S.A.
- Neelin, J. D., 1991: The slow sea-surface temperature mode and the fast-wave limit: Analytic theory for tropical interannual oscillations and experiments in a hybrid coupled model. *J. Atmos. Sci.*, **48**, 584–606.
- Neelin, J. D., D. S. Battisti, A. C. Hirst, F-F Jin, Y. Wakata, T. Yamagata, and S. Zebiak, 1998: ENSO theory. *J. Geophys. Res.*, **103**, 14261–14290.
- Noda, A., K. Yoshimatsu, S. Yukimoto, K. Yamaguchi, and S. Yamaki: 1999, Relationship between natural variability and CO₂-induced warming pattern: MRI AOGCM Experiment. *Proc. 10th Symposium on Global Change Studies, Dallas Texas*, American Meteorological Society, Boston, USA, volume 24, 359–362.
- Otto-Bliesner, B. and E. Brady, 2001: Tropical Pacific variability in the NCAR Climate System Model. *J. Climate*, **14**, 3587–3607.
- Pacanowski, R. C. and S. G. H. Philander, 1981: Parameterization of vertical mixing in numerical models of tropical oceans. *J. Phys. Oceanogr.*, **11**, 1443–1451.
- Parker, D. E., C. K. Folland, A. Bevan, M. N. Ward, M. Jackson, and K. Maskell: 1994, Marine surface data for analysis of climatic fluctuations of interannual to century timescales. *Natural Climate Variability on Decade-to-Century Time Scales*, D. G. Martinson, K. Bryan, M. Ghil, M. M. Hall, T. R. Karl, E. S. Sarachik, S. Soroostian, and L. F. Talley, eds., National Academy Press, 241–250, 222–228.
- Pearce, F., 1997: Sneaky El Niño outwits weather forecasters. *New Scientist*, **31 May**, 6.
- Philander, G. S. and A. Fedorov, 2003: Is El Niño sporadic or cyclic? *Annu. Rev. Earth Planet. Sci. Lett.*, **31**, 579–594.
- Philander, S. G., 1990: *El Niño, La Niña and the Southern Oscillation*. Academic Press, San Diego, 293 pp.
- Picaut, J., M. Ioulalen, C. Menkes, and T. Delcroix, 1996: Mechanism of the zonal displacement of the Pacific warm pool: implications for ENSO. *Science*, **274**, 1486–1489.
- Picaut, J., F. Masia, and Y. du Penhoat, 1997: An advective-reflective conceptual model for the oscillatory nature of the ENSO. *Science*, **277**, 663–666.
- Reynolds, R. W., N. A. Rayner, T. M. Smith, D. C. Stokes, and W. Wang, 2002: An improved in situ and satellite SST analysis for climate. *J. Climate*, **15**, 1609–1625.

Bibliography

- Reynolds, R. W. and T. M. Smith, 1994: Improved global sea surface analyses using optimum interpolation. *J. Climate*, **7**, 929–948, Niño indices are available from the Climate Prediction Center at <http://www.cpc.noaa.gov/data/indices/>.
- Rodbell, D., G. Seltzer, D. M. Anderson, M. B. Abbott, D. B. Enfield, and J. H. Newman, 1999: A 15,000 year record of ENSO-driven alluviation in southwestern Ecuador. *Science*, **283**, 516–520.
- Ropelewski, C. F. and M. S. Halpert, 1987: Global and regional scale precipitation patterns associated with the El Niño/Southern Oscillation. *Mon. Wea. Rev.*, **115**, 1606–1626.
- Schrama, E., R. Scharroo, and M. Naeije, 2000: Radar Altimeter Database System (RADS): Towards a generic multi-satellite altimeter database system. BCRS/USP-2 report 00-11, Netherlands Remote Sensing Board (BCRS), Delft, the Netherlands, ISBN 905 411 319 7.
- Stockdale, T. N., D. L. T. Anderson, J. O. S. Alves, and M. A. Balmaseda, 1998: Global seasonal rainfall forecasts using a coupled ocean–atmosphere model. *Nature*, **392**, 370–373.
- Stricherz, J., D. Legler, and J. O'Brien, 1997: *TOGA Pseudo-stress Atlas 1985–1994, Vol. II: Pacific Ocean*. Florida State University, Tallahassee, FL, USA, 158pp. pp.
- Suarez, M. J. and P. S. Schopf, 1988: A delayed action oscillator for ENSO. *J. Atmos. Sci.*, **45**, 3283–3287.
- Thomson, W., 1879: On gravitational oscillations of rotating water. *Proc. Roy. Soc. Edinburgh*, **10**, 92–100.
- Timmermann, A., J. Oberhuber, A. Bacher, M. Esch, M. Latif, and E. Roeckner, 1999: Increased El Niño frequency in a climate model forced by future greenhouse warming. *Nature*, **398**, 694–697.
- Trenberth, K. E., , and T. J. Hoar, 1997: The 1990-1995 El Niño-Southern Oscillation event: Longest on record. *Geophys. Res. Lett.*, **23**, 57–60.
- Tudhope, A. W., C. P. Chilcott, M. T. McCulloch, E. R. Cook, J. Chappell, R. M. Ellam, D. W. Lea, J. M. Lough, and G. Shimmiel, 2001: Variability in ENSO through a glacial-interglacial cycle. *Science*, **291**, 1511–1517.
- Tziperman, E., M. A. Cane, and S. E. Zebiak, 1997: Mechanisms of seasonal ENSO interaction. *J. Atmos. Sci.*, **54**, 61–71.
- Tziperman, E., L. Stone, M. A. Cane, and H. Jarosh, 1994: El Niño chaos: overlapping of resonances between the seasonal cycle and the Pacific ocean-atmosphere oscillator. *Science*, **264**, 72–74.
- Uppala, S. M. and coauthors, 2005: The ERA-40 re-analysis. *Quart. J. Roy. Meteor. Soc.*, submitted.

Bibliography

- van den Dool, H. M., 1994: Searching for analogues, how long must one wait? *Tellus*, **46A**, 314–324.
- van den Dool, H. M. and A. G. Barnston: 1994, Forecasts of global sea surface temperature out to a year using the Constructed Analogue method. *Proceedings of the Climate Diagnostics Workshop*, College Park, MD, 416–419.
- van der Vaart, P. C. F., H. A. Dijkstra, and F-F Jin, 2000: The Pacific cold tongue and the ENSO mode: Unified theory within the Zebiak-Cane model. *J. Atmos. Sci.*, **57**, 967–988.
- van Oldenborgh, G. J., M. A. Balmaseda, L. Ferranti, T. N. Stockdale, and D. L. T. Anderson, 2005: Did the ECMWF seasonal forecast model outperform a statistical model over the last 15 years? *J. Climate*, accepted.
- van Oldenborgh, G. J., G. Burgers, and A. Klein Tank, 2000: On the El Niño teleconnection to spring precipitation in Europe. *Int. J. Climatol.*, **20**, 565–574.
- van Oldenborgh, G. J., G. Burgers, S. Venzke, C. Eckert, and R. Giering, 1999: Tracking down the ENSO delayed oscillator with an adjoint OGCM. *Mon. Wea. Rev.*, **127**, 1477–1496.
- Vialard, J., C. Menkes, J.-P. Boulanger, P. Delecluse, and E. Guilyardi, 2001: A model study of oceanic mechanisms affecting equatorial Pacific sea surface temperature during the 1997-98 El Niño. *J. Phys. Oceanogr.*, **31**, 1649–1675.
- Von Storch, H. and F. W. Zwiers, 1999,2001: *Statistical Analysis in Climate Research*. Cambridge University Press, The Edinburgh Building, Cambridge CB2 2RU, UK, 484 pp., ISBN 0 521 45071 3 / 0 521 01230 9.
- Vose, R. S., R. L. Schmoyer, P. M. Steurer, T. C. Peterson, R. Heim, T. R. Karl, and J. K. Eischeid, 1992: The global historical climatology network: Long-term monthly temperature, precipitation, sea level pressure, and station pressure data. Technical Report NDP-041, Carbon Dioxide Information Analysis Center, Oak Ridge National Laboratory, Oak Ridge, Tennessee, U.S.A.
- Vossepoel, F. C., 1999: *Sea-Level Data Assimilation for Estimating Salinity Variability in the Tropical Pacific*. Ph.D. thesis, Utrecht University, the Netherlands.
- Wang, C., R. H. Weisberg, and H. Yang, 1999: Effects of the wind speed–evaporation–SST feedback on the El Niño–Southern Oscillation. *J. Atmos. Sci.*, **56**, 1391–1403.
- Wang, W. and M. J. McPhaden, 2000: The surface-layer heat balance in the equatorial Pacific ocean. Part II: Interannual variability. *J. Phys. Oceanogr.*, **30**, 2989–3008.
- 2001: Surface layer temperature balance in the equatorial Pacific during the 1997–98 El Niño and 1998–99 La Niña. *J. Climate*, **14**, 3393–3407.

Bibliography

- Wolff, J.-O., E. Maier-Reimer, and S. Legutke, 1997: The Hamburg Ocean Primitive Equation model HOPE. Technical Report No. 13, Deutsches Klimarechenzentrum, Bundesstr. 55, D-20146 Hamburg, Germany, Hamburg.
- Woodroffe, C. D., M. Beech, and M. K. Gagan, 2003: Mid-late holocene El Niño variability in the equatorial Pacific from coral microatolls. *Geophys. Res. Lett.*, **30**, doi:10.1029/2002GL015868.
- Xue, Y., A. Leetmaa, and M. Ji, 2000: ENSO prediction with Markov models: The impact of sea level. *J. Climate*, **13**, 849–871.
- Zebiak, S. E. and M. A. Cane, 1987: A model of El Niño–Southern Oscillation. *Mon. Wea. Rev.*, **115**, 2262–2278.
- Zelle, H., G. Appeldoorn, G. Burgers, and G. J. Van Oldenborgh, 2004: The relationship between sea surface temperature and thermocline depth in the eastern equatorial Pacific. *J. Phys. Oceanogr.*, **34**, 643–655, doi:10.1175/2523.1.
- Zelle, H., G. J. Oldenborgh, G. Burgers, and H. Dijkstra, 2005: El niño and greenhouse warming: Results from ensemble simulations with the NCAR CCSM. *J. Climate*, revised February 2005.
- Zelle, H. a., 2005: The evolution of SST anomalies in the warm pool during El Niño. *J. Phys. Oceanogr.*, submitted December 2004.

Samenvatting

El Niño – Southern Oscillation (ENSO) is een verschijnsel uit de Stille Oceaan rond de evenaar. Eens in de 3 tot 7 jaar wordt het oppervlaktewater in de buurt van zuid Amerika warmer dan normaal, soms wel meer dan 4 graden boven het gemiddelde. Deze opwarming strekt zich uit over de evenaar naar het westen over een afstand van duizenden kilometers, tot ver in de Stille Oceaan bij de datumgrens. Met de opwarming van dit enorme stuk oceaan gaan veranderingen in de atmosferische circulatie gepaard. Normaal waaien er sterke oostelijke passaatwinden over de evenaar, tijdens El Niño worden deze sterk verzwakt en in de westelijke Stille Oceaan draaien ze zelfs om van richting. De regenzone boven Indonesië schuift naar het oosten tot boven de oceaan, deze verschuiving zorgt voor droogte in Indonesië en omliggende landen. Bij sterke El Niño's bereikt de regen soms zelfs de westkust van zuid Amerika en kan daar overstromingen veroorzaken. De effecten van El Niño op het weer zijn duidelijk merkbaar tot in Afrika en Amerika, en zijn soms zelfs meetbaar in Europa.

De naam El Niño – Southern Oscillation (zuidelijke oscillatie) suggereert een schommeling: de El Niño fase wordt afgewisseld door La Niña, de omgekeerde fase. De oppervlaktetemperatuur van de Stille Oceaan rond de evenaar is dan kouder dan normaal, en de passaatwinden zijn sterker dan normaal. De gemiddelde tijd tussen twee El Niño's is ongeveer 4 jaar, maar de oscillatie is grillig: soms is er twee jaar achtereen een El Niño, soms gebeurt er jaren achtereen relatief weinig. Dit grillige gedrag maakt het moeilijk om goede voorspellingen te maken van El Niño, belangrijk voor landen zoals Indonesië die zwaar getroffen kunnen worden door de effecten van El Niño op het lokale klimaat.

Voorspellingen van El Niño worden gemaakt met numerieke modellen die ruwweg in twee categorieën zijn in te delen: algemene circulatie modellen (GCM) en eenvoudiger modellen. Een GCM deelt de oceaan en atmosfeer op in meerdere lagen en een rooster met cellen van circa 100 km grootte. Voor deze cellen worden de natuurkundige bewegingsvergelijkingen opgelost om het stromingspatroon te berekenen. Fysische processen op schalen kleiner dan één rooster cel kunnen niet door het model worden berekend en worden geparаметeriseerd. De categorie versimpelde modellen omvat zowel modellen die de oceaan en atmosfeer benaderen als een systeem met slechts één of twee lagen, alsmede statistische modellen die de hele oceaan of atmosfeer proberen te beschrijven met statistische verbanden. Een voorspelling wordt gemaakt door een zo goed mogelijke schatting van de begintoestand van oceaan en atmosfeer te maken en het model met deze begintoestand te starten.

Samenvatting

Het doel van dit proefschrift is om onze kennis van El Niño te vergroten. Recente observaties van de Stille Oceaan zijn geanalyseerd om hiermee belangrijke fysische mechanismen voor El Niño te verifiëren. Een tweede doel is om modelsimulaties van El Niño te verbeteren, wat kan leiden tot verbeterde voorspellingen. Dit is een traag proces; net zoals bij numerieke weersvoorspellingen ontwikkelen de modellen voor ENSO voorspellingen zich langzaam maar gestaag.

In hoofdstuk 2 wordt een analyse gemaakt van veranderingen in de diepte van de thermoklien, een scherpe scheiding tussen warm oppervlaktewater en koud, dieper water. Golven in de thermoklien staan centraal in de theoretische beschrijving van El Niño. Op de evenaar in de Stille Oceaan ligt de thermoklien op circa 50–150 meter diepte. De diepte van de thermoklien is gekoppeld aan de oppervlaktetemperatuur, met name in het oosten van de Stille Oceaan waar de thermoklien dicht bij het oppervlak ligt. Een verstoring (verdieping) van de thermokliendiepte geeft een vertraagde verstoring (verhoging) van de oppervlaktetemperatuur. Deze vertraging is belangrijk omdat hij mede verantwoordelijk is voor de periode van ENSO. In de oostelijke Stille Oceaan is de vertraging slechts twee weken, hier wordt een signaal in de thermokliendiepte door opwelling en menging van water vrijwel direct doorgegeven aan het oppervlak. In het westen rond de datumgrens is de vertraging veel groter: hier kan het tot 12 maanden duren voordat de oppervlaktetemperatuur reageert op een verstoring van de thermoklien. Het signaal reist hier met een omweg: een golf in de thermoklien (verdieping) beweegt in 2-6 maanden naar het oosten over de evenaar. Daar wordt de lokale oppervlaktetemperatuur verhoogd, hetgeen westenwind veroorzaakt over de westelijke en centrale Stille Oceaan. De westenwind warmt lokaal het oppervlaktewater op, door een combinatie van minder verdamping, minder menging en minder opwelling van dieper, kouder water. Tevens ontstaat een oostwaartse stroming die warmer water uit de westelijke Stille Oceaan naar het oosten transporteert.

In hoofdstuk 3 ligt de nadruk op het analyseren van fysische mechanismen die invloed hebben op de zeeoppervlaktetemperatuur in de westelijke en centrale Stille Oceaan. Deze regio wordt ook wel de “warm pool” genoemd, vanwege de hoge oppervlaktetemperatuur van rond de 29°C. Binnen het onderzoek naar El Niño is nog geen consensus bereikt over welke mechanismen in dit gebied het meest belangrijk zijn voor variaties van de oppervlaktetemperatuur, hoewel duidelijk is dat warmtetransport op de grens van oceaan en atmosfeer een belangrijke rol speelt. Met behulp van een warmtebudget, berekend uit een gekoppelde oceaan-atmosfeer modelsimulatie, wordt aangetoond dat een lokale verhoging (anomalie) van de oppervlaktetemperatuur zich zonaal verplaatst. Tijdens de ontwikkeling van El Niño verplaatst de temperatuur anomalie zich van de westelijke Stille Oceaan naar het oosten tot voorbij de datumgrens, en weer terug naar het westen tijdens het verval van El Niño. In bestaande literatuur wordt als oorzaak voor deze zonale beweging vooral zonale stroming genoemd, die op zijn beurt weer veroorzaakt wordt door anomale zonale wind aan het oppervlak. Uit het warmtebudget blijkt dat ook veranderingen in windsnelheid belangrijk zijn: deze veroorzaken veranderingen in verdamping aan het oppervlak en beïnvloeden de dikte van de menglaag. De menglaag is een goed doorgemengde laag aan het zeeoppervlak, circa 20 meter dik, waarin de temperatuur

Samenvatting

ongeveer constant is. Een verandering in de dikte van deze laag verandert ook de warmtecapaciteit, hetgeen invloed heeft op de warmtebalans aan het oppervlak en uiteindelijk leidt tot een verandering van de oppervlaktetemperatuur. Oostwaartse beweging van temperatuur anomalieën tijdens de groei van El Niño wordt voornamelijk veroorzaakt door een lokale verdunning van de menglaag door een afname van de passaatwinden. De westwaartse beweging tijdens het verval van El Niño wordt in gang gezet als deze winden weer in sterkte toenemen en een westwaartse stroming aan het oppervlak veroorzaken, en tevens door toegenomen uitgaande warmtestraling waardoor het oceanoppervlak in de oostelijke Stille Oceaan afkoelt.

Een vraag die recent veel aandacht heeft gekregen is “Hoe zal El Niño veranderen onder invloed van het broeikaseffect?”. Deze vraag is het onderwerp van hoofdstuk 4. Een verzameling van 62 simulaties met hetzelfde gekoppelde ocean-atmosfeermodel wordt hier geanalyseerd. Alle simulaties zijn van de periode 1940–2080, waarbij steeds een iets andere begintoestand gebruikt wordt. Na een paar weken zijn de simulaties in de atmosfeer al volledig verschillend, voor de ocean duurt dit wat langer. Iedere simulatie representeert een mogelijke ontwikkeling van het klimaat van de aarde. Ondanks een gesimuleerde wereldgemiddelde opwarming van $\sim 1.2^\circ\text{C}$ treden er binnen de simulaties geen noemenswaardige veranderingen op in het gedrag van El Niño. Omdat van te voren zeker niet uit te sluiten viel dat er een verandering zou kunnen optreden, wordt een nadere analyse uitgevoerd om uit te vinden waarom El Niño niet verandert, en of dit eventueel te wijten is aan fouten in het gebruikte model. Het blijkt dat ENSO in dit model zich gedraagt als een stabiel systeem aangedreven door ruis. De reactie van de oppervlaktewinden op veranderingen in de oppervlaktetemperatuur is zwak, ongevoelig voor veranderingen in de achtergrondtemperatuur en meer geconcentreerd rond de evenaar dan in waarnemingen. De analyse toont aan dat dit smalle wind patroon rond de evenaar inderdaad leidt tot een te stabiel systeem, met een relatief korte ENSO periode zoals ook in het gebruikte model gevonden wordt. Uit deze analyse kan geconcludeerd worden dat het nodig is om eerst de gevonden gebreken in het model (die ook voorkomen in andere veelgebruikte modellen) te verbeteren, alvorens een conclusie getrokken kan worden over het te verwachten gedrag van El Niño als de aarde verder opwarmt door menselijke invloeden.

In dit proefschrift worden een aantal toetsen en aanbevelingen geformuleerd voor modelsimulaties van El Niño – Southern Oscillation. Deze aanbevelingen kunnen bijdragen aan de ontwikkeling van betere modellen, en uiteindelijk aan betere ENSO voorspellingen. Algemene circulatie modellen zijn al drastisch verbeterd en presteren beter dan eenvoudige modellen, die niet alle belangrijke eigenschappen van de tropische Stille Oceaan kunnen bevatten. De toekomst van ENSO voorspellingen ligt in de verdere ontwikkeling van deze complexe modellen.

Samenvatting

Dankwoord

Het voltooien van dit proefschrift heeft niet alleen een sterk gevoel van opluchting te weeg gebracht, maar vooral ook dankbaarheid richting al mijn collega's en vrienden.

Gerrit en Geert Jan, jullie hebben een veelvoud van rollen aangenomen tijdens mijn promotie. Van dagelijkse begeleider tot coauteur, van spellingchecker tot hoofd van de afdeling oceanografie, van docent tot collega om mee te gaan lunchen in het park. Gerrit, ik heb veel van je geleerd over het doen van onderzoek en over het opschrijven ervan. Jouw bijdragen aan de artikelen in dit proefschrift werden soms op het moment zelf niet direct gewaardeerd (omdat ze vaak extra werk of correcties betekenden) maar waren bijna zonder uitzondering nuttig, eerlijk en een verbetering van het stuk. Ik ben blij dat het zelfstandig onderzoek doen waar je vanaf het begin naar op zoek was aan het eind nog tevoorschijn is gekomen. Geert Jan, jouw aanstekelijke enthousiasme voor je werk is niet te negeren. Ook van jou heb ik veel geleerd, vooral over statistiek, het visualiseren van data en het daarmee oplossen van problemen. Je geduld bij het corrigeren van onze artikelen en dit proefschrift heeft veel bijgedragen, dat waardeer ik zeer. Onze discussies over computers, muziek en andere niet aan werk gerelateerde zaken waren altijd een welkome afleiding, ik ben blij dat we vier jaar samen hebben kunnen werken.

Zonder promotor(en) geen promotie — ik ben blij dat ik het hebben van twee promotoren als een luxe heb ervaren en niet als last. Gerbrand, je bent als promotor op het KNMI altijd in de buurt geweest. Ik ben dankbaar voor jouw bijdrage in het zicht houden op de grote lijn, het relativeren als het moeilijk ging, het benadrukken van voortgang als het goed ging en vooral je constructieve commentaar op dit proefschrift. Boudewijn, hoewel er van de samenwerking tussen het KNMI en DEOS minder op papier gekomen is dan oorspronkelijk de bedoeling was, ben ik blij dat je mijn promotor bent. Door de band met DEOS is mijn blikveld verruimd met satelliet observaties, en heb ik hier veel over geleerd. Ook jouw rol in het overzicht houden op de voortgang van de promotie is erg nuttig geweest, en ik ben altijd met plezier naar Delft gegaan voor onze besprekingen.

Alle directe en minder directe collega's op het KNMI, bedankt! John en Gerrian, zonder jullie gezelschap waren deze vier jaar veel minder leuk geweest, en ik heb veel steun aan jullie gehad. Wilco, bedankt voor het kritisch aanhoren en corrigeren van mijn zoveelste dwaling in de wereld van de budgetstudies. Andreas, bedankt voor je hulp bij het verkrijgen en analyseren van data. Camiel, bedankt voor het oplossen van talloze computerproblemen en je assistentie bij het draaien van modellen. Brigitta en

Dankwoord

Greet, bedankt voor jullie geduld, goede humeur en hulp bij alle administratie.

Fei-Fei, Soon-Il, Brandon, Qinghua, Yongxin and all others at the meteorological department of the University of Hawaii at Manoa, thank you for being my supervisor, colleagues and friends during my stay in Hawaii.

Tot slot gaat mijn dank uit naar mijn ouders, familie en vrienden die me gesteund hebben tijdens mijn promotie, en ervoor gezorgd hebben dat dit boekje nu daadwerkelijk gedrukt wordt. Evelyn, jou wil ik in het bijzonder bedanken voor je steun en aanmoediging tijdens het maken van dit proefschrift. Dankzij jou kijk ik er met plezier op terug!

Curriculum vitae

Hein Daniël Zelle werd geboren op 14 mei 1975 te Geldrop. Na de lagere school heeft hij van 1987 tot 1993 een VWO opleiding gevolgd aan het Sint-Joris college te Eindhoven. In 1993 is hij begonnen aan de opleiding technische natuurkunde van de Rijks Universiteit Groningen. Na een onderzoek bij het Kernfysisch Versneller Instituut aldaar is hij in mei 2000 afgestudeerd in de richting fysische informatica.

Zijn interesse voor het weer vanuit zijn hobby zweefvliegen heeft ertoe geleid om te solliciteren bij het Koninklijk Nederlands Meteorologisch Instituut. Dit leidde tot een aanstelling als onderzoeker in opleiding bij de afdeling Oceanografisch Onderzoek in November 2000. Van oktober 2002 tot maart 2003 heeft hij aan zijn onderzoek gewerkt bij de faculteit meteorologie van de University of Hawaii at Manoa, te Honolulu. Dit proefschrift bevat de drie wetenschappelijke artikelen die uit het onderzoek zijn voortgekomen.

Sinds 14 februari 2005 heeft hij een aanstelling als project manager bij ARGOSS in Vollenhove, waar hij werkt aan golven en wind in kustwateren.

